Evaluating Aminotransferase Targets and Enhanced Imaging Modalities in Pancreatic Ductal Adenocarcinoma

by

Noah S. Nelson

A dissertation submitted in partial fulfillment
of the requirement for the degree of
Doctor of Philosophy
(Molecular and Integrative Physiology)
in the University of Michigan
2026

Doctoral Committee:

Professor Costas A. Lyssiotis, Chair
Professor Timothy L. Frankel
Professor Marina Pasca di Magliano
Professor Yatrik M. Shah

Noah S. Nelson

noahnels@umich.edu

ORCID iD: 0000-0002-2972-442X

© Noah S. Nelson 2026

Table of Contents

List of Figures ...……...iii

List of Tables……..v

Abstract …….vi

Chapter 1 — Introduction to Pancreatic Ductal Adenocarcinoma……1

Chapter 2 — Aspartate Transaminases Are Dispensable for Pancreatic Development and Pancreatic Cancer Progression……63

Chapter 3 — Selective and Targeted Molecular MRI of Pancreatic Cancer Using a Polyethylene Glycol Nanopolymer……....119

Chapter 4 — Future Directions and Conclusions……140

List of Figures

Figure 1-1 Diagram of basic pancreas anatomy and surrounding structures. ……..…59

Figure 1-2 Malate-Aspartate Shuttle. ……...……61

Figure 1-3 Arginine-Glycine-Aspartate (RGD) Structures. ……62

Figure 2-1 Mouse pancreatic functions are maintained without Got1 or Got2. ……..99

Figure 2-2 Knockout of pancreatic Got1 or Got2 does not impact precancerous lesion formation. ……..101

Figure 2-3 Loss of Got1 or Got2 does not improve survival in genetically engineered models of pancreatic cancer. ……...103

Figure 2-4 Got1 or Got2 loss does not alter the composition of immune and epithelial compartments in the tumor microenvironment. ……104

Figure 2-5 PDAC cells adapt their metabolism to counter GOT loss. ……105

Supplementary Figure 2-1……109

Supplementary Figure 2-2……111

Supplementary Figure 2-3……112

Supplementary Figure 2-4……113

Supplementary Figure 2-5……115

Supplementary Figure 2-6……117

Figure 3-1 Nuclear magnetic resonance (NMR) spectrum depicting separation between water and polyethylene glycol (PEG) signatures. ……..134

Figure 3-2 Schematic of the iRGD-PEG imaging strategy. ……135

Figure 3-3 Sensitivity of magnetic resonance imaging (MRI) to diffusion-weighted (DW), T2-weighted (T2W) selective polyethylene glycol (PEG) imaging. ……..136

Figure 3-4 *In vivo* imaging of PEG in mouse with PEG-Matrigel flank injection. …….137

Figure 3-5 Selective imaging of PEG in murine PDAC tumors. ……..138

Figure 3-6 *In vivo* imaging of singular PEG, singular iRGD, and joint PEG-iRGD administration. ……139

List of Tables

Table 1-1 Hereditary pancreatic cancer syndrome. ……60

Table 2-1 sgRNA sequences. ……107

Table 2-2 PCR primers for genotyping. ……...108

Abstract

Pancreatic ductal adenocarcinoma (PDAC) is a particularly devastating disease with poor prognosis and inadequate treatment strategies. For the vast majority of patients, a PDAC diagnosis is essentially a near-term death sentence, with only around 10% of all patients surviving 5 years beyond their initial diagnosis. The primary issue leading to these pernicious outcomes is that most individuals do not even realize they have PDAC until the cancer has metastasized and surgical intervention is no longer a viable option and current therapies are not efficacious in metastatic disease. There is currently no standard population-wide screening method, and efforts focus on high-risk groups such as those with a strong family history, genetic predispositions, or specific clinical risk factors. Even among the most high-risk individuals, the surveillance system is underwhelming and offers much room for improvement. As such, a strategy designed to enhance screening options for individuals of all risk categories that provides precise and accurate diagnostic measurements would provide a substantial benefit to providers, patients, and family members alike.

In the first chapter of this thesis, I will provide an overview of the current state of PDAC, including its most common risk factors, the current screening standards, and how imaging is presently being performed. I also discuss PDAC metabolism and specific pathways that may offer opportunities for strategic therapeutic targets. Furthermore, I will describe some potential areas for improvement in these issues and

how a broader surveillance system could increase early diagnosis of PDAC and thereby impact PDAC survival statistics. In Chapter Two, I will describe our investigation into two specific enzymatic targets in the PDAC metabolic pathway, namely glutamate oxaloacetate transaminase 1 and 2 (GOT1 and GOT2), detailing how these transaminases are not essential to PDAC progression or to functional pancreatic development. Chapter Three highlights the initial work we have undertaken in developing a magnetic resonance imaging (MRI)-based protocol to address some of the gaps in PDAC surveillance. While undoubtedly early in the process, this work shows some promising results utilizing a combination of polyethylene glycol (PEG) and an internalizing arginine-glycine-aspartic acid (iRGD) molecule to enhance the fidelity of pancreatic tumor MRI in the absence of potentially harmful contrast agents and ionizing radiation. In Chapter Four, I will put our new work into the context of the existing body of PDAC treatment and imaging literature, describing how it may advance the field further. Here I also explain the limitations of our study as well as the future directions that we hope to explore.

Chapter 1: Introduction to Pancreatic Ductal Adenocarcinoma

1.1 Background

In this chapter, I will describe the foundational aspects of pancreatic cancer, including the relevant anatomical and physiological structures, the various disease types, and epidemiological characteristics unique to this pathology. I will then focus my attention on pancreatic ductal adenocarcinoma (PDAC), as that is the specific subtype of interest in our laboratory. After covering the molecular factors unique to PDAC, I will describe the risk factors and common complications that patients are likely to experience. This will lead to a discussion of the relevant metabolic pathways in PDAC progression and how various components of these pathways have been targeted therapeutically. Our two primary enzymes of interest, glutamate oxaloacetate transaminase 1 and 2 (GOT1 and GOT2), will be highlighted and reviewed prior to their further experimental description in Chapter 2.

In shifting to the PDAC imaging literature, I will provide an overview of the currently published screening criteria used by clinicians to diagnose PDAC. While there is some overlap within these recommendations among the various PDAC committees, there is no agreed upon standard as to which prospective patients require preemptive assessment. Furthermore, the diagnostic techniques are case-dependent, as I will describe in the section highlighting the various imaging modalities used. Of these, we chose to utilize magnetic resonance imaging (MRI) within our experimental protocol,

and therefore I provide a more extensive description of the latest techniques and cutting-edge approaches that have been developed recently for this technology. Finally, I will provide an overview of both polyethylene glycol (PEG) and arginine-glycine-aspartate (RGD) peptides in biomedicine, as these compounds will be described further in our experiments highlighted in Chapter 3.

1.2 Anatomy and physiology of the pancreas

The pancreas is a retroperitoneal organ of the upper abdomen, located behind the stomach and in front of the spine. It is divided into three main parts: the head, the body, and the tail. The head of the pancreas is nestled within the first loop of the duodenum, while the tail extends to the spleen (**Figure 1-1**). The vast majority of the pancreas is composed of exocrine tissue, which is responsible for synthesizing and secreting digestive enzymes such as amylase, lipase, trypsin, and chymotrypsin. The enzymes are produced in the acinar cells and then are secreted into the duodenum of the small intestine in order to break down dietary carbohydrates, fats, and protein for subsequent absorption (1,2).

In addition to its important exocrine functions, the pancreas also plays a significant endocrine role as well. The islets of Langerhans, which only comprise about 1% of pancreatic tissue, contain five main cell types: alpha cells, beta cells, delta cells, F-cells, and epsilon cells. The alpha cells produce glucagon, a hormone that increases blood sugar levels by signaling the liver to convert stored glycogen into glucose. The beta cells produce insulin, which performs the opposite function of glucagon, lowering blood sugar levels by enabling cellular uptake of glucose. Delta cells represent a smaller proportion of the islet cells and produce somatostatin, an inhibitory hormone

responsible for regulating both glucagon and insulin release from their respective cell types. F-cells produce pancreatic polypeptide, which regulates digestion by inhibiting gastric emptying and biliary secretion, thereby allowing additional time for nutrient absorption. Lastly, the epsilon cells produce ghrelin, which induces hunger signals. All five of these endocrine cell types produced in the pancreas play a critical role in energy homeostasis and blood glucose regulation (1,2).

1.3 Defining pancreatic cancer

Pancreatic cancer can be broken down into two major classifications, neuroendocrine or exocrine, based on the cell type in which it originates. The differences between these two cancer types will be outlined below.

1.3.1 Neuroendocrine pancreatic tumors

As their name suggests, neuroendocrine pancreatic tumors (pNETs) are a type of pancreatic cancer that arises from the endocrine islet cells. They represent a small fraction (only 1-2%) of all pancreatic cancers and can be further classified as either functional or non-functional tumors. (3)

Functional pNETs are those that secrete excess hormones, thereby causing secondary effects related to their specific cell type of origin. Insulinomas are the most common type of functional pNET, accounting for around 70% of the category. (4) These tumors are characterized by excessive insulin secretion, which results in recurrent hypoglycemia. Gastrinomas cause excess gastrin release, leading to peptic ulcer formation. Glucagonomas can cause diabetes and weight loss from high blood glucose levels following excess glucagon secretion. VIPomas are tumors that secrete vasoactive intestinal peptide and have symptoms such as severe diarrhea, low potassium levels,

and dehydration. Somatostatinomas can also cause diabetes, as well as gallstones and steatorrhea. (3) Fortunately, given their noticeable clinical symptoms, functional pNETs are often diagnosed when the tumors are still small, and therefore patients have a fairly good prognosis, with a 5-year survival rate of around 90% when caught early. (4)

Non-functional pNETs are much more common than their counterparts, constituting 60-90% of cases. These tumors often grow asymptomically until they are large enough to cause an obstruction or metastasize. As such, the 5-year survival can be as low as 19%, considerably below the rate seen in functional pNETs. (4)

1.3.2 Exocrine pancreatic cancer

Exocrine pancreatic cancer is by far the most common type of pancreatic cancer, accounting for approximately 95% of all cases. (5) The vast majority of these cases are PDAC, which comprises 85% of exocrine pancreatic cancer cases and is the focal point of this thesis. The remaining 10-15% of exocrine-originating diagnoses are rare cancers that distinguish themselves from pancreatic ductal adenocarcinoma (PDAC) by various unique anatomopathological features. These histotypes include acinar cell carcinoma, pancreatoblastoma, and solid pseudopapillary neoplasms. Due to the rarity of these cancers, most of their characterization comes from single-center case reports and smaller retrospective analyses.

1.3.3 Symptoms of PDAC

PDAC typically causes symptoms because the tumor obstructs ducts, invades nerves, and disrupts both exocrine and endocrine pancreatic function. Common effects include abdominal or back pain from local invasion and nerve involvement, jaundice from biliary obstruction (often with dark urine, pale or greasy stools, and pruritus), and

progressive weight loss with loss of appetite due to cancer-associated cachexia and malabsorption from exocrine insufficiency. Many patients also experience nonspecific gastrointestinal symptoms such as nausea, early satiety, bloating, and steatorrhea as tumor burden increases and gastric emptying or bile flow becomes impaired. (6-7)

Systemic and metabolic consequences are also frequent. New-onset or worsening diabetes can occur as PDAC damages islet cells and alters insulin secretion, while tumor-related hypercoagulability predisposes to venous thrombosis and embolic events. As disease advances or metastasizes (commonly to liver and peritoneum), patients may develop worsening fatigue, ascites, right upper quadrant discomfort, and further nutritional decline. In many individuals, these secondary effects of the tumor—pain, jaundice, weight loss, and metabolic derangements—are the first clinically apparent manifestations, which is one reason PDAC is often diagnosed at an advanced, symptomatic stage. (6-7)

1.3.4 Molecular features of PDAC

In addition to the broader clinical symptoms with which patients present, PDAC is also characterized by a set of well-defined molecular features, involving recurrent genetic mutations and alterations in critical oncogenes and tumor suppressor genes.

PDAC is driven by a characteristic set of genomic alterations superimposed on a complex stromal and immune microenvironment. At the core of its molecular pathogenesis are near-ubiquitous activating mutations in the Kirsten rat sarcoma viral oncogene homolog gene (KRAS, most often at codon 12), which occur in more than 85% of tumors and are already detectable in early pancreatic intraepithelial neoplasia (PanIN) lesions, where they initiate aberrant mitogen-activated protein kinase (MAPK)

and phosphoinositide 3-kinase (PI3K) signaling, metabolic reprogramming, and resistance to apoptosis. Progressive accumulation of inactivating alterations in the canonical tumor suppressors CDKN2A/p16, TP53, and SMAD4/DPC4 then drives stepwise evolution from low-grade PanIN to invasive and metastatic carcinoma, with CDKN2A loss disrupting G1–S cell-cycle control, TP53 alteration impairing DNA damage responses and genomic stability, and SMAD4 loss abrogating TGF-β–mediated growth inhibition. Large sequencing series show that concurrent disruption of KRAS, CDKN2A, TP53, and SMAD4 is associated with higher metastatic burden and poorer survival, whereas a genomically stable minority lacking these canonical events follows distinct evolutionary routes. (8-11)

Beyond the core drivers, PDAC exhibits a broader genomic and epigenomic landscape involving chromatin regulators, DNA damage repair (DDR) genes, and lineage-specifying transcription factors. Whole-exome and panel sequencing studies have identified recurrent alterations in genes such as ARID1A and other SWI/SNF components, as well as MYC and GATA6 amplifications, which contribute to chromatin remodeling, transcriptional reprogramming, and maintenance of classical versus basal-like expression subtypes. Germline or somatic mutations in DDR genes, including BRCA1/2, PALB2, ATM, and related pathways, define a clinically relevant subset with genomic instability and potential sensitivity to platinum agents and PARP inhibition, while more recent exome data emphasizes the contribution of ATM, WRN, PALB2, and additional DDR defects to PDAC susceptibility and progression. At the tumor–host interface, PDAC is characterized by a dense desmoplastic stroma rich in cancer-associated fibroblasts and extracellular matrix, which shapes immune exclusion

and supports an immunosuppressive milieu dominated by heterogeneous T-cell populations and myeloid cells; spatial analyses of stromal maturity and tumor–stroma ratio show that these stromal features tightly correlate with patterns of macrophage and lymphocyte infiltration and are increasingly recognized as molecularly encoded determinants of prognosis and therapeutic response. Collectively, PDAC is defined by a constellation of key genetic drivers, significant genomic instability, specific molecular subtypes, and a uniquely fibrotic and immune-modulating microenvironment. (11-13)

1.3.5 PDAC statistics

PDAC is a highly lethal cancer with increasing global incidence and mortality rates. In recent years, the global incidence of PDAC has risen, with estimates showing that it ranks among the top ten cancers worldwide. The incidence rate of PDAC in the United States is approximately 13.8 cases per 100,000 men and women annually, translating to nearly 70,000 new cases each year. Although this only represents 3.3% of all new cancer diagnoses in the US, PDAC accounts for nearly 8% of all cancer deaths, demonstrating an outsized impact for this disease. The five-year survival rate for PDAC remains extremely low with the most recent national statistics citing only 8%. In 2025, it is projected that 52,000 individuals will die from pancreatic cancer in the U.S. alone. Globally, it is the third, and soon expected to be the second, leading cause of cancer death in developed regions. (14,15)

1.4 Risk factors for PDAC

Although PDAC has a relatively low lifetime risk in the United States (approximately 1.5% by age 75), there are several factors that can significantly increase the likelihood of disease development. (16) These range from genetic contributors, age,

specific disease comorbidities, as well as environmental and modifiable factors that can all impact pancreas health.

1.4.1 Family history and genetic disorders

Familial pancreatic cancer is defined as the presence of two or more immediate relatives with PDAC. Furthermore, if family members are younger than 50 when they are diagnosed, the risk ratio of developing PDAC is nearly 10-fold compared to the normal population. Other autosomal dominant or recessive gene mutations lead to diseases that have varying impact on a patient's relative risk (RR) to PDAC, some which were briefly discussed previously. (**Table 1-1**) Peutz-Jeghers syndrome (*STK11/LKB1*, RR: 132), hereditary pancreatitis (*PRSS1*, RR: 60-87), familial atypical multiple mole melanoma syndrome (*CDKN2A/p16*, RR: 13-22), hereditary nonpolyposis colorectal cancer (*hMSH2* and *hMLH1*, RR: 8.6), hereditary breast and ovarian cancer syndrome (*BRCA1/2* and *PALB2*, RR: 4.1-5.8), hereditary colorectal adenomatous polyposis (*APC*, RR: 4.4), Li-Fraumeni syndrome (*TP53*, RR: 7.3), and ataxia-telangiectasia mutation (*ATM*, RR: 3.9) represent some of the more common hereditary diseases that are closely associated with familial pancreatic cancer. Clearly, these genetic mutations play a serious, but variable role in the risk of developing PDAC, ranging from a 4-fold to a 132-fold increase in the likelihood of a positive lifetime diagnosis. (16,17) Despite these dramatic numbers, only 10% of patients with pancreatic cancer have an inherited risk identified.

1.4.2 Comorbidities and complications

In addition to familiar factors, other specific characteristics and comorbidities also dramatically increase PDAC risk in the general population. Age is the most significant

risk factor for PDAC, with incidence rising exponentially across the lifespan. The median age at diagnosis is approximately 71 years, and more than 80% of patients present with advanced disease after age 65. Aging fundamentally alters the stromal compartment, accelerating PDAC progression through age-related fibrosis and cancer-associated fibroblast (CAF) dysfunction. Studies comparing identical cancer cells implanted into young versus old mice demonstrate that tumors in older hosts grow faster and metastasize more extensively. This acceleration is driven by aged CAFs that secrete excess extracellular matrix proteins, creating a fibrotic, stiffened TME that promotes immune suppression and metastasis. (18) From a molecular standpoint, aging leads to increased DNA repair dysfunction, causing genome instability and accumulation of more mutations in PDAC driver genes. Age-related oxidative damage causes protein carbonylation, enzyme dysfunction, and hydrophobic aggregate formation that promotes carcinogenesis. Lastly, epigenetic changes like global methylation alterations with age may silence tumor suppressor genes, further facilitating tumor initiation. (19)

In patients with long-standing type 2 diabetes mellitus (T2DM), PDAC risk is 1.5-2 times as high as non-diabetic patients. The risk is even higher for those with a recent T2DM diagnosis, as those within one year of diagnosis are over five times as likely to have a PDAC diagnosis. Further complicating matters, PDAC onset can also cause diabetes mellitus, sometimes referred to as pancreatogenic diabetes, and therefore patients with a new-onset diagnosis, especially those over the age of 50, are encouraged to be screened for PDAC. (16, 20)

Overweight and obese patients are also in a higher risk category for PDAC. According to a meta-analysis involving 9504 cases, for every increase in body mass

index (BMI) of 5 kg/m^2, the risk of developing PDAC increased 1.1-fold. In addition, each increase in waist circumference of 10cm leads to a 1.11-fold higher risk. (21) Individuals with a BMI over 30 kg/m^2 who are under the age of 30 are at a 3.5-fold higher risk. (16)

Chronic pancreatitis is a well-established risk factor for PDAC, with numerous studies demonstrating that chronic inflammation, enhanced cell turnover, and fibrotic tissue remodeling in the pancreas lead to an environment conducive to PDAC development. Prolonged inflammation may lead to genetic changes in pancreatic tissue, such as activation of oncogenes like *Kras*. Collectively, chronic pancreatitis leads to a 5- to 15-fold increase in PDAC diagnosis. (22)

Intraductal papillary mucinous neoplasms (IPMNs) are defined as cystic tumors that arise from the epithelial cells lining the pancreatic ducts and produce thick mucinous fluid. These cysts often remain benign, but some can progress to PDAC in certain situations. If discovered, IPMNs are closely monitored, as malignant transformation occurs in 8% of patients within 10 years. (23)

1.4.3 Environmental and lifestyle exposures

It is well known that tobacco use has detrimental effects on overall health and risk of PDAC diagnosis is no different. Compared to non-smokers, those who use tobacco have a 1.68-fold increased risk of developing PDAC. (24) Similarly, heavy alcohol consumption is associated with a 1.22-fold increase in PDAC risk. Indirectly, alcohol consumption is also closely linked to chronic pancreatitis, which has an aforementioned 5- to 15-fold increase in PDAC risk. (25)

1.5 PDAC Metabolic Profile

In addition to the previously mentioned molecular and genetic factors associated with disease development, PDAC exhibits profound metabolic reprogramming driven by oncogenic KRAS mutations, tumor suppressor loss, and the hypovascular, nutrient-deprived tumor microenvironment. The metabolic landscape integrates interconnected core pathways such as glucose and glutamine metabolism, autophagy and macropinocytosis, and redox homeostasis. Collectively, these pathways sustain rapid proliferation, immune evasion, and therapeutic resistance and are tightly regulated by nutrient-sensing hubs and exhibit remarkable plasticity, enabling PDAC cells to adapt through compensatory metabolic routes when individual pathways are disrupted. Within this section, I will also provide a specific description of the changes that occur regarding the aspartate transaminases GOT1 and GOT2, as these enzymes will be the focus of Chapter 2 in the thesis.

1.5.1 Glucose metabolism

PDAC cells exhibit the Warburg effect—preferential aerobic glycolysis even under normoxia—driven by oncogenic KRAS and hypoxia-inducible factor-1α (HIF-1α). This metabolic rewiring supports rapid ATP generation, biosynthetic precursor production, and creation of an immunosuppressive acidic microenvironment. (26) KRAS increases cellular uptake and subsequent phosphorylation of glucose by upregulating glucose transporter type 1 (GLUT1) and hexokinase 2 (HK2), which effectively traps the glucose intracellularly. (27) To direct carbons toward glycolysis rather than oxidative phosphorylation, the rate-limiting enzymes phosphofructokinase-1 (PFK1) and enolase 1 (ENO1) are upregulated. (28) A high expression of lactate dehydrogenase A (LDHA) rapidly converts pyruvate to lactate, sustaining high-speed glycolysis via regeneration of

NAD+ and also resulting in massive lactate secretion, which acidifies the tumor microenvironment (TME). This acidification suppresses anti-tumor immunity and promotes the activation of pancreatic stellate cells, contributing to the dense fibrosis characteristic of PDAC. (29)

Glucose carbons are strategically diverted from glycolysis into collateral pathways to maintain the structural building blocks of the pancreatic tumor. Glucose-6-phosphate is shunted into the oxidative arm of the pentose phosphate pathway (PPP), generating ribose-5-phosphate for nucleotide synthesis and NADPH. These components are crucial for neutralizing the high levels of reactive oxygen species (ROS) that are produced as a by-product of rapid proliferation. (27) Within the hexosamine biosynthesis pathway (HBP), fructose-6-phosphate is diverted to produce UDP-GlcNAc. Used for *O*-GlcNAcylation, this substrate provides stabilization of oncogenic proteins like c-MYC and PFK1 and modifies extracellular matrix via hyaluronan production, further increasing the interstitial pressure and drug resistance of the TME. (27)

1.5.2 Glutamine metabolism

PDAC cells demonstrate unique glutamine addiction characterized by quantifiable metabolic distortion. Metabolomic analysis of human resected tumors reveals that glutamine is the single most depleted amino acid in PDAC tissue relative to adjacent benign pancreas, a finding consistently replicated across both human specimens and murine models. (30-32) This glutamine depletion stems directly from the TME's poorly vascularity and fibrosis, limiting circulating nutrient delivery. As with the glycolytic alterations, the genetic basis of the glutamine addiction is oncogenic KRAS,

which directly reprograms glutamine metabolism through transcriptional regulation of key metabolic enzymes.

PDAC cells have evolved a fundamentally different glutamine utilization strategy compared to canonical models observed in other cancers. While most cells employ glutamate dehydrogenase (GLUD1) to convert glutamine-derived glutamate into α-ketoglutarate for tricarboxylic acid (TCA) cycle anaplerosis, PDAC relies predominantly on a non-canonical transaminase-dependent pathway. (32) In this pathway, glutamine-derived glutamate undergoes transamination via mitochondrial aspartate aminotransferase (GOT2), generating aspartate that is transported to the cytoplasm. There, cytosolic aspartate aminotransferase (GOT1) catalyzes conversion to oxaloacetate, which is subsequently transformed into malate and then pyruvate via malate dehydrogenase 1 (MDH1) and malic enzyme 1 (ME1). Critically, this sequential enzyme cascade was initially hypothesized to support TCA cycle anaplerosis, but isotope-labeling experiments revealed an unexpected primary function: the generation of reducing power in the form of NADPH. (33) The biological significance of this redox axis is profound. Whereas glutamine deprivation modestly compromises TCA cycle function and ATP production, it catastrophically disrupts intracellular redox homeostasis in PDAC cells, causing rapid accumulation of ROS and depletion of reduced glutathione (GSH). This elevated demand for NADPH during proliferation far exceeds that needed for homeostasis and cannot be compensated by glucose-dependent sources. Empirically, the redox imbalance induced by glutamine withdrawal—but not by glucose withdrawal—halts PDAC proliferation, and this growth inhibition can be completely rescued by media supplementation with cell-permeable glutathione or the antioxidant N-

acetyl cysteine. This finding established that NADPH-dependent redox maintenance is the critical rate-limiting function of glutamine in PDAC. (33-34)

KRAS upregulates GOT1 expression while simultaneously suppressing GLUD1. This creates a ratio shift that funnels glutamine metabolism away from the canonical GLUD1 pathway and toward the transaminase-dependent redox pathway. Experimentally, suppression of any component enzyme in the GOT1-MDH1-ME1 axis produces pronounced suppression of PDAC growth both in vitro and in orthotopic xenografts, whereas GLUD1 suppression has no effect. Critically, this metabolic rewiring is dispensable in normal differentiated cells—GLUD1 suppression does not impair growth in a panel of normal cell lines—providing a potential therapeutic window. (31-33, 35)

1.5.3 Autophagy and macropinocytosis

The metabolic resistance of PDAC is fundamentally underpinned by two lysosomal scavenging pathways, autophagy and micropinocytosis. Both pathways feed into the lysosome to generate a pool of amino acids, lipids, and nucleotides, but they differ fundamentally in source and regulation. Autophagy is a catabolic process where double-membrane vesicles called autophagosomes sequester intracellular components, such as damaged organelles, and misfolded proteins, and fuse with lysosomes for degradation. (36) Unlike most tissues where autophagy is induced by starvation, PDAC exhibits constitutive autophagy even in nutrient-rich conditions. This is driven by the MiT/TFE transcription factor family, which uncouples autophagy from typical mTORC1 suppression. (37) Autophagy maintains the mitochondrial pool of functional iron and

intermediates for the TCA cycle. Crucially, it degrades MHC-I molecules via NBR1, preventing antigen presentation and promoting immune evasion. (38)

Macropinocytosis, on the other hand, is an actin-dependent, non-selective endocytic process where the cell membrane engulfs large volumes of extracellular fluid. It is the primary route for scavenging albumin, which is the most abundant protein in the TME. (39) This process is driven directly by KRAS and enhanced by PTEN loss via mTORC2. It allows PDAC cells to bypass the lack of free amino acids in the desmoplastic stroma by degrading albumin into glutamine and alanine. (39-40)

1.5.4 Redox homeostasis

Redox homeostasis in PDAC represents a survival mechanism that distinguishes tumor cells from their neighbors. Rather than simply reducing ROS, PDAC cells engage in precise orchestration of pro-oxidant production and antioxidant capacity, allowing them to maintain a metabolic identity optimized for rapid growth while resisting both endogenous and therapeutic oxidative stress. PDAC cells exist in a chronic state of elevated ROS compared to normal tissue, yet paradoxically upregulate antioxidant defenses simultaneously. (41) This apparent contradiction is resolved by understanding that KRAS directly drives both ROS generation and its detoxification. (42) Mitochondrial electron transport chain (ETC) dysfunction is the primary source of ROS production. As previously mentioned, PDAC cells exhibit the Warburg effect, generating high NADH flux that exceeds oxidative capacity and spills electrons onto oxygen, creating superoxide. (41) Additional sources include NOX activation (NADPH oxidase), which KRAS upregulates via p38 signaling, and COX-2 activity, which produces hydrogen peroxide as a byproduct. (43-44) This creates a constitutive ROS pressure that, left

unchecked, would trigger senescence or apoptosis. (42) KRAS also activates NRF2, the master transcription factor governing antioxidant responses, demonstrating the ability of KRAS to activate both the fuel for growth via glycolysis as well as the antioxidant shield necessary to tolerate it. (41-42) The elevated antioxidant capacity exhibited in PDAC requires massive NADPH flux, and therefore PDAC cells have co-opted three redundant NADPH-generating pathways, including the PPP, the malic enzyme pathway, and the isocitrate dehydrogenase 1 pathway. (45-47)

1.5.5 Aspartate transaminase function in PDAC

As previously mentioned, PDAC cells exhibit a unique metabolic adaptation driven by oncogenic KRAS mutations that fundamentally rewires glutamine utilization. Unlike most cancers that rely on GLUD1 for canonical glutamine metabolism, PDAC cells preferentially employ a non-canonical pathway orchestrated by GOT1 and GOT2. (32, 48-49) This pathway begins in the mitochondria where glutaminase (GLS1) converts glutamine to glutamate, which GOT2 then transaminates with oxaloacetate to produce aspartate and α-ketoglutarate/2-OG as a part of the malate aspartate shuttle (**Figure 1-2**). Aspartate is exported to the cytoplasm where GOT1 catalyzes its conversion back to oxaloacetate. Through subsequent reactions mediated by malate dehydrogenase (MDH1) and malic enzyme 1 (ME1), this generates pyruvate and—critically—NADPH, the primary reducing equivalent for maintaining redox balance. ME1 produces NADPH at levels comparable to the pentose phosphate pathway, underscoring its importance in cancer metabolism. (50-52) KRAS directly regulates this metabolic rewiring by transcriptionally upregulating GOT1 expression while suppressing GLUD1. The PI3K/mTORC2 pathway further amplifies GOT1 expression through HIF-

2α activation, particularly under hypoxic conditions that characterize the poorly vascularized PDAC tumor microenvironment. This coordinated reprogramming enables PDAC cells to efficiently manage oxidative stress while supporting rapid proliferation—a metabolic phenotype dispensable in non-transformed pancreatic cells. (32, 50, 53)

Beyond redox regulation, GOT-mediated aspartate biosynthesis serves an essential biosynthetic function. Aspartate represents a rate-limiting precursor for both purine and pyrimidine nucleotide synthesis, and its depletion causes S-phase arrest through activation of the ATR-mediated DNA damage response pathway. When glutamine is deprived or GOT function is impaired, insufficient deoxynucleotide pools generate stretches of single-stranded DNA during replication, triggering checkpoint activation and proliferative arrest. (54-55) This nucleotide limitation explains why GOT2 knockdown induces cellular senescence in PDAC cells—a phenotype mediated through ROS accumulation and p27 upregulation rather than classical p53 or p16 pathways. Importantly, this senescence response occurs specifically in PDAC cells bearing KRAS mutations and frequent p53/p16 alterations, while normal pancreatic ductal cells remain largely unaffected by GOT2 inhibition. (56)

Interestingly, there has been a stark discrepancy in the literature over whether GOT1 and GOT2 are required for PDAC development and progression. Several *in vitro* studies demonstrate profound proliferative defects following GOT inhibition. GOT1 knockdown causes cytostasis characterized by G1 arrest with minimal apoptosis, reversible upon restoration of GOT1 expression. (53, 57) GOT2 knockdown similarly impairs colony formation and proliferation across multiple PDAC cell lines while sparing non-transformed cells. (56, 58) Accumulation of NADH causes reductive stress that

inhibits GAPDH, creating a glycolytic bottleneck with elevated upstream metabolites and depleted downstream glycolytic intermediates. Simultaneously, mitochondrial metabolism suffers from decreased aspartate and α-ketoglutarate production, disrupting TCA cycle anaplerosis and diminishing ATP generation. (58)

The therapeutic promise supported by *in vitro* studies confronts a remarkable obstacle when investigated in animal models of PDAC. In one study, GOT2 knockdown had no effect on tumor growth in subcutaneous xenografts across five different PDAC cell lines, orthotopic pancreatic tumors, or in autochthonous KC-GOT2 genetically engineered mouse models. Tumors lacking GOT2 maintained proliferative capacity, exhibiting modestly increased Ki67 staining rather than growth suppression. (58) In another recent paper, researchers describe a non-canonical function of GOT2, profoundly impacting antitumor immunity. This occurs when GOT2 localizes not only to the mitochondria but also to the nucleus in PDAC cells, which is not observed in normal tissue. (59) In the nucleus, GOT2 purportedly functions as a fatty acid binding protein that directly binds ligands such as arachidonic acid and facilitates their interaction with peroxisome proliferator-activated receptor delta (PPARδ), a nuclear receptor that regulates transcriptional programs. This GOT2-PPARδ axis drives profound immunosuppression by promoting spatial restriction of CD4+ and CD8+ T cells from the tumor microenvironment. In this study, GOT2 knockout increased cytotoxic T cell infiltration into tumors, and engineering GOT2 with a forced nuclear localization signal (NLS) enhances T cell exclusion without affecting tumor growth directly. (59) In an effort to bring some clarity to the role of GOT1 and GOT2 in PDAC metabolism, Chapter 2 of

this thesis describes our experiments utilizing various models of individual and combined knockouts of these aminotransferases.

1.6 PDAC Surveillance Guidelines

Although there is currently no widely accepted protocol for pancreatic cancer screening, most physicians recommend targeting patients who are known to be at a higher risk due to family history or have the presence of some of the associated conditions listed above. Different medical organizations, including the U.S. Preventative Services Task Force (USPSTF), the International Cancer of the Pancreas Screening (CAPS) Consortium, and the American Gastroenterological Association (AGA) have issued specific criteria in order to identify the individuals for whom they believe pancreatic cancer screening is warranted. (60-63)

1.6.1 USPSTF recommendations

In its 2019 report, the USPSTF found no evidence that screening for PDAC is effective in reducing mortality and recommends against routine screening in asymptomatic adults using abdominal palpation, ultrasonography, or serologic markers. However, they did not review the effectiveness of screening individuals at high risk for PDAC and thus issued no determination in regard to that population. (60)

1.6.2 International CAPS Consortium recommendations

Composed of 49 multidisciplinary experts, the International CAPS Consortium provided its initial consensus guidelines in 2012 and then provided an update in 2020. They recommend screening for stage I PDAC and PDAC precursor lesions with high-grade dysplasia in the following high-risk groups:

- All patients with Peutz-Jeghers syndrome
- All carriers of a *CDKN2A* mutation
- Carriers of a *BRCA2*, *BRCA1*, *PALB2*, *ATM*, *MLH1*, *MSH2*, or *MSH6* gene mutation with at least one affected first-degree relative
- Patients who have at least one first-degree relative with PDAC who in turn also have a first-degree relative with PDAC (61-62)

1.6.3 AGA recommendations

The AGA released a 2020 clinical practice guideline for identifying which patients should receive screening, with the expressed goal of detecting resectable stage 1 PDAC and high-risk precursor neoplasms such as IPMNs. Their guideline recommends screening in individuals who are first-degree relatives of patients with PDAC with at least two affected relatives, and in patients with genetic syndromes associated with an increased risk of PDAC, including all patients with the following diagnoses:

- Peutz-Jeghers syndrome
- Hereditary pancreatitis
- *CDKN2A* gene mutation
- One or more first-degree relatives with PDAC with Lynch syndrome
- Mutations in *BRCA1*, *BRCA2*, *PALB2*, and *ATM* genes

The AGA further recommends that relatives of PDAC patients should consider genetic testing. These results may uncover germline mutations that alert them to PDAC susceptibility or risk of other associated cancers. In terms of what age to initiate screening, the AGA encourages high-risk individuals to start at age 50, or 10 years

younger than the initial age of familial onset. For those with *CDKN2A* or *PRSS1* mutations, screening should begin at 40 years of age, and if a patient has Peutz-Jeghers syndrome, then age 35 is appropriate. Additionally, they suggest that patients who are undergoing screening should participate in a registry to track cases and potentially uncover additional contributing factors to PDAC progression. Like the USPSTF guidelines, the AGA recommends against screening average-risk individuals for PDAC. (63)

1.7 Diagnostic Imaging in PDAC

There are a number of imaging techniques used singly and in combination to diagnose PDAC and monitor progression over time (64-65). This section will provide a brief overview of these techniques and highlight the benefits and limitations of each modality.

1.7.1 Ultrasonography and Endoscopic Ultrasound

A PDAC ultrasound (US) protocol can fall into one of two categories: a non-invasive abdominal US or an endoscopic ultrasound (EUS), which involves placing a flexible endoscope down the throat into the stomach and duodenum. Both procedures use sound waves to generate images of pertinent abdominal organs, including the pancreas, bile duct, and gastrointestinal tract. The abdominal US would typically be used for a quick, initial patient screening. Of all the imaging techniques, it is the least expensive, most widely available, and quickest to perform. Abdominal US does not provide adequate imaging of smaller tumors or those in the tail of the pancreas, which are less accessible externally. EUS provides higher resolution imaging, which allows the

investigation of more subtle structures. If a suspicious mass is identified, an EUS-guided fine needle aspiration (EUS-FNA) can be performed to provide a transcutaneous tissue biopsy. This offers the opportunity for a definitive PDAC diagnosis via a pathologist's histologic assessment. As such, EUS-FNA is often utilized as a confirmatory step even when alternate imaging techniques are employed. (64-65) EUS-FNA for pancreatic cancer is generally safe, but complications can occur, primarily acute pancreatitis, mild bleeding, infection, and pain, with major complication rates around 2.5% and very low mortality. A rare but serious concern is needle tract seeding, where cancer cells spread along the needle path, though studies suggest it's uncommon and doesn't significantly worsen survival. The overall risk of severe morbidity is low, but monitoring for pancreatitis and pain is crucial. (66)

For both forms of US, the technique is very operator-dependent, thus representing a substantial limitation to its efficacy. (67) Furthermore, tumors that cause diffuse infiltration or all or part of the pancreas without changing gland contours may be poorly imaged with US. Imaging may be obscured in patients with obesity or when gas is present in the stomach or bowel, however a full bladder can help to displace gas and improve resolution. (68-69) Additional methods to augment structure visualization would be to use contrast-enhanced US, which offers greater differentiation between potential lesions of interest and background tissues.

1.7.2 Computed Tomography

Computed tomography (CT) is a primary imaging modality for diagnosis and staging of PDAC, due in large part to its broad availability, short scan time, and detailed

cross-sectional images, which provides excellent spatial resolution. (69-70) CT utilizes a series of X-ray scans taken at multiple angles in order to produce a 3-dimensional rendering of the region of interest. This method particularly excels at visualizing the anatomical relationship of the tumor to major vessels, such as whether the mass is encasing local arteries or veins. CT can also be used to assess local metastases to the liver, lymph nodes, or other vital abdominal organs. Given these characteristics, CT can provide critical information relevant to surgical planning and determining candidacy for tumor resection. (71) Unfortunately, CT comes with several considerable drawbacks as well. Although this technology provides a high degree of spatial resolution, it has relatively poor contrast resolution, meaning that it is often unable to differentiate between tissues of similar densities. As such, CT does not provide strong resolution between soft tissues when compared to other imaging strategies, which limits its efficacy in detecting isoattenuating or infiltrative tumors. Small tumors also present a challenge for CT, and it is estimated that up to 40% of pancreatic tumors less than 2 cm wide may be missed, which significantly impacts early-stage diagnosis. (71-73) Furthermore, CT scans expose patients to ionizing radiation, which should be minimized as much as possible in all individuals, particularly when other non-radiation-producing alternatives exist. (70)

1.7.3 Positron Emission Tomography

While CT scans provide the size, shape, and location of target structures, positron emission tomography (PET) scans provide information about altered metabolic activity of cells within the body, particularly as it relates to glucose metabolism. ^{18}F-Fluorodeoxyglucose (^{18}F-FDG) is a glucose analog radiotracer that is commonly used in

the context of PET imaging, and it functions by accumulating in tissues with high glucose demand, such as tumors and areas of high inflammation. (74) The PET scan is able to read the signal generated by the metabolized ^{18}F-FDG and therefore the regions of high activity suggest the location of a malignant tumor. Most often, PET is combined with CT or magnetic resonance imaging (MRI) to provide both metabolic information as well as anatomical location. (75-76) PET/CT and PET/MRI can also detect distant or occult metastatic disease that may not be visible on standard CT or MRI alone. (77-78) The effectiveness of PET for initial PDAC diagnosis remains a point of contention amongst clinicians, because although it has a high specificity and avoids false positive diagnoses, it has a lower sensitivity than other diagnostic modalities and is more susceptible to false negatives. (73) One study demonstrated a diagnostic delay when PET/CT imaging was added to the protocol, extending time to surgery by 16-43 days, which may be critical in a scenario with an aggressive tumor (77). The presence of ionizing radiation from the ^{18}F-FDG is an additional area of slight concern, although the levels are fairly modest.

1.7.4 Magnetic Resonance Imaging

MRI offers distinct advantages for the diagnosis and characterization of PDAC, particularly due to its superior soft tissue contrast and ability to non-invasively evaluate pancreatic ducts and surrounding structures. (79) This high contrast resolution allows the MRI to differentiate more effectively between a true PDAC diagnosis and other pancreatic lesions such as cystic tumors and focal pancreatitis. (79) MRI with diffusion-weighted imaging (DWI) enhances sensitivity for detecting small or isoattenuating tumors, which may be missed by CT. (80)

Unique from both PET and CT imaging, MRI relies on the activity of positively-charged hydrogen atoms to create a signal which can be then used to generate an image. Briefly, the magnetic field within the MRI machine aligns the protons in the body's hydrogen atoms and then radiofrequency pulses are emitted to knock the protons out of alignment. Once these pulses are turned off, the protons are able to relax and return to their aligned state, which causes them to release energy. This energy is picked up by the MRI sensors and creates an image. (81) Property differences between normal and cancerous tissue, such as water content, altered vascularity, and cellular density cause changes to the proton relaxation time, allowing for abnormalities to be highlighted on the scan. To enhance the imaging, gadolinium-based contrast agents are often administered to patients prior to MRI. These agents accumulate in the tumors due to their leaky vessels. (82) In order to target visualization of the pancreatic and biliary ducts, a modified procedure known as magnetic resonance cholangiopancreatography (MRCP) can be performed. MRCP excels at depicting the ductal anatomy and pathology, but contributes limited information on solid tumor characteristics or resectability unless combined with full MRI (83) An added benefit of MRI is that it involves no ionizing radiation, unlike CT and PET scans, and therefore serial imaging does not carry any additional radiation burden. (84-85)

1.7.4.1 Latest advancements in MRI for PDAC

MRI for PDAC has evolved from purely anatomic assessment to a multiparametric and increasingly quantitative platform that probes vascularity, cellularity, fibrosis, and metabolism. Recent advances focus on higher-field and accelerated acquisition, diffusion and perfusion modeling, radiomics and artificial intelligence, and

emerging targeted or functional contrast approaches, all aimed at improving detection of small lesions, characterization of fibrosis-rich tumors, and prediction of treatment response. (86-88) These technologies seek to complement or, in selected scenarios, challenge contrast-enhanced CT by offering better soft-tissue contrast, non-ionizing imaging, and access to microstructural information that is especially relevant in a dense, desmoplastic cancer such as PDAC.

Higher field strengths (3T and above) with modern multichannel coils improve signal-to-noise and spatial resolution, allowing more reliable depiction of small pancreatic and peri-pancreatic lesions and finer ductal and vascular detail. Compressed sensing and parallel imaging have enabled faster dynamic contrast-enhanced (DCE) sequences and high-resolution MRCP, reducing motion artifacts and breath holding demands in often frail PDAC patients. Balanced optimization of sequence parameters at 3T, along with motion-robust T1/T2-weighted imaging and secretin-stimulated MRCP, has improved evaluation of main pancreatic duct strictures, early obstruction, and subtle parenchymal changes associated with early PDAC and high-grade PanIN in high-risk cohorts. (88-90)

Advanced DWI aims to separate true diffusion from microvascular perfusion and capture non-Gaussian diffusion behavior in the fibrotic tumor matrix. Diffusion metrics are also being tested as early biomarkers of response to chemotherapy and chemoradiation, with increases in diffusion indices after neoadjuvant therapy correlating with pathologic tumor regression and improved resectability in prospective and retrospective cohorts. (91-93)

Quantitative DCE-MRI techniques, using pharmacokinetic models, have been applied to PDAC to derive parameters like extracellular volume fraction and plasma volume that reflect microvascular permeability and perfusion. (94) Studies over the last few years indicate that PDAC typically exhibits low perfusion and restricted enhancement compared with normal pancreas, and that DCE-derived metrics can help distinguish PDAC from inflammatory masses and predict response, with lower baseline perfusion often associated with chemoresistance and poorer outcome. (95) In parallel, quantitative T1 and T2 mapping and MRI elastography techniques are being explored to noninvasively characterize pancreatic fibrosis and stiffness, aiming to capture the extensive desmoplastic reaction that is central to PDAC biology and may influence drug penetration and immunotherapy response. (96)

Radiomics and machine-learning approaches applied to multiparametric MRI (T1/T2, DWI, DCE, and MRCP) represent one of the most active areas of technological development in PDAC imaging. (91-92) Recent work shows that texture features and shape descriptors extracted from pancreatic MRI can differentiate PDAC from chronic pancreatitis, stratify molecular subtypes, and predict nodal involvement, margin status, or survival, often outperforming single radiologist assessments in retrospective analyses. Deep learning-based segmentation and classification networks are increasingly being trained on large MRI datasets to automate pancreas and tumor delineation, detect subtle lesions, and integrate imaging with genomic and clinical variables, supporting precision risk stratification and treatment planning in PDAC. (97)

Although early in clinical translation, molecular MRI strategies for PDAC are progressing, including targeted gadolinium or iron-oxide agents that bind to

overexpressed biomarkers such as integrins, stromal components, or specific receptors on cancer cells and associated fibroblasts. Preclinical and early phase clinical studies have also explored pH-sensitive and metabolic probes, as well as chemical exchange saturation transfer (CEST) techniques, to interrogate tumor metabolism, acidosis, and extracellular matrix composition in PDAC in a noninvasive manner. (98) These molecular and functional MRI tools are being positioned as complementary to FDG-PET and CT, with the goal of providing target-specific contrast for earlier detection, improved delineation of viable tumor within fibrotic tissue, and more precise monitoring of targeted therapies and immunotherapies in PDAC.

As with the other modalities, MRI does have challenges associated with imaging PDAC effectively for diagnosis. The protocols are often more complex than alternative imaging, requiring long scan times that can be susceptible to artifacts from patient movement or intestinal gas. The gadolinium-based contrast agents may also accumulate in brain tissue, which could be concerning with repeated exposure, although the literature is not resolved on its overall long-term impact. (99-101)

1.8 Current Limitations in Diagnostic Imaging

PDAC remains one of the deadliest malignancies primarily due to late-stage diagnosis. Despite advances in the imaging technology described above, significant unmet clinical needs persist in the diagnostic imaging landscape for PDAC, limiting early detection, accurate staging, and timely intervention.

1.8.1 Early detection and screening limitations

Inadequate sensitivity for small and early-stage tumors represents a critical unmet need. Conventional contrast-enhanced computed tomography (CT), the standard imaging modality for PDAC diagnosis, demonstrates overall sensitivity of 89% and specificity of 90%. However, its performance deteriorates dramatically for small lesions, with sensitivity dropping to around 60-70% for tumors ≤2 cm. Nearly 40% of pancreatic tumors remain undetected at early stages, resulting in most patients presenting with unresectable disease. (102-103)

Isoattenuating tumors pose particular diagnostic challenges. These lesions, representing between 5-12% of PDACs, exhibit attenuation differences of less than 15 Hounsfield units compared to surrounding pancreatic parenchyma, rendering them essentially invisible on standard CT imaging. Isoattenuating tumors are characteristically smaller (12-25 mm, compared to 30-40 mm for hypoattenuating tumors) and must be detected through indirect signs such as pancreatic duct dilatation, ductal interruption, or pancreatic atrophy. Paradoxically, these tumors have better prognoses when detected, with higher resectability rates (85-100%) compared to hypoattenuating lesions. (104-106)

As mentioned earlier, a lack of validated screening tools for asymptomatic populations remains a fundamental barrier. The USPSTF has assigned a “grade D" recommendation for PDAC screening in the general population due to the low prevalence (~12 per 100,000) and high false-positive rates even with tests having 99% specificity. This low positive predictive value would result in approximately 990 individuals undergoing unnecessary imaging and associated anxiety for every true positive case. Asymptomatic PDAC detection is rare, yet when achieved, it correlates

with earlier stage at presentation, higher resectability rates (64% versus 36%), and significantly improved 5-year survival (18% versus 7%) compared to symptomatic disease. (107-108)

1.8.2 Biomarker and Imaging Integration Gaps

CA19-9, the most established serum biomarker, has insufficient sensitivity and specificity for early detection. At the standard clinical cutoff of 37 U/mL, CA19-9 demonstrates only 76% sensitivity and 79% specificity. Its performance for early-stage disease detection is particularly poor, requiring a cutoff as low as 2.0 U/mL to achieve 95% sensitivity—which yields only 2% specificity, rendering it clinically useless for screening. Additionally, CA19-9 lacks specificity for PDAC, as it can be elevated in benign conditions including chronic pancreatitis and cholangitis. (109-111) Recent multi-laboratory validation studies have identified biomarker combinations that improve performance. CA19-9 combined with the glycan biomarker CA199.STRA achieved 71% sensitivity at 98% specificity, compared to 44% sensitivity for CA19-9 alone. Three-marker panels including CA19-9, LRG1, and CA199.STRA demonstrated 89% sensitivity at 65% specificity. However, these panels require further validation before clinical implementation. (111)

1.8.3 Differential diagnosis challenges

Distinguishing PDAC from mass-forming chronic pancreatitis and autoimmune pancreatitis represents a persistent diagnostic dilemma with significant clinical implications. The imaging features of these maladies substantially overlap across CT, MRI, and PET-CT. Misdiagnosis of chronic pancreatitis as PDAC leads to unnecessary

surgical intervention and patient burden, while the converse error delays potentially curative treatment. (112-113) Key differentiating features have limited reliability. While delayed contrast enhancement >70.5 Hounsfield units showed 84.2% sensitivity and 84.7% specificity for distinguishing chronic mass-forming pancreatitis from PDAC, many cases remain ambiguous. The "duct-penetrating sign" on MRCP is more suggestive of chronic pancreatitis, while abrupt ductal cutoff and the "double-duct sign" favor PDAC. However, these findings are neither perfectly sensitive nor specific. (112-113)

While somewhat uncommon, there have also been several reports of IgG4-related autoimmune pancreatitis closely mimicking PDAC clinically and radiologically and leading to a challenging diagnosis. While serum IgG4 levels >135 mg/dL demonstrate 95% sensitivity and 97% specificity for autoimmune pancreatitis, approximately 10% of pancreatic cancers also present with elevated IgG4. DWI on MRI cannot reliably differentiate PDAC from focal pancreatitis due to overlapping apparent diffusion coefficient (ADC) values related to inflammation and fibrosis in both conditions. (90, 115)

1.8.4 Staging Accuracy and Resectability Assessment

Inaccurate assessment of vascular involvement and borderline resectability remains problematic. The positive predictive value of CT for determining unresectability is high (89-100%), but its ability to predict resectability is substantially lower (45-79%). This discrepancy is particularly pronounced after neoadjuvant therapy, where CT fails to distinguish tumor from inflammation and fibrosis. (116-117)

1.8.5 Technical and Practical Limitations

Contrast agent toxicity and contraindications limit imaging options for vulnerable patients. Iodinated CT contrast carries risks of contrast-induced acute kidney injury, particularly in patients with pre-existing renal impairment, with incidence reported at 12-50% in some studies. Gadolinium-based MRI contrast agents, while generally safer, can cause nephrogenic systemic fibrosis in patients with severe kidney disease and have been associated with gadolinium deposition in tissues, as previously stated. These safety concerns restrict imaging frequency and modality selection in patients with comorbidities who would benefit most from enhanced surveillance. (118-120)

Limited accessibility and expertise with EUS restrict its utilization despite superior diagnostic performance. EUS demonstrates greater than 90% sensitivity for PDAC detection and enables tissue acquisition, with 90% sensitivity for confirming even isoattenuating tumors via fine-needle aspiration. However, EUS programs face substantial barriers including high initial investment and recurrent costs, need for on-site cytopathology support, and a high clinical training threshold required for competency. These barriers are particularly pronounced in developing countries and smaller healthcare institutions. (69, 121-122)

Lastly, radiation exposure from repeated CT imaging presents cumulative risk concerns, particularly for high-risk individuals requiring surveillance. While non-contrast CT reduces radiation dose, it has limited utility for PDAC detection and staging. This constraint necessitates careful risk-benefit balancing in surveillance protocols. (123)

1.8.6 Emerging Technologies with Translation Gaps

Artificial intelligence and radiomics models show promise but face significant implementation barriers. Deep learning models have achieved high marks for PDAC detection, with some demonstrating superior performance to radiologists, particularly for subtle or small tumors. AI-based analysis of prediagnostic CT scans obtained 6-36 months before clinical diagnosis achieved 89.3% accuracy, 86% sensitivity, and 93% specificity for identifying individuals at risk. (124-125) However, multiple obstacles prevent clinical adoption. Data heterogeneity from varying scanner types, imaging protocols, and reconstruction algorithms introduces inconsistencies in radiomics features, compromising model generalizability. Limited datasets, lack of standardized protocols for feature extraction and preprocessing, and insufficient external validation studies restrict clinical translation. The computational infrastructure requirements, including high-performance processing units and large-scale storage systems, are prohibitively expensive for many institutions. Regulatory barriers, unclear liability frameworks, and the opaque nature of many AI models that lack interpretability further impede adoption. (126-127)

Standardization of imaging protocols across institutions also remains incomplete. While successful multisite standardization protocols have been developed for pancreatic MRI with coefficients of variation <10% for quantitative parameters, these protocols have not achieved universal adoption. Variability in imaging acquisition continues to complicate multicenter studies and data pooling efforts essential for AI model development. (126,128)

While molecular imaging with targeted probes offers great promise, to this point it remains largely investigational. Peptide-based probes targeting receptors

overexpressed in PDAC (such as integrin αvβ3, plectin, and low-density lipoprotein receptor) have shown encouraging preclinical results and radiolabeled probes like 68Ga-RAD 301 targeting αvβ6-integrin demonstrate strong imaging potential. However, most remain in early clinical trials without established efficacy, optimal radionuclide selection, or regulatory approval for routine clinical use. (129-131)

Liquid biopsy technologies also show potential but, likewise, require further validation. Circulating cell-free DNA (cfDNA) methylation panels, exosomal microRNAs, and multi-analyte approaches have demonstrated impressive performance in development cohorts, with some achieving 97% detection rates for stage I-II PDAC when combined with CA19-9. However, these technologies face challenges related to specificity in diverse populations, cost-effectiveness, standardization across laboratories, and the need for large-scale prospective validation in asymptomatic at-risk populations before implementation in clinical practice. (132-134)

1.8.7 Critical Gaps in High-Risk Surveillance

The absence of consensus protocols for high-risk individual surveillance limits systematic early detection efforts. While the American Gastroenterological Association and American Society for Gastrointestinal Endoscopy have endorsed selective surveillance using EUS, MRI, and/or CT for high-risk individuals, standardized protocols for imaging frequency, modality selection, and reporting remain incompletely implemented. The International Cancer of the Pancreas Screening consortium has made progress in standardization, but disparities in access, expertise, and resources persist. (135-136)

A lack of validated risk stratification tools to identify which asymptomatic individuals warrant intensive surveillance further hampers screening efficiency. The Enriching New-onset Diabetes for Pancreatic Cancer (END-PAC) score, which increases PDAC incidence identification from 0.8% to 3.6% with 78% sensitivity and 82% specificity, represents progress but requires broader validation. Machine learning models analyzing electronic health record data have achieved improvments for predicting PDAC within 36 months, yet these tools have not been widely translated into clinical decision support systems. (137)

The diagnostic imaging landscape for PDAC faces fundamental unmet needs spanning early detection capabilities, biomarker integration, differential diagnosis accuracy, metastatic disease assessment, and technology translation. Addressing these unmet needs requires coordinated efforts in multiple domains: development and validation of standardized imaging protocols across institutions, rigorous external validation of AI models in diverse populations, integration of complementary biomarker panels with imaging, advancement of molecular imaging probes through clinical trials, establishment of infrastructure to support computational imaging analysis, creation of regulatory frameworks for AI diagnostic tools, and implementation of evidence-based surveillance protocols for high-risk populations. Only through such comprehensive approaches can the field overcome current limitations and achieve the transformative goal of detecting PDAC at curable stages.

1.9 Polyethylene Glycol (PEG) in Medicine

Polyethylene glycol (PEG) has become a cornerstone in modern pharmaceutical and biomedical applications, ranging from simple laxatives to complex drug delivery

systems. This synthetic, water-soluble polymer consists of repeating ethylene glycol units and is valued for its unique physicochemical properties, including biocompatibility, low immunogenicity, and versatility in conjugation chemistry. The covalent attachment of PEG chains to therapeutic molecules, termed PEGylation, represents one of the most significant advances in pharmaceutical biotechnology. This modification profoundly alters the pharmacokinetic and pharmacodynamic profiles of drugs, particularly proteins and peptides that would otherwise be rapidly cleared from circulation. (138-139)

PEGylation improves therapeutic efficacy through several mechanisms, including increased hydrodynamic size, steric shielding, reduced immunogenicity, enhanced solubility, and decreased reticuloendothelial system clearance. (138-142) As of 2025, the FDA has approved over 40 PEGylated drugs, for indications as wide-ranging as Hepatitis B and C (peginterferon alfa-2a), neutropenia (pegfilgrastim), gout (pegloticase), leukemia (pegaspargase), and opioid antagonism (naloxegol). (143) Both linear and branched PEG structures are employed in marketed drugs. Branched PEG reagents, consisting of two PEG molecules linked to a central core, provide higher PEG density per modification site and offer advantages such as increased stability and prolonged circulation compared to linear counterparts. (144-145) PEGylation has also revolutionized nanoparticle-based drug delivery by conferring properties that enable nanocarriers to evade immune surveillance. PEG coatings with molecular weights exceeding 20 kDa create thick hydration layers that minimize protein adsorption and immune recognition, extending circulation time and enhancing therapeutic effectiveness. (138, 142, 146)

The first clinically approved PEGylated nanoparticle formulation was Doxil (PEGylated liposomal doxorubicin), approved in 1995 for ovarian cancer, multiple myeloma, and AIDS-related Kaposi's sarcoma. Doxil demonstrates improved circulation half-life, slower plasma clearance, and reduced volume of distribution compared to free doxorubicin. PEGylated liposomes achieve drug loading capacities up to 90% and have shown disease control rates of 73% in colorectal cancer patients treated with encapsulated CPX-1. (142) Recent advances include PEGylated liposomes synthesized via atom transfer radical polymerization (ATRP), which allows controlled and uniform PEG grafting onto liposome surfaces. This method enhances stability, provides prolonged circulation, and improves blood-brain barrier penetration compared to conventional PEGylation approaches. (147)

PEG hydrogels have emerged as versatile biomaterials for wound healing, tissue scaffolding, and regenerative medicine applications. PEG-based hydrogels demonstrate superior wound closure properties compared to commercial products. In preclinical studies, PEG hydrogels applied to full-thickness skin incisions in rats resulted in immediate hemostasis and accelerated wound closure. After 14 days, wounds treated with PEG hydrogels showed 77.2% collagen formation compared to 65.2% with commercial controls, and wound area was reduced by half when compared to control groups. The hydrogels' nontoxic, inert nature and ability to create a moist environment conducive to tissue regeneration make them excellent choices for medical dressings. (148) Multi-arm PEG derivatives are used in hydrogel formation for controlled therapeutic release in medical devices and regenerative medicine. PEG hydrogels serve as scaffolds for cell culture, providing a three-dimensional matrix with tunable

stiffness and porosity that mimics the physiological extracellular matrix. Bio-synthetic tissue scaffolds consisting of interpenetrating networks of gelatin methacrylamide polymerized within PEG frameworks have demonstrated excellent cell adhesion, cytoplasmic spreading, and ongoing viability for both adherent and encapsulated cells. (149) PEG hydrogels have been utilized to engineer tissue-specific constructs, including vascularized bone grafts using mesenchymal stem cells and periodontal treatments using stem cell-encapsulated gels to promote gum healing. Microporous annealed particle (MAP) hydrogels possess interconnected microporous structures that result in superior tissue regeneration compared to conventional nanoporous PEG hydrogels. (150)

1.9.1 PEG safety profile and adverse effects

PEG has a generally favorable safety profile and has been approved by regulatory authorities in most countries for intravenous, oral, and topical use. However, several adverse effects and complications have been documented. When used as a laxative, PEG can cause bloating, nausea, abdominal cramping, diarrhea, flatulence, and electrolyte imbalances including alterations in calcium, sodium, potassium, and phosphate levels. There is also a risk of metabolic acidosis, characterized by acid and toxin accumulation. (151) Although rare, PEG allergy can occur and may result in severe anaphylactic reactions. Studies suggest that up to 72% of people have at least some antibodies against PEG, likely due to exposure through cosmetics and pharmaceuticals, with approximately 7% having antibody levels high enough to predispose them to anaphylactic reactions. Allergic reactions to PEG have been

documented with both laxative formulations and COVID-19 vaccines containing PEGylated lipid nanoparticles. (152)

A significant limitation of repeated PEGylated drug administration is the accelerated blood clearance (ABC) phenomenon, where subsequent doses are rapidly eliminated from circulation due to the production of anti-PEG antibodies, particularly IgM. This immune response occurs as a T-independent mechanism mediated by marginal zone B cells in the spleen. (153-154) Studies demonstrate that a single intravenous administration of PEGylated proteins or liposomes can elicit anti-PEG IgM responses, leading to rapid clearance of subsequent doses. For instance, mice pretreated with PEGylated ovalbumin showed undetectable levels of the test dose at 24 hours post-injection, compared to 41.6% in control mice. Interestingly, anti-PEG IgM induced by PEGylated liposomes does not necessarily affect all PEGylated materials equally, suggesting specificity in the immune response. (154-155) Strategies to overcome the ABC effect include pre-infusion with high molecular weight free PEG (40 kDa), which can saturate circulating anti-PEG antibodies and restore prolonged circulation of PEGylated liposomes for at least 48 hours. Asymmetrical branched PEG modifications and slow intravenous infusion have also shown promise in reducing ABC phenomena. (156-157)

Despite the challenges of anti-PEG antibody formation, accelerated clearance upon repeat dosing, and potential immunogenic reactions, PEG has been widely used with well-documented benefits. In Chapter 3 of this thesis, I will describe a newly discovered utility of PEG as an agent to improve contrast in MR imaging of PDAC.

1.10 Arginine-Glycine-Aspartate (RGD) as a Therapeutic

Arginine-Glycine-Aspartate (RGD) peptides represent one of the most extensively studied cell adhesion sequences in biomedical research. This tripeptide motif serves as the primary recognition site in extracellular matrix (ECM) proteins and has evolved into a versatile platform for tumor-targeted drug delivery, molecular imaging, and tissue engineering applications. The RGD sequence functions as a critical cell adhesion motif that binds to integrin receptors, a family of transmembrane proteins mediating cell-ECM interactions. Eight integrin dimers recognize the RGD motif: αvβ1, αvβ3, αvβ5, αvβ6, αvβ8, α5β1, α8β1, and αIIbβ3. (158-161)

(**Figure 1-4**)

1.10.1 Linear vs. cyclic RGD peptides

The structural configuration profoundly impacts RGD peptide performance. Cyclic RGD peptides demonstrate markedly superior properties compared to linear forms in binding affinity, proteolytic stability, pharmacokinetics, and dissociation kinetics. Cyclic versions exhibit higher affinity for integrin receptors through conformational constraint that optimizes the spatial arrangement of arginine and aspartate residues. (161) The cyclic RGD are also approximately 30-fold more resistant to enzymatic degradation than their linear counterparts. (162) In regard to pharmacokinetics, linear RGD peptides have circulation half-lives of only around 2 minutes, while cyclic forms persist 10 times longer. (163) Lastly, steered molecular dynamics simulations reveal that cyclic RGD requires greater force to dissociate from integrin binding sites and takes longer to unbind compared to linear peptides (159). The rigid ring structure of cyclic peptides prevents conformational flexibility, maintaining stable interaction geometry with the integrin headpiece throughout binding. (164)

RGD peptides display differential binding affinities across integrin subtypes. Linear RGD peptides typically show highest activity toward αvβ3, with moderate affinity for αvβ5 and α5β1, while exhibiting selectivity against αvβ6, αvβ8, and αIIbβ3. (164-165) Emerging computational design approaches have achieved remarkable selectivity improvements, with engineered miniproteins demonstrating picomolar affinity and greater than 1000-fold selectivity for single integrin subtypes like αvβ6 or αvβ8 over other RGD-binding integrins. (166)

1.10.2 RGD use in cancer treatment

RGD peptides have garnered substantial attention for cancer therapy research due to αvβ3 and αvβ5 integrin overexpression on tumor vasculature and certain cancer cells. The tumor-targeting mechanism exploits preferential integrin expression in angiogenic blood vessels and tumor cells while these receptors remain largely absent in normal tissues. (167-169) RGD modification of chemotherapeutic agents, particularly doxorubicin, has demonstrated significant therapeutic enhancements. Pre-modified RGD-doxorubicin conjugates showed substantial tumor suppression both *in vitro* and *in vivo*. (167) RGD-functionalized nanoparticles demonstrate improved tumor accumulation while minimizing systemic toxicity. (168-169) The design of cleavable linkers connecting RGD peptides to drug cargos has been a huge area of development in the last 20 years. (168)

The cyclic nonapeptide iRGD represents a sophisticated evolution of conventional RGD peptides, incorporating dual-targeting capability through a multistep mechanism. (170-172) iRGD initially binds αvβ3 and αvβ5 integrins on tumor vasculature via its RGD motif. Tumor-associated proteases cleave the peptide to

expose a cryptic C-end Rule (CendR) motif (CRGDK). The exposed CendR motif binds neuropilin-1 (NRP-1) receptors, triggering active transcytosis and deep tissue penetration. This mechanism enables iRGD and co-administered drugs to penetrate tumor parenchyma far more effectively than conventional RGD peptides, which remain confined to tumor vasculature. (172-173) In Chapter 3 of this thesis, I will describe how the aforementioned features of iRGD can be exploited to improve pancreatic tumor imaging when used in combination with PEG.

1.11 References

1. Talathi, S. S., Omole, A. E., & Young, M. (2025). Anatomy, abdomen and pelvis, pancreas. In *StatPearls [Internet]*. StatPearls Publishing.

2. Leung, P. S. (2010). Overview of the pancreas. *The renin-angiotensin system: current research progress in the pancreas: the RAS in the pancreas*, 3-12.

3. Helbing, A., Menon, G., & Tuma, F. (2025). Pancreatic Neuroendocrine Tumors. *StatPearls*.

4. Dasari, A., Shen, C., Halperin, D., Zhao, B., Zhou, S., Xu, Y., ... & Yao, J. C. (2017). Trends in the incidence, prevalence, and survival outcomes in patients with neuroendocrine tumors in the United States. *JAMA oncology*, *3*(10), 1335-1342.

5. Niger, M., Prisciandaro, M., Antista, M., Monica, M. A. T., Cattaneo, L., Prinzi, N., ... & Di Bartolomeo, M. (2020). One size does not fit all for pancreatic cancers: A review on rare histologies and therapeutic approaches. *World journal of gastrointestinal oncology*, *12*(8), 833.

6. Park, W., Chawla, A., & O'Reilly, E. M. (2021). Pancreatic cancer: a review. *Jama*, *326*(9), 851-862.

7. American Cancer Society. Signs and Symptoms of Pancreatic Cancer [Internet]. www.cancer.org. 2024. Available from: https://www.cancer.org/cancer/types/pancreatic-cancer/detection-diagnosis-staging/signs-and-symptoms.html

8. Stefanoudakis, D., Frountzas, M., Schizas, D., Michalopoulos, N. V., Drakaki, A., & Toutouzas, K. G. (2024). Significance of TP53, CDKN2A, SMAD4 and KRAS in Pancreatic Cancer. *Current Issues in Molecular Biology*, *46*(4), 2827-2844.

9. Xie, T., Musteanu, M., Lopez-Casas, P. P., Shields, D. J., Olson, P., Rejto, P. A., & Hidalgo, M. (2015). Whole exome sequencing of rapid autopsy tumors and xenograft models reveals possible driver mutations underlying tumor progression. *PloS one*, *10*(11), e0142631.

10. Gu, Y., Ji, Y., Jiang, H., & Qiu, G. (2020). Clinical effect of driver mutations of KRAS, CDKN2A/P16, TP53, and SMAD4 in pancreatic cancer: a meta-analysis. *Genetic Testing and Molecular Biomarkers*, *24*(12), 777-788.

11. Ottenhof, N. A., de Wilde, R. F., Maitra, A., Hruban, R. H., & Offerhaus, G. J. A. (2011). Molecular characteristics of pancreatic ductal adenocarcinoma. *Pathology research international*, *2011*(1), 620601.

12. Karamitopoulou, E. (2019). Tumour microenvironment of pancreatic cancer: immune landscape is dictated by molecular and histopathological features. *British journal of cancer*, *121*(1), 5-14.

13. He, Y., Huang, W., Tang, Y., Li, Y., Peng, X., Li, J., ... & Huang, X. (2023). Clinical and genetic characteristics in pancreatic cancer from Chinese patients revealed by whole exome sequencing. *Frontiers in Oncology*, *13*, 1167144.

14. American Cancer Society. Cancer Facts & Figures 2025. Atlanta: American Cancer Society; 2025.

15. National Cancer Institute. (2025). Surveillance, epidemiology, and end results (SEER) program. *Cancer Statistics, SEER Data & Software, Registry Operations*.

16. Ushio, J., Kanno, A., Ikeda, E., Ando, K., Nagai, H., Miwata, T., ... & Yamamoto, H. (2021). Pancreatic ductal adenocarcinoma: Epidemiology and risk factors. *Diagnostics*, *11*(3), 562.

17. Bekkali, N. L., & Oppong, K. W. (2017). Pancreatic ductal adenocarcinoma epidemiology and risk assessment: Could we prevent? Possibility for an early diagnosis. *Endoscopic ultrasound*, *6*(Suppl 3), S58-S61.

18. Gupta, P., Murad, R., Ling, L., Zhang, Y., Duong-Polk, K., Huang, W., ... & Commisso, C. (2025). The Aging Microenvironment is a Determinant of Immune Exclusion and Metastatic Fate in Pancreatic Cancer. *Cancer research*.

19. Raffenne, J., Martin, F. A., Nicolle, R., Konta, M., Blum, Y., Torrisani, J., ... & Cros, J. (2021). Pancreatic ductal adenocarcinoma arising in young and old patients displays similar molecular features. *Cancers*, *13*(6), 1234.

20. Yang, J., Wen, C., Guo, H., Chai, Y., Sun, G., & Cheng, H. (2025). Targeting early diagnosis and treatment of pancreatic cancer among the diabetic population: a comprehensive review of biomarker screening strategies. *Diabetology & Metabolic Syndrome*, *17*(1), 176.

21. Aune, D., Greenwood, D. C., Chan, D. S. M., Vieira, R., Vieira, A. R., Rosenblatt, D. N., ... & Norat, T. (2012). Body mass index, abdominal fatness and pancreatic cancer risk: a systematic review and non-linear dose–response meta-analysis of prospective studies. *Annals of oncology*, *23*(4), 843-852.

22. Guerra, C., Schuhmacher, A. J., Cañamero, M., Grippo, P. J., Verdaguer, L., Pérez-Gallego, L., ... & Barbacid, M. (2007). Chronic pancreatitis is essential for induction of pancreatic ductal adenocarcinoma by K-Ras oncogenes in adult mice. *Cancer cell*, *11*(3), 291-302.

23. Pergolini, I., Sahora, K., Ferrone, C. R., Morales-Oyarvide, V., Wolpin, B. M., Mucci, L. A., ... & Fernández-del Castillo, C. (2017). Long-term risk of

pancreatic malignancy in patients with branch duct intraductal papillary mucinous neoplasm in a referral center. *Gastroenterology*, *153*(5), 1284-1294.

24. Lynch, S. M., Vrieling, A., Lubin, J. H., Kraft, P., Mendelsohn, J. B., Hartge, P., ... & Stolzenberg-Solomon, R. Z. (2009). Cigarette smoking and pancreatic cancer: a pooled analysis from the pancreatic cancer cohort consortium. *American journal of epidemiology*, *170*(4), 403-413.

25. Tramacere, I., Scotti, L., Jenab, M., Bagnardi, V., Bellocco, R., Rota, M., ... & La Vecchia, C. (2010). Alcohol drinking and pancreatic cancer risk: a meta-analysis of the dose-risk relation. *International journal of cancer*, *126*(6), 1474-1486.

26. Ali, A., Chianese, U., Papulino, C., Toraldo, A., Abakar, M. E. A., Passaro, E., ... & Benedetti, R. (2022). Metabolic pathways as a novel landscape in pancreatic ductal adenocarcinoma. *Cancers*, *14*(15), 3799.

27. Ying, H., Kimmelman, A. C., Lyssiotis, C. A., Hua, S., Chu, G. C., Fletcher-Sananikone, E., ... & DePinho, R. A. (2012). Oncogenic Kras maintains pancreatic tumors through regulation of anabolic glucose metabolism. *Cell*, *149*(3), 656-670.

28. Chang, X., Liu, X., Wang, H., Yang, X., & Gu, Y. (2022). Glycolysis in the progression of pancreatic cancer. *American Journal of Cancer Research*, *12*(2), 861.

29. Zhang, Y., Li, W., Niu, J., Fan, Z., Li, X., & Zhang, H. (2025). Reprogramming of glucose metabolism in pancreatic cancer: mechanisms, implications, and therapeutic perspectives. *Frontiers in Immunology*, *16*, 1586959.

30. Kamphorst, J. J., Nofal, M., Commisso, C., Hackett, S. R., Lu, W., Grabocka, E., ... & Rabinowitz, J. D. (2015). Human pancreatic cancer tumors are nutrient poor and tumor cells actively scavenge extracellular protein. *Cancer research*, *75*(3), 544-553.

31. Bott, A. J., Shen, J., Tonelli, C., Zhan, L., Sivaram, N., Jiang, Y. P., ... & Zong, W. X. (2019). Glutamine anabolism plays a critical role in pancreatic cancer by coupling carbon and nitrogen metabolism. *Cell reports*, *29*(5), 1287-1298.

32. Son, J., Lyssiotis, C. A., Ying, H., Wang, X., Hua, S., Ligorio, M., ... & Kimmelman, A. C. (2013). Glutamine supports pancreatic cancer growth through a KRAS-regulated metabolic pathway. *Nature*, *496*(7443), 101-105.

33. Lyssiotis, C. A., Son, J., Cantley, L. C., & Kimmelman, A. C. (2013). Pancreatic cancers rely on a novel glutamine metabolism pathway to maintain redox balance. *Cell Cycle*, *12*(13), 1987-1988.

34. Chakrabarti, G., Moore, Z. R., Luo, X., Ilcheva, M., Ali, A., Padanad, M., ... & Boothman, D. A. (2015). Targeting glutamine metabolism sensitizes pancreatic

cancer to PARP-driven metabolic catastrophe induced by ss-lapachone. *Cancer & metabolism*, *3*(1), 12.

35. Shen, X., Niu, N., & Xue, J. (2023). Oncogenic KRAS triggers metabolic reprogramming in pancreatic ductal adenocarcinoma. *Journal of translational internal medicine*, *11*(4), 322-329.

36. Reyes-Castellanos, G., Abdel Hadi, N., & Carrier, A. (2022). Autophagy contributes to metabolic reprogramming and therapeutic resistance in pancreatic tumors. *Cells*, *11*(3), 426.

37. Beatty, G. L., Werba, G., Lyssiotis, C. A., & Simeone, D. M. (2021). The biological underpinnings of therapeutic resistance in pancreatic cancer. *Genes & Development*, *35*(13-14), 940-962.

38. Michetti, F., Cirone, M., Strippoli, R., D'Orazi, G., & Cordani, M. (2025). Mechanistic insights and therapeutic strategies for targeting autophagy in pancreatic ductal adenocarcinoma. *Discover Oncology*, *16*(1), 1-17.

39. Michalopoulou, E., Auciello, F. R., Bulusu, V., Strachan, D., Campbell, A. D., Tait-Mulder, J., ... & Kamphorst, J. J. (2020). Macropinocytosis renders a subset of pancreatic tumor cells resistant to mTOR inhibition. *Cell reports*, *30*(8), 2729-2742.

40. Rainero, E. (2024). Macropinocytosis at the crossroad between nutrient scavenging and metabolism in cancer. *Current Opinion in Cell Biology*, *88*, 102359.

41. Rapozzi, V., Comuzzi, C., Di Giorgio, E., & Xodo, L. E. (2025). KRAS and NRF2 drive metabolic reprogramming in pancreatic cancer cells: the influence of oxidative and nitrosatice stress. *Frontiers in Cell and Developmental Biology*, *13*, 1547582.

42. Lim, J. K., & Leprivier, G. (2019). The impact of oncogenic RAS on redox balance and implications for cancer development. *Cell death & disease*, *10*(12), 955.

43. Durand, N., & Storz, P. (2017). Targeting reactive oxygen species in development and progression of pancreatic cancer. *Expert review of anticancer therapy*, *17*(1), 19-31.

44. Jain, P., Dvorkin-Gheva, A., Mollen, E., Malbeteau, L., Xie, M., Jessa, F., ... & Koritzinsky, M. (2021). NOX4 links metabolic regulation in pancreatic cancer to endoplasmic reticulum redox vulnerability and dependence on PRDX4. *Science advances*, *7*(19), eabf7114.

45. Chen, L., Zhang, Z., Hoshino, A., Zheng, H. D., Morley, M., Arany, Z., & Rabinowitz, J. D. (2019). NADPH production by the oxidative pentose-

phosphate pathway supports folate metabolism. *Nature metabolism*, *1*(3), 404-415.

46. De Santis, M. C., Porporato, P. E., Martini, M., & Morandi, A. (2018). Signaling pathways regulating redox balance in cancer metabolism. *Frontiers in oncology*, *8*, 126.

47. Lau, A. N., Li, Z., Danai, L. V., Westermark, A. M., Darnell, A. M., Ferreira, R., ... & Vander Heiden, M. G. (2020). Dissecting cell-type-specific metabolism in pancreatic ductal adenocarcinoma. *Elife*, *9*, e56782.

48. Li, D., Fu, Z., Chen, R., Zhao, X., Zhou, Y., Zeng, B., ... & Chen, R. (2015). Inhibition of glutamine metabolism counteracts pancreatic cancer stem cell features and sensitizes cells to radiotherapy. *Oncotarget*, *6*(31), 31151.

49. Yoo, H. C., Yu, Y. C., Sung, Y., & Han, J. M. (2020). Glutamine reliance in cell metabolism. *Experimental & molecular medicine*, *52*(9), 1496-1516.

50. Peng, H., Dou, H., He, S., Xie, Y. A., Zhang, Q., & Zheng, J. (2024). The role of GOT1 in cancer metabolism. *Frontiers in Oncology*, *14*, 1519046.

51. Murai, S., Ando, A., Ebara, S., Hirayama, M., Satomi, Y., & Hara, T. (2017). Inhibition of malic enzyme 1 disrupts cellular metabolism and leads to vulnerability in cancer cells in glucose-restricted conditions. *Oncogenesis*, *6*(5), e329-e329.

52. Simmen, F. A., Alhallak, I., & Simmen, R. C. (2020). Malic enzyme 1 (ME1) in the biology of cancer: it is not just intermediary metabolism. *Journal of molecular endocrinology*, *65*(4), R77-R90.

53. Kremer, D. M., Nelson, B. S., Lin, L., Yarosz, E. L., Halbrook, C. J., Kerk, S. A., ... & Lyssiotis, C. A. (2021). GOT1 inhibition promotes pancreatic cancer cell death by ferroptosis. *Nature communications*, *12*(1), 4860.

54. Patel, D., Menon, D., Bernfeld, E., Mroz, V., Kalan, S., Loayza, D., & Foster, D. A. (2016). Aspartate rescues S-phase arrest caused by suppression of glutamine utilization in KRas-driven cancer cells. *Journal of Biological Chemistry*, *291*(17), 9322-9329.

55. Garcia-Bermudez, J., Baudrier, L., La, K., Zhu, X. G., Fidelin, J., Sviderskiy, V. O., ... & Birsoy, K. (2018). Aspartate is a limiting metabolite for cancer cell proliferation under hypoxia and in tumours. *Nature cell biology*, *20*(7), 775-781.

56. Yang, S., Hwang, S., Kim, M., Seo, S. B., Lee, J. H., & Jeong, S. M. (2018). Mitochondrial glutamine metabolism via GOT2 supports pancreatic cancer growth through senescence inhibition. *Cell death & disease*, *9*(2), 55.

57. Sun, W., Luan, S., Qi, C., Tong, Q., Yan, S., Li, H., & Zhang, Y. (2019). Aspulvinone O, a natural inhibitor of GOT1 suppresses pancreatic ductal adenocarcinoma cells growth by interfering glutamine metabolism. *Cell Communication and Signaling*, *17*(1), 111.

58. Kerk, S. A., Lin, L., Myers, A. L., Sutton, D. J., Andren, A., Sajjakulnukit, P., ... & Lyssiotis, C. A. (2022). Metabolic requirement for GOT2 in pancreatic cancer depends on environmental context. *Elife*, *11*, e73245.

59. Abrego, J., Sanford-Crane, H., Oon, C., Xiao, X., Betts, C. B., Sun, D., ... & Sherman, M. H. (2022). A cancer cell–intrinsic GOT2–PPARδ axis suppresses antitumor immunity. *Cancer discovery*, *12*(10), 2414-2433.

60. Owens, D. K., Davidson, K. W., Krist, A. H., Barry, M. J., Cabana, M., Caughey, A. B., ... & US Preventive Services Task Force. (2019). Screening for pancreatic cancer: US preventive services task force reaffirmation recommendation statement. *Jama*, *322*(5), 438-444.

61. Canto, M. I., Harinck, F., Hruban, R. H., Offerhaus, G. J., Poley, J. W., Kamel, I., ... & Bruno, M. (2013). International Cancer of the Pancreas Screening (CAPS) Consortium summit on the management of patients with increased risk for familial pancreatic cancer. *Gut*, *62*(3), 339-347.

62. Goggins, M., Overbeek, K. A., Brand, R., Syngal, S., Del Chiaro, M., Bartsch, D. K., ... & Bruno, M. (2020). Management of patients with increased risk for familial pancreatic cancer: updated recommendations from the International Cancer of the Pancreas Screening (CAPS) Consortium. *Gut*, *69*(1), 7-17.

63. Aslanian, H. R., Lee, J. H., & Canto, M. I. (2020). AGA clinical practice update on pancreas cancer screening in high-risk individuals: expert review. *Gastroenterology*, *159*(1), 358-362.

64. Elbanna, K. Y., Jang, H. J., & Kim, T. K. (2020). Imaging diagnosis and staging of pancreatic ductal adenocarcinoma: a comprehensive review. *Insights into imaging*, *11*(1), 58.

65. Tummala, P., Junaidi, O., & Agarwal, B. (2011). Imaging of pancreatic cancer: An overview. *Journal of gastrointestinal oncology*, *2*(3), 168.

66. Mizuide, M., Ryozawa, S., Fujita, A., Ogawa, T., Katsuda, H., Suzuki, M., ... & Tanisaka, Y. (2020). Complications of endoscopic ultrasound-guided fine needle aspiration: a narrative review. *Diagnostics*, *10*(11), 964.

67. Șolea, S. F., Brisc, M. C., Orășeanu, A., Venter, F. C., Brisc, C. M., Șolea, R. M., ... & Brisc, C. (2024). Revolutionizing the pancreatic tumor diagnosis: emerging trends in imaging technologies: a systematic review. *Medicina*, *60*(5), 695.

68. Baek, S. K., Atousa Jahanshahi, M. D., Hanieh Akbari, M. D., Bal Subedi, M. D., & Neagu, S. embrACE the PAiN-CREATITIS: a case of benazepril induced pancreatitis.

69. Bilreiro, C., Andrade, L., Santiago, I., Marques, R. M., & Matos, C. (2024). Imaging of pancreatic ductal adenocarcinoma–An update for all stages of patient management. *European Journal of Radiology Open*, *12*, 100553.

70. Bi, Y., Li, D., Pang, R., Du, C., Li, D., Zhao, X., & Lv, H. (2025). Diagnosis methods for pancreatic cancer with the technique of deep learning: a review and a meta-analysis. *Frontiers in Oncology*, *15*, 1597969.

71. Zhang, L., Sanagapalli, S., & Stoita, A. (2018). Challenges in diagnosis of pancreatic cancer. *World journal of gastroenterology*, *24*(19), 2047.

72. Lee, E. S., & Lee, J. M. (2014). Imaging diagnosis of pancreatic cancer: a state-of-the-art review. *World journal of gastroenterology: WJG*, *20*(24), 7864.

73. Yang, D. H., Park, S. H., & Yoon, S. (2024). Differential diagnosis of pancreatic cancer and its mimicking lesions. *Journal of the Korean Society of Radiology*, *85*(5), 902.

74. Pu, Y., Wang, C., Zhao, S., Xie, R., Zhao, L., Li, K., ... & Sun, H. (2021). The clinical application of 18F-FDG PET/CT in pancreatic cancer: a narrative review. *Translational cancer research*, *10*(7), 3560.

75. Banks, T., & Tafti, D. (2024). Nuclear Medicine CNS Assessment, Protocols, and Interpretation. In *StatPearls [Internet]*. StatPearls Publishing.

76. Wang, X. Y., Yang, F., Jin, C., & Fu, D. L. (2014). Utility of PET/CT in diagnosis, staging, assessment of resectability and metabolic response of pancreatic cancer. *World Journal of Gastroenterology: WJG*, *20*(42), 15580.

77. Dibble, E. H., Karantanis, D., Mercier, G., Peller, P. J., Kachnic, L. A., & Subramaniam, R. M. (2012). PET/CT of cancer patients: part 1, pancreatic neoplasms. *American journal of roentgenology*, *199*(5), 952-967.

78. McKay, S. C., Thorne, T. W., Pathak, S., Wilkin, R. J., Barrie, J., Moir, J., ... & Surg-Panc-UK Study Group. (2025). The impact of FDG-PET/CT on the diagnostic pathway of surgically treated pancreatic ductal adenocarcinoma: the Surg-Panc-UK study. *HPB*.

79. Al Ansari, N., Ramalho, M., Semelka, R. C., Buonocore, V., Gigli, S., & Maccioni, F. (2015). Role of magnetic resonance imaging in the detection and characterization of solid pancreatic nodules: an update. *World Journal of Radiology*, *7*(11), 361.

80. Bugazia, D., Al-Najjar, E., Esmail, A., Abdelrahim, S., Abboud, K., Abdelrahim, A., ... & Abdelrahim, M. (2024). Pancreatic ductal adenocarcinoma: the latest on diagnosis, molecular profiling, and systemic treatments. *Frontiers in Oncology*, *14*, 1386699.

81. Berger, A. (2002). How does it work? Magnetic resonance imaging.(Clinical review). *British medical journal*, *324*(7328), 35-36.

82. Bogdanov Jr, A., & Mazzanti, M. L. (2011, February). Molecular magnetic resonance contrast agents for the detection of cancer: past and present. In *Seminars in oncology* (Vol. 38, No. 1, pp. 42-54). WB Saunders.

83. Khan, H. U., & FA, A. A. A. Y. (2024). Magnetic Resonance Cholangiopancreatography (MRCP): Innovations in Non-Invasive Visualization of the Hepatobiliary and Pancreatic Systems. *J Gastro Hepato*, *10*(12), 1-13.

84. Fung, A., Zaheer, A., Porter, K. K., Bashir, M. R., Cash, B. D., Chiorean, E. G., ... & Kim, D. H. (2025). ACR Appropriateness Criteria® Screening, Locoregional Assessment, and Surveillance of Pancreatic Ductal Adenocarcinoma: 2025 Update. *Journal of the American College of Radiology*, *22*(11), S610-S624.

85. Lee, J. S., & Kim, D. H. (2025). Patient-Friendly Summary of the ACR Appropriateness Criteria®: Screening, Locoregional Assessment, and Surveillance of Pancreatic Ductal Adenocarcinoma. *Journal of the American College of Radiology*.

86. Choi, M. H., Yoon, S. B., Lee, Y. J., Jung, E. S., Pak, S., Han, D., & Nickel, D. (2024). Rim enhancement of pancreatic ductal adenocarcinoma: investigating the relationship with DCE-MRI-based radiomics and next-generation sequencing. *Frontiers in Oncology*, *14*, 1304187.

87. Grewal, M., Ahmed, T., & Javed, A. A. (2023). Current state of radiomics in hepatobiliary and pancreatic malignancies. *Artificial Intelligence Surgery*, *3*(4), 217-232.

88. Xu, X., Qu, J., Zhang, Y., Qian, X., Chen, T., & Liu, Y. (2023). Development and validation of an MRI-radiomics nomogram for the prognosis of pancreatic ductal adenocarcinoma. *Frontiers in Oncology*, *13*, 1074445.

89. Zhao, B., Cao, B., Xia, T., Zhu, L., Yu, Y., Lu, C., ... & Ju, S. (2025). Multiparametric MRI for Assessment of the Biological Invasiveness and Prognosis of Pancreatic Ductal Adenocarcinoma in the Era of Artificial Intelligence. *Journal of Magnetic Resonance Imaging*.

90. Boekestijn, B., Feshtali, S., Meijer, A. C., Ibrahim, I. S., Farina-Sarasqueta, A., Inderson, A., ... & Wasser, M. N. (2020). MRI screening in hereditary pancreatic cancer: value of various sequences in the detection of early pancreatic cancer. *Annals of Pancreatic Cancer*, *3*.

91. Malagi, A. V., Shivaji, S., Kandasamy, D., Sharma, R., Garg, P., Gupta, S. D., ... & Mehndiratta, A. (2023). Pancreatic mass characterization using IVIM-DKI MRI and machine learning-based multi-parametric texture analysis. *Bioengineering*, *10*(1), 83.

92. Li, K., Li, J., Liu, X., Chen, J., & Chen, W. (2025). Multi-parametric MRI diffusion models combined with clinical information for predicting Ki-67 expression in pancreatic ductal adenocarcinoma: a prospective cohort study. *Abdominal Radiology*, 1-12.

93. Gao, Q. Y., Wang, L. J., & Ma, C. (2025). Diffusion-weighted magnetic resonance imaging of the pancreas: A narrative review. *World Journal of Radiology*, *17*(10), 112271.

94. Huang, J., Yang, S., Zou, L., Chen, Y., Yang, L., Yao, B., ... & Zhang, N. (2024). Quantitative pharmacokinetic parameter ktrans map assists in regional segmentation of nasopharyngeal carcinoma in dynamic contrast-enhanced magnetic resonance imaging (DCE-MRI). *Biomedical Signal Processing and Control*, *87*, 105433.

95. Noda, Y., Kawai, N., Kaga, T., Ishihara, T., Hyodo, F., Kato, H., ... & Matsuo, M. (2022). Vascular involvement and resectability of pancreatic ductal adenocarcinoma on contrast-enhanced MRI: comparison with pancreatic protocol CT. *Abdominal Radiology*, *47*(8), 2835-2844.

96. Liu, D., Chen, J., Zhang, Y., Dai, Y., & Yao, X. (2023). Magnetic resonance elastography-derived stiffness: potential imaging biomarker for differentiation of benign and malignant pancreatic masses. *Abdominal Radiology*, *48*(8), 2604-2614.

97. Preuss, K., Thach, N., Liang, X., Baine, M., Chen, J., Zhang, C., ... & Zheng, D. (2022). Using quantitative imaging for personalized medicine in pancreatic cancer: a review of radiomics and deep learning applications. *Cancers*, *14*(7), 1654.

98. High, R. A., Randtke, E. A., Jones, K. M., Lindeman, L. R., Ma, J. C., Zhang, S., ... & Pagel, M. D. (2019). Extracellular acidosis differentiates pancreatitis and pancreatic cancer in mouse models using acidoCEST MRI. *Neoplasia*, *21*(11), 1085-1090.

99. Gulani, V., Calamante, F., Shellock, F. G., Kanal, E., & Reeder, S. B. (2017). Gadolinium deposition in the brain: summary of evidence and recommendations. *The Lancet Neurology*, *16*(7), 564-570.

100. Strickler, S. E., & Clark, K. R. (2021). Gadolinium Deposition: A Study Review. *Radiologic technology*, *92*(3).

101. Choi, J. W., & Moon, W. J. (2019). Gadolinium deposition in the brain: current updates. *Korean journal of radiology*, *20*(1), 134-147.

102. Huang, C., Hecht, E. M., Soloff, E. V., Tiwari, H. A., Bhosale, P. R., Dasayam, A., ... & Goenka, A. H. (2024). Imaging for early detection of pancreatic ductal adenocarcinoma: Updates and challenges in the implementation of screening and surveillance programs. *American Journal of Roentgenology*, *223*(2), e2431151.

103. Zhang, L., Sanagapalli, S., & Stoita, A. (2018). Challenges in diagnosis of pancreatic cancer. *World journal of gastroenterology*, *24*(19), 2047.

104. Psar, R., Urban, O., Cerna, M., Rohan, T., & Hill, M. (2021). Improvement of the diagnosis of isoattenuating pancreatic carcinomas by defining their characteristics on contrast enhanced computed tomography and endosonography with fine-needle aspiration (EUS-FNA). *Diagnostics*, *11*(5), 776.

105. Blouhos, K., Boulas, K. A., Tsalis, K., & Hatzigeorgiadis, A. (2015). The isoattenuating pancreatic adenocarcinoma: Review of the literature and critical analysis. *Surgical Oncology*, *24*(4), 322-328.

106. Kim, J. H., Park, S. H., Yu, E. S., Kim, M. H., Kim, J., Byun, J. H., ... & Lee, M. G. (2010). Visually isoattenuating pancreatic adenocarcinoma at dynamic-enhanced CT: frequency, clinical and pathologic characteristics, and diagnosis at imaging examinations. *Radiology*, *257*(1), 87-96.

107. Singhi, A. D., Koay, E. J., Chari, S. T., & Maitra, A. (2019). Early detection of pancreatic cancer: opportunities and challenges. *Gastroenterology*, *156*(7), 2024-2040.

108. Takeda, Y., Saiura, A., Takahashi, Y., Inoue, Y., Ishizawa, T., Mise, Y., ... & Ito, H. (2017). Asymptomatic pancreatic cancer: does incidental detection impact long-term outcomes?. *Journal of Gastrointestinal Surgery*, *21*(8), 1287-1295.

109. Coradduzza, D., Perra, T., Sibono, L., Sanna, A., Cossu, M., Azara, E. G., ... & Medici, S. (2025). Diagnostic Stratification of Pancreatic Ductal Adenocarcinoma via Metallomics and Blood-Based Biomarkers. *Diagnostics*, *15*(21), 2818.

110. Tonini, V., & Zanni, M. (2025). Pancreatic cancer in 2025: Have we found a solution?. *World Journal of Gastroenterology*, *31*(43), 111433.

111. Haab, B., Qian, L., Staal, B., Jain, M., Fahrmann, J., Worthington, C., ... & Brand, R. E. (2024). A rigorous multi-laboratory study of known PDAC biomarkers identifies increased sensitivity and specificity over CA19-9 alone. *Cancer letters*, *604*, 217245.

112. Elsherif, S. B., Virarkar, M., Javadi, S., Ibarra-Rovira, J. J., Tamm, E. P., & Bhosale, P. R. (2020). Pancreatitis and PDAC: association and differentiation. *Abdominal Radiology*, *45*(5), 1324-1337.

113. Ren, S., Chen, X., Cui, W., Chen, R., Guo, K., Zhang, H., ... & Wang, Z. (2019). Differentiation of chronic mass-forming pancreatitis from pancreatic ductal adenocarcinoma using contrast-enhanced computed tomography. *Cancer Management and Research*, 7857-7866.

114. Mohamed, F., Vijayan, B., & Saraswat, L. (2024). IgG4-Related Autoimmune Pancreatitis Mimicking Pancreatic Cancer: A Report of Two Cases. *Cureus*, *16*(7).

115. Hsu, W. L., Chang, S. M., Wu, P. Y., & Chang, C. C. (2018). Localized autoimmune pancreatitis mimicking pancreatic cancer: Case report and literature review. *Journal of International Medical Research*, *46*(4), 1657-1665.

116. D'Onofrio, M., Ciaravino, V., Cardobi, N., De Robertis, R., Martini, P. T., Girelli, R., ... & Bassi, C. (2017). The borderline resectable/locally advanced pancreatic ductal adenocarcinoma staging with computed tomography/magnetic resonance imaging. *Endoscopic Ultrasound*, *6*(Suppl 3), S79-S82.

117. Nappo, G., Donisi, G., & Zerbi, A. (2021). Borderline resectable pancreatic cancer: Certainties and controversies. *World Journal of Gastrointestinal Surgery*, *13*(6), 516.

118. Andreucci, M., Faga, T., Serra, R., De Sarro, G., & Michael, A. (2017). Update on the renal toxicity of iodinated contrast drugs used in clinical medicine. *Drug, healthcare and patient safety*, 25-37.

119. Cunningham, A., Kirk, M., Hong, E., Yang, J., Howard, T., Brearley, A., ... & Wagner, B. (2024). The safety of magnetic resonance imaging contrast agents. *Frontiers in Toxicology*, *6*, 1376587.

120. Najjar, R. (2024). Clinical applications, safety profiles, and future developments of contrast agents in modern radiology: A comprehensive review. *Iradiology*, *2*(5), 430-468.

121. Ahmed, F. (2014). Endoscopic ultrasonography: challenges and opportunities in the developing world. *World Journal of Gastrointestinal Pharmacology and Therapeutics*, *5*(2), 55.

122. Fusaroli, P., Rakichevikj, E., & Lisotti, A. (2025). Quality in EUS: for many but not for all. *Best Practice & Research Clinical Gastroenterology*, 102010.

123. Wang, Y., Liu, K., Xie, X., & Song, B. (2021). Potential role of imaging for assessing acute pancreatitis-induced acute kidney injury. *The British Journal of Radiology*, *94*(1118), 20200802.

124. Lin, Z., Adeniran, E. A., Cai, Y., Qureshi, T. A., Li, D., Gong, J., ... & Jiang, Y. (2025). Early Detection of Pancreatic Cancer: Current Advances and Future Opportunities. *Biomedicines*, *13*(7), 1733.

125. Cao, K., Xia, Y., Yao, J., Han, X., Lambert, L., Zhang, T., ... & Lu, J. (2023). Large-scale pancreatic cancer detection via non-contrast CT and deep learning. *Nature medicine*, *29*(12), 3033-3043.

126. Xu, Y., Li, Y., Wang, F., Zhang, Y., & Huang, D. (2025). Addressing the current challenges in the clinical application of AI-based Radiomics for cancer imaging. *Frontiers in Medicine*, *12*, 1674397.

127. Lekkas, G., Vrochidou, E., & Papakostas, G. A. (2025). Advancements in radiomics-based AI for pancreatic ductal adenocarcinoma. *Bioengineering*, *12*(8), 849.

128. Virostko, J., Craddock, R. C., Williams, J. M., Triolo, T. M., Hilmes, M. A., Kang, H., ... & Powers, A. C. (2021). Development of a standardized MRI protocol for pancreas assessment in humans. *PloS one*, *16*(8), e0256029.

129. Lee, S., Xie, J., & Chen, X. (2010). Peptide-based probes for targeted molecular imaging. *Biochemistry*, *49*(7), 1364-1376.

130. Wang, Q., Yan, H., Jin, Y., Wang, Z., Huang, W., Qiu, J., ... & Tian, J. (2018). A novel plectin/integrin-targeted bispecific molecular probe for magnetic resonance/near-infrared imaging of pancreatic cancer. *Biomaterials*, *183*, 173-184.

131. Acier, A., Godard, M., Gassiot, F., Finetti, P., Rubis, M., Nowak, J., ... & Guillaumond, F. (2021). LDL receptor-peptide conjugate as in vivo tool for specific targeting of pancreatic ductal adenocarcinoma. *Communications Biology*, *4*(1), 987.

132. Bardol, T., Dujon, A. M., Taly, V., Dunyach-Remy, C., Lavigne, J. P., Costa-Silva, B., ... & Alix-Panabières, C. (2024). Early detection of pancreatic cancer by liquid biopsy “PANLIPSY”: a French nation-wide study project. *Bmc Cancer*, *24*(1), 709.

133. Wang, X., Wang, H., Zhang, M., Li, H., Liu, Y., Huang, H., ... & Hao, J. (2026). Development and Prospective Validation of a Cell-free DNA–Based Model for the Early Detection of Pancreatic Cancer. *Cancer Discovery*, *16*(1), 66-80.

134. Yin, L., Cao, C., Lin, J., Wang, Z., Peng, Y., Zhang, K., ... & Jiang, K. (2025). Development and Validation of a Cell-Free DNA Fragmentomics–Based Model for Early Detection of Pancreatic Cancer. *Journal of Clinical Oncology*, JCO-24.

135. Blackford, A. L., Canto, M. I., Dbouk, M., Hruban, R. H., Katona, B. W., Chak, A., ... & Goggins, M. (2024). Pancreatic cancer surveillance and survival of high-risk individuals. JAMA oncology, 10(8), 1087-1096.

136. Manam, A., Everett, J. N., Haraldsdottir, S., Hart, P. A., Kaul, V., Klute, K., ... & PRECEDE Consortium. (2025). Areas of Uncertainty in Pancreatic Cancer Surveillance: A Survey Across the International Pancreatic Cancer Early Detection (PRECEDE) Consortium. *JCO Precision Oncology*, *9*, e2500696.

137. Lin, Z., Adeniran, E. A., Cai, Y., Qureshi, T. A., Li, D., Gong, J., ... & Jiang, Y. (2025). Early Detection of Pancreatic Cancer: Current Advances and Future Opportunities. *Biomedicines*, *13*(7), 1733.

138. Santhanakrishnan, K. R., Koilpillai, J., Narayanasamy, D., & Santhanakrishnan, K. (2024). PEGylation in pharmaceutical development: current status and emerging trends in macromolecular and immunotherapeutic drugs. *Cureus*, *16*(8).

139. Caliceti, P., & Veronese, F. M. (2003). Pharmacokinetic and biodistribution properties of poly (ethylene glycol)–protein conjugates. *Advanced drug delivery reviews*, *55*(10), 1261-1277.

140. Kolate, A., Baradia, D., Patil, S., Vhora, I., Kore, G., & Misra, A. (2014). PEG—A versatile conjugating ligand for drugs and drug delivery systems. *Journal of controlled release*, *192*, 67-81.

141. Padín-González, E., Lancaster, P., Bottini, M., Gasco, P., Tran, L., Fadeel, B., ... & Monopoli, M. P. (2022). Understanding the role and impact of poly (ethylene glycol)(PEG) on nanoparticle formulation: Implications for COVID-19 vaccines. *Frontiers in bioengineering and biotechnology*, *10*, 882363.

142. Taher, M., Susanti, D., Haris, M. S., Rushdan, A. A., Widodo, R. T., Syukri, Y., & Khotib, J. (2023). PEGylated liposomes enhance the effect of cytotoxic drug: A review. *Heliyon*, *9*(3).

143. Gao, Y., Joshi, M., Zhao, Z., & Mitragotri, S. (2024). PEGylated therapeutics in the clinic. *Bioengineering & translational medicine*, *9*(1), e10600.

144. Turecek, P. L., Bossard, M. J., Schoetens, F., & Ivens, I. A. (2016). PEGylation of biopharmaceuticals: a review of chemistry and nonclinical safety information of approved drugs. *Journal of pharmaceutical sciences*, *105*(2), 460-475.

145. Kunkel, G. E., Zhou, Q., Treacy, J. W., Montgomery, H. R., Salas-Ambrosio, P., Ready, A. D., ... & Maynard, H. D. (2024). Comparison of cyclic and linear PEG conjugates. *Bioconjugate Chemistry*, *35*(6), 744-749.

146. Suk, J. S., Xu, Q., Kim, N., Hanes, J., & Ensign, L. M. (2016). PEGylation as a strategy for improving nanoparticle-based drug and gene delivery. *Advanced drug delivery reviews*, *99*, 28-51.

147. Chen, L., Zhang, Z., R. Simonsen, M., Owens, T., MH Khorooshi, R., & Wu, C. (2025). PEGylated liposomes via ATRP for brain drug delivery. *Journal of Liposome Research*, 1-7.

148. Chen, S. L., Fu, R. H., Liao, S. F., Liu, S. P., Lin, S. Z., & Wang, Y. C. (2018). A PEG-based hydrogel for effective wound care management. *Cell transplantation*, *27*(2), 275-284.

149. Sawadkar, P., Lali, F., Garcia-Gareta, E., Garrido, B. G., Chaudhry, A., Matharu, P., ... & Greco, K. (2025). Innovative hydrogels in cutaneous wound healing: current status and future perspectives. *Frontiers in Bioengineering and Biotechnology*, *13*, 1454903.

150. Isaac, A. H., Recalde Phillips, S. Y., Ruben, E., Estes, M., Rajavel, V., Baig, T., ... & Alge, D. L. (2024). Impact of PEG sensitization on the efficacy of PEG hydrogel-mediated tissue engineering. *Nature Communications*, *15*(1), 3283.

151. Carlin, A., & Justham, D. (2011). A literature review of two laxatives: lactulose and polyethylene glycol. *British journal of community nursing*, *16*(12), 584-590.

152. Picard, M., Drolet, J. P., Masse, M. S., Filion, C. A., ALMuhizi, F., Fein, M., ... & Primeau, M. N. (2022). Safety of COVID-19 vaccination in patients with polyethylene glycol allergy: a case series. *The Journal of Allergy and Clinical Immunology: In Practice*, *10*(2), 620-625.

153. Mima, Y., Hashimoto, Y., Shimizu, T., Kiwada, H., & Ishida, T. (2015). Anti-PEG IgM is a major contributor to the accelerated blood clearance of polyethylene glycol-conjugated protein. *Molecular pharmaceutics*, *12*(7), 2429-2435.

154. Miao, G., He, Y., Lai, K., Zhao, Y., He, P., Tan, G., & Wang, X. (2023). Accelerated blood clearance of PEGylated nanoparticles induced by PEG-based pharmaceutical excipients. *Journal of Controlled Release*, *363*, 12-26.

155. McSweeney, M. D., Price, L. S., Wessler, T., Ciociola, E. C., Herity, L. B., Piscitelli, J. A., ... & Lai, S. K. (2019). Overcoming anti-PEG antibody mediated accelerated blood clearance of PEGylated liposomes by pre-infusion with high molecular weight free PEG. *Journal of Controlled Release*, *311*, 138-146.

156. Zheng, Y., Zhou, Q., Ma, H., Xu, H., Xiao, D., Li, Y., ... & Li, Y. (2025). Slow intravenous infusion reduces the accelerated blood clearance of PEGylated liposomes by removing anti-PEG antibodies. *Journal of Controlled Release*, 113762.

157. Zhang, K., Li, M., Sui, D., Zhao, J., She, Z., Ding, K., ... & Deng, Y. (2025). Asymmetrical branched PEG-modified liposomes evade anti-PEG antibody recognition to abolish accelerated blood clearance and amplify tumor drug accumulation. *Nanoscale*, *17*(37), 21693-21705.

158. Ludwig, B. S., Kessler, H., Kossatz, S., & Reuning, U. (2021). RGD-binding integrins revisited: how recently discovered functions and novel synthetic ligands (re-) shape an ever-evolving field. *Cancers*, *13*(7), 1711.

159. Li, N., Qiu, S., Fang, Y., Wu, J., & Li, Q. (2021). Comparison of linear vs. cyclic RGD pentapeptide interactions with integrin αvβ3 by molecular dynamics simulations. *Biology*, *10*(7), 688.

160. Nieberler, M., Reuning, U., Reichart, F., Notni, J., Wester, H. J., Schwaiger, M., ... & Kessler, H. (2017). Exploring the role of RGD-recognizing integrins in cancer. *Cancers*, *9*(9), 116.

161. Kim, J., Hong, S. Y., Park, H. S., Kim, D. S., & Lee, W. (2005). Structure and function of RGD peptides derived from disintegrin proteins. *Molecules and cells*, *19*(2), 205-211.

162. Bogdanowich-Knipp, S. J., Chakrabarti, S., Siahaan, T. J., Williams, T. D., & Dillman, R. K. (1999). Solution stability of linear vs. cyclic RGD peptides. *The Journal of peptide research*, *53*(5), 530-541.

163. Chen, K., Xie, J., & Chen, X. (2009). RGD-human serum albumin conjugates as efficient tumor targeting probes. *Molecular imaging*, *8*(2), 7290-2009.

164. Kapp, T. G., Rechenmacher, F., Neubauer, S., Maltsev, O. V., Cavalcanti-Adam, E. A., Zarka, R., ... & Kessler, H. (2017). A comprehensive evaluation of the activity and selectivity profile of ligands for RGD-binding integrins. *Scientific reports*, *7*(1), 39805.

165. Yamada, Y., Onda, T., Wada, Y., Hamada, K., Kikkawa, Y., & Nomizu, M. (2023). Structure–Activity relationships of RGD-Containing peptides in integrin αvβ5-Mediated cell adhesion. *ACS omega*, *8*(5), 4687-4693.

166. Roy, A., Shi, L., Chang, A., Dong, X., Fernandez, A., Kraft, J. C., ... & Baker, D. (2023). De novo design of highly selective miniprotein inhibitors of integrins αvβ6 and αvβ8. *Nature Communications*, *14*(1), 5660.

167. Yeh, T. Y., Lin, J. H., Jiang, Y. J., Cho, E. C., & Lee, K. C. (2025). Exploration of RGD peptide-modified targeted delivery of doxorubicin using chitosan oligosaccharide-coated GQD carriers with different complexity. *International Journal of Biological Macromolecules*, *320*, 145734.

168. Cossu, J., Thoreau, F., & Boturyn, D. (2023). Multimeric RGD-based strategies for selective drug delivery to tumor tissues. *Pharmaceutics*, *15*(2), 525.

169. Sun, Y., Kang, C., Liu, F., Zhou, Y., Luo, L., & Qiao, H. (2017). RGD peptide-based target drug delivery of doxorubicin nanomedicine. *Drug development research*, *78*(6), 283-291.

170. D'Amore, V. M., Donati, G., Lenci, E., Ludwig, B. S., Kossatz, S., Baiula, M., ... & Marinelli, L. (2023). Molecular View on the i RGD Peptide Binding Mechanism: Implications for Integrin Activity and Selectivity Profiles. *Journal of Chemical Information and Modeling*, *63*(20), 6302-6315.

171. Thirumalai, A., Girigoswami, K., Pallavi, P., Harini, K., Gowtham, P., & Girigoswami, A. (2023). Cancer therapy with iRGD as a tumor-penetrating peptide. *Bulletin du Cancer*, *110*(12), 1288-1300.

172. Kang, S., Lee, S., & Park, S. (2020). iRGD peptide as a tumor-penetrating enhancer for tumor-targeted drug delivery. *Polymers*, *12*(9), 1906.

173. Wang, K., Zhang, X., Liu, Y., Liu, C., Jiang, B., & Jiang, Y. (2014). Tumor penetrability and anti-angiogenesis using iRGD-mediated delivery of doxorubicin-polymer conjugates. *Biomaterials*, *35*(30), 8735-8747.

1.12 Tables and Figures

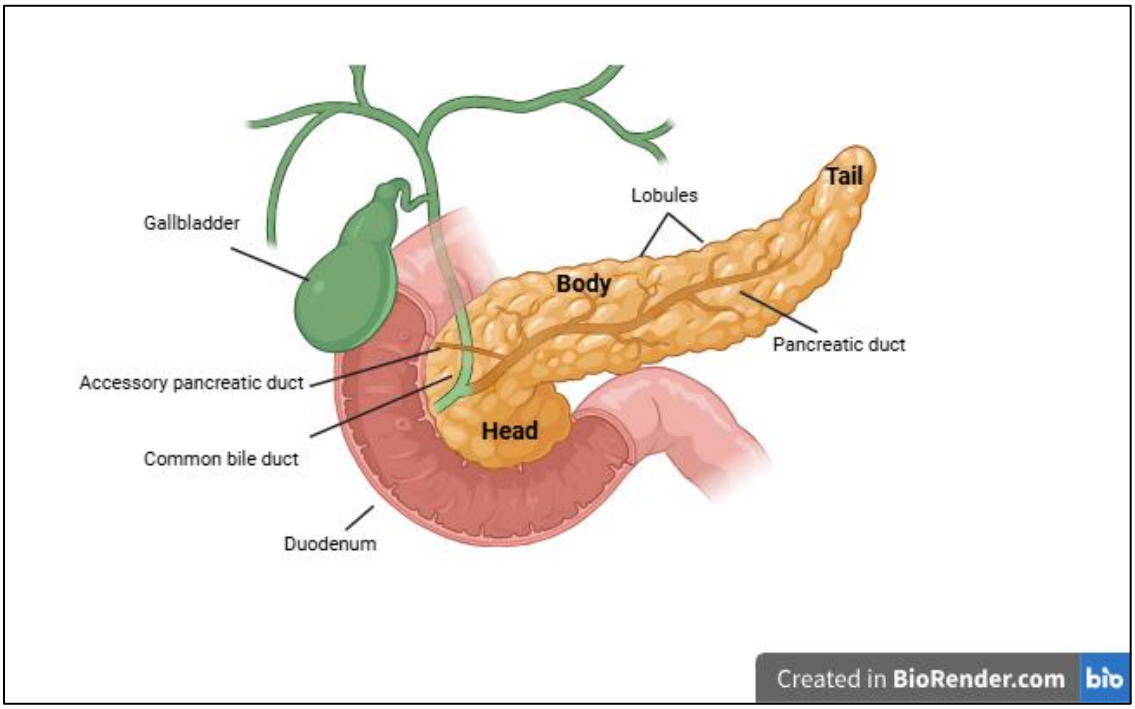


Figure 1-1 Diagram of basic pancreas anatomy and surrounding structures.

Disease	Mutated Gene	Relative Risk of PDAC
Peutz-Jeghers syndrome	*STK11/LKB1*	132
Hereditary pancreatitis	*PRSS1*	60-87
Familial atypical multiple mole melanoma syndrome	*CDKN2A/p16*	13-22
Hereditary nonpolyposis colorectal cancer	*hMSH2 and hMLH1*	8.6
Li-Fraumeni syndrome	*TP53*	7.3
Hereditary breast and ovarian cancer syndrome	*BRCA1/2 and PALB2*	4.1-5.8
Hereditary colorectal adenomatous polyposis	*APC*	4.4
Ataxia-telangiectasia mutation	*ATM*	3.9

Table 1-1 Hereditary pancreatic cancer syndrome.

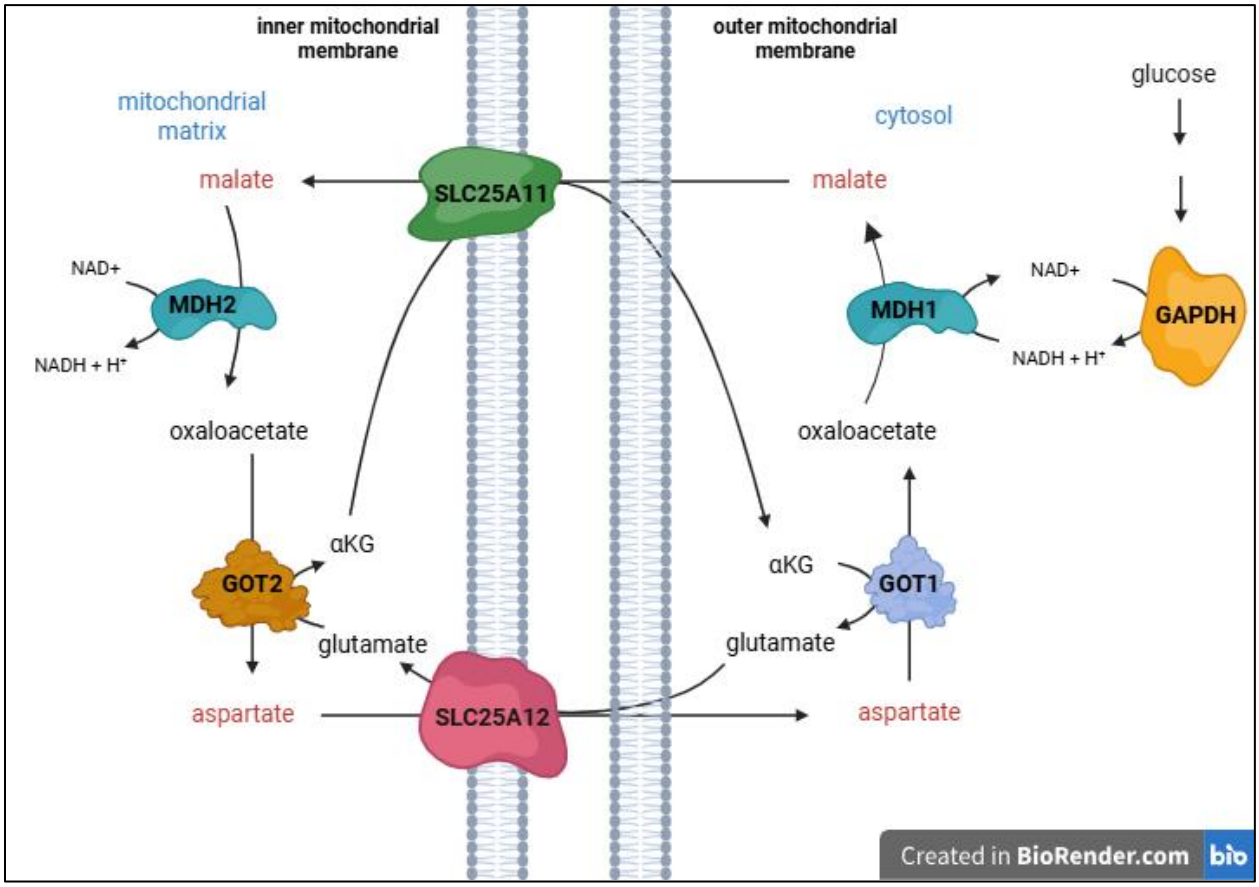


Figure 1-2 Malate-Aspartate Shuttle.

The shuttle is the principal mechanism for the movement of reducing equivalents (in the form of NADH) from the cytoplasm to the mitochondria. The glycolytic pathway is the source of cytoplasmic NADH. Cytoplasmic malate dehydrogenase (MDH1) reduces oxaloacetate to malate while oxidizing NADH to NAD+. Malate is then transported into the mitochondria via the SLC25A11 transporter. When malate enters the mitochondria, the reverse reaction is carried out by mitochondrial malate dehydrogenase (MDH2). Oxaloacetate is converted to aspartate by mitochondrial glutamic-oxaloacetic transaminase (GOT2) while simultaneously converting glutamate to α-ketoglutarate (αKG). The reverse reaction is performed by cytosolic glutamic-oxaloacetic transaminase (GOT1). Aspartate is transported across the mitochondrial membrane by SLC25A12.

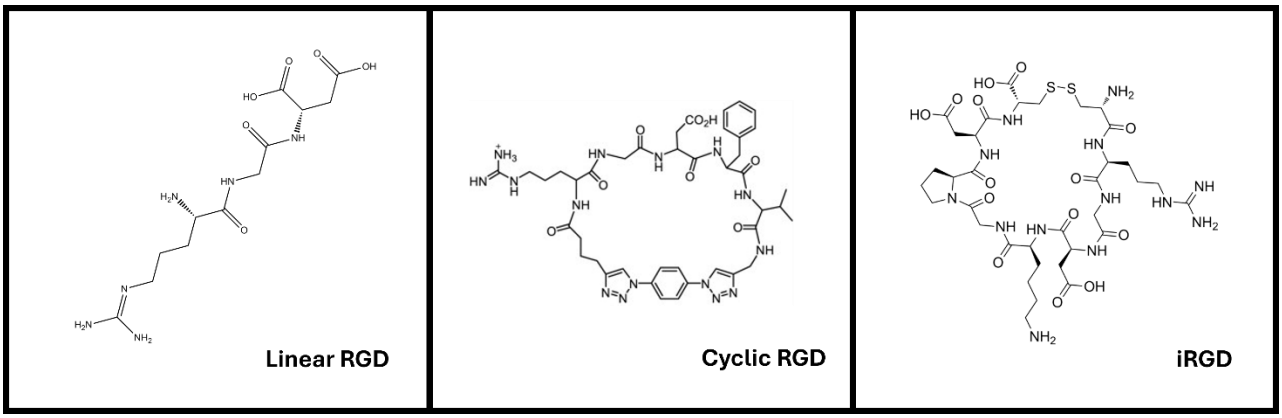


Figure 1-3 Arginine-Glycine-Aspartate (RGD) Structures.

One example of each family of RGD peptides is presented to demonstrate the structural differences between each category. The linear structure (left) is more easily synthesized and has flexibility when grafted onto polymers. The cyclic RGD (center) provides greater stability in vivo and offers higher integrin affinity. The iRGD (right) is a specialized cyclic RGD that maintains the favorable pharmacologic properties of the simple cyclic RGD while also offering augmented tumor penetration functionality.

Chapter 2: Aspartate Transaminases Are Dispensable for Pancreatic Development and Pancreatic Cancer Progression†

2.1 Abstract

Pancreatic ductal adenocarcinoma (PDAC) is the third leading cause of cancer-related deaths in the United States. This is due in part to the limited availability of effective treatment options for patients, highlighting a significant need for new targets and approaches. Deregulated metabolism is a hallmark feature of PDAC that has gained attention as a promising inroad for therapy. The aspartate transaminases (glutamate oxaloacetate transaminases, cytosolic GOT1 and mitochondrial GOT2) have several important metabolic functions, including maintaining energy and redox balance and generating aspartate, an essential building block in protein and nucleotide biosynthesis. Previous studies of GOT proteins in preclinical tumor transplant models have yielded conflicting results regarding the requirement of GOT1 and GOT2 for PDAC tumor growth. To assess the role of GOT proteins in tumor development and tumor

---

†This chapter consists of a published preprint article: Urgas J*, **Nelson NS***, Kerk SA, Sutton D, Lin L, Sajjakulnukit P, Dombrowski T, Davidson G, Lavoie B, Awad D, Olivei A, Yan W, Strayhorn C, Radyk M, Perricone M, Pasca di Magliano M, Bednar F, Frankel T, Shah YM, Lyssiotis CA. Aspartate transaminases are dispensable for pancreatic development and pancreatic cancer progression. *bioRxiv*. (2025): 2025-12.

*These authors contributed equally.

Author Details and Contributions: J.U., N.S.N., S.A.K. and C.A.L. designed the study. J.U. and C.A.L. wrote the manuscript. J.U. and N.S.N. collected data for the bulk of the experimental studies. J.U. prepared the manuscript figures. S.A.K., D.S., T.D., G.D., M.P., M.R., D.A., A.O., L.L., P.S., W.Y., and C.S. conducted experiments. A.O., P.S., and W.Y. contributed to data analysis. C.A.L., Y.S., F.B., T.F., and M.P.M. provided resources funding, and conceptual input for experiments and supervised the research. All authors reviewed and approved the manuscript.

maintenance, we generated conditional knockout mice for *Got1* and *Got2* and crossed these into pancreas-specific models. Whereas loss of either *Got* does not impact pancreas development, double *Got1* and *Got2* knockout results in markedly reduced pancreas size and cellularity without overtly impacting endocrine or exocrine function. In genetically engineered cancer models, single *Got* loss does not impact lesion formation, tumor size, animal survival, or the composition of the tumor microenvironment. Identical results were also observed in orthotopic allograft mouse models. Together, these findings add to a growing body of work illustrating the adaptability of metabolism in cancer. They also emphasize the importance of model selection, the use of multiple independent models, and the *in vivo* context when studying the role of metabolic programs in cancer.

2.2 Introduction

Pancreatic ductal adenocarcinoma (PDAC), the most common form of pancreatic cancer, is projected to be the second leading cause of cancer-related deaths in the United States by 2030. (1) Over half of PDAC patients are diagnosed at a late stage of disease when surgery is not possible, and our treatment approaches are largely ineffective. The 5-year survival rate for patients with late-stage disease is only 3%, contrasting the more favorable 5-year survival rate of 44% for those diagnosed when the disease is confined to the pancreas. (1-3) Thus, there is a clear and pressing need to both better detect and intercept in the early stages of disease and develop better treatments for advanced disease.

PDAC tumors are noted for their complex cellular environment, which includes a dense stromal reaction that leads to deregulated vasculature, nutrient access, and drug infiltration. (4-6) In this abnormal tumor microenvironment (TME), PDAC cells engage in extensive metabolic rewiring to promote their fitness and survival. (7) Many of these mechanisms are driven by oncogenic KRAS (8-11), which is the signature transforming oncogene in PDAC. (12-14) In earlier studies, we found that mutant Kras drives altered glutamine metabolism to support redox balance PDAC growth. (15) This phenotype is mediated in part through the rewiring of central carbon metabolism via the glutamate-oxaloacetate transaminases (GOT), cytosolic GOT1 and mitochondrial GOT2.

The GOTs serve many functions in cellular metabolism (Figure 1A). They catalyze the reversible, substrate-driven transamination of glutamate and oxaloacetate into aspartate and α-ketoglutarate. Classically, the GOTs are most well known for their role in the malate-aspartate shuttle (MAS), an evolutionarily conserved metabolic pathway that maintains redox and energy balance between the cytosol and the mitochondria. The MAS links cytosolic and mitochondrial energy production through a series of redox reactions that allow NADH to enter mitochondria and support mitochondrial ATP production. In its anabolic role, GOT2 generates aspartate, driven both by facilitated release from the mitochondria and net consumption. GOT1/2 are the only cellular source of aspartate, which is essential for the production of nucleotides and asparagine. (15-18) GOT1 and GOT2 also generate α-ketoglutarate, which can support mitochondrial TCA cycle metabolism and the epigenetic regulation of gene expression.

Given their regulation by KRAS and their central functions in cell growth and proliferation, GOT1 and GOT2 have been extensively studied in PDAC. For example, we first described how PDAC cells route glutamine carbon through a GOT2-GOT1 pathway to maintain redox homeostasis. (15) In this and a subsequent study, we demonstrated that genetic inhibition of GOT1 in PDAC cells reduces proliferation and colony formation *in vitro*, sensitizes cells to ferroptosis, and slows the rate of tumor growth in human subcutaneous xenograft models. (15, 19) Work from our group on GOT2 revealed that genetic inhibition or knockout of GOT2 reduces proliferation and colony formation *in vitro*, a consequence of elevated NADH reductive stress. However, GOT2 knockout did not slow the rate of tumor growth in subcutaneous and orthotopic human xenograft models. (17) Mechanistically, it was demonstrated that GOT knockout tumors can scavenge aspartate via macropinocytosis to enable tumor growth. (20)

These studies revealed important distinctions between the dependence on GOT metabolism *in vitro* vs *in vivo*. However, transplant models are unable to provide information about the consequences of GOT inhibition in the context of an evolving tumor in the pancreas. To address these shortcomings, we developed a conditional knockout of *Got2* and crossed this into genetically engineered models of pancreatic tumor initiation. We found that *Got2* pancreas-specific knockout did not protect from precancerous lesion formation. (17) A related study using immune competent transplant models illustrated that knockout of *Got2* marked slowed tumor growth in a T cell-dependent manner. (21) It is important to note that these collective studies utilized diverse cell lines and animal models, which may account for the conflicting findings.

More importantly, together, these studies highlight that the field lacks a clear consensus on the role of GOT dependence in PDAC.

In this study, we revisit the role of Got1 and Got2 in pancreatic cancer using a battery of state-of-the-art models. Here, we find that the combined loss of Got1 and Got2 leads to reduced pancreas size without overtly impacting function or mouse health. Using these new genetically engineered mouse models, we then demonstrate that loss of either Got1 or Got2 does not impact tumor initiation, growth, or the immune compartment of the TME.

2.3 Methods

Got CRISPR/Cas9 knockout: The lentiviral vector for CRISPR knockout (KO), lentiCRISPR v2, was obtained from Addgene (plasmid #52961)[33]. Plasmid DNA was expanded by transformation of NEB Stable competent cells (NEB, C3040H) and maxi prepped using the EndoFree Plasmid Maxi Kit (Qiagen, 12362). The cloning vector was prepared by *BsmB*I-v2 (NEB, R0739S) digestion and the ends of linearized vector dephosphorylation executed with Shrimp Alkaline Phosphatase (rSAP) (NEB, M0371S) followed by 1% of agarose gel (Invitrogen, 16500500) purification (Qiagen, 28704). Several guide RNAs from the various mouse CRISPR libraries were selected and screened (https://www.addgene.org/pooled-library/#crispr). Previously published cloning procedures were followed[33,34]. The workflow for generating *Got1* and *Got2* knockout cell lines are detailed here. 1) Sense and antisense guide RNA oligos were synthesized (IDT-Integrated DNA Technologies), phosphorylated (NEB, M0201S), and annealed (ABI Thermal Cycler). The prepped vector and annealed guide RNAs were ligated

(NEB, M0202S); 2) 293FT cells were used for transfection; 3) 7940B and MT3 murine pancreatic cancer cell lines were transduced with virus and selected with puromycin for 5 days (Sigma, P8833, 3μg/mL). The best KO guide RNA constructs were selected after Western Blotting and qRT-PR and utilized for *in vitro* and *in vivo* studies. Sequences of mouse guide RNAs for mouse Got1 (NM_010324) and Got2 (NM_010325) are shown here.

(**Table 2-1**)

Western Blotting: For cells in culture, medium was aspirated, and the wells were washed once with PBS. Thereafter, 50-100 μl of radioimmunoprecipitation assay buffer (Sigma-Aldrich, R0278) to which phosphatase and protease inhibitors were added, was transferred to each well to lyse the cells. Lysis and the collection of the lysates were completed on ice. Following a 5- to 10-minute incubation on ice, lysates were collected into 1.5 ml Eppendorf tubes and centrifuged at 4 °C for 10 min at 18,000*g* to extract the sample supernatant. Protein concentration of the samples for western blot analysis was measured using Pierce BCA Protein Assay Kit (ThermoFisher, 23227) according to the manufacturer's instructions. For the running step, samples were loaded at 20 μg protein per lane along with the SeeBlue Plus2 protein ladder (Invitrogen, LC5925) and run at 120V on an Invitrogen NuPAGE 4–12% Bis-Tris gel for 1 hour (ThermoFisher, NP0336BOX). Thereafter, the separated proteins were transferred to methanol-activated PVDF membranes (Millipore) at 25 V for 1 h. Following this, membranes were immersed in blocking buffer (5% blotting-grade blocker (Bio-Rad, 1706404) in TBS-T solution: tris-buffered saline (Bio-Rad, 1706435) with 0.1% Tween-20 (Sigma-Aldrich, 9005-64-5) for ~1 h on a plate rocker at room temperature. Next, membranes were

washed 3 times with TBS-T at 10 min per wash, immersed in the indicated primary antibodies, and incubated overnight at 4 °C on a plate rocker. The antibodies used were diluted in blocking buffer at dilutions recommended by the manufacturer. The following day, the primary antibody was removed, and the membrane was washed 3 times with TBS-T and on a plate rocker for 5 min per wash. Immediately after, the membrane was incubated for 1 h with gentle rocking at room temperature in the appropriate secondary antibody diluted 1:10,000 in TBS-T. Lastly, the membrane was washed 3 times in TBS-T at 10 min per wash and incubated in chemiluminescence reagent (Clarity Max Western ECL Substrate, 705062) according to the manufacturer's instructions. Subsequently, blot images were acquired on a Bio-Rad ChemiDoc Imaging System (Image Lab Touch Software version 2.4.0.03). The following primary antibodies were used in this study at a 1:1,000 dilution: GOT1 Abcam 239487, GOT2 Sigma-HPA018139, and Vinculin CST (E1E9V) XP Rabbit mAb #13901. For secondary antibodies, Cell Signaling Anti-rabbit HRP-linked antibody (7074) and Anti-mouse HRP-linked antibody (7076) were used at a 1:10,000 dilution.

Cell viability assay: Cells were seeded in replicates of 5 or 10 at 500 cells per well and 1000 cells per well in standard growth medium for 24 hours in a white-bottom 96-well plate. The next day, in dark conditions, Cell Titer Glo Reagent (CAT G9242) was diluted 1:3 in PBS and added in a 1:1 volume to the media in each well. Plates were covered from light, shaken for 2 minutes, then incubated at room temperature for 10 minutes to stabilize the signal. Luminescence was promptly recorded on a plate reader.

Cell proliferation assay: Cells were seeded in replicates of 5 or 10 at 500 cells per well and 1000 cells per well in standard growth medium for 24 hours in a clear-bottom 96-

well plate. Cells were then placed on a Biotek Biospa 8 Automated Incubator for continuous incubation and cell counting over 48-72 hours. Cell counts were taken every 24 hours for each well.

Oxygen consumption rate: Cells were seeded in replicates of 7 at 500 cells per well in standard growth medium for 24 hours in a Falcon clear-bottom 96-well plate. The next day, a Lucid Scientific Resipher was placed on each plate in a sterile incubator for 72 hours to measure oxygen consumption rate and environmental conditions, including humidity. Data was analyzed from the Lucid Lab online tool. Oxygen consumption rate was normalized to cell count for each line, followed by normalization to the corresponding non-targeting sample.

Metabolomics Sample Preparation: For *in vitro* extracellular (medium) and intracellular metabolomic profiling, PDAC cells were seeded in triplicate in a 6-well plate at 150,000 cells per well in growth medium. The cells were incubated for 48 hours. Thereafter, for extracellular metabolites, 200 µl of medium was collected from each well into a 1.5 ml Eppendorf tube, spun to remove cell debris, and to that 800 µl ice-cold 80% methanol was added. For intracellular metabolites, the remaining medium was aspirated, and 1 ml of ice-cold 80% methanol was added to each well on dry ice for 10 min. Each well was scraped and spun down to clarify samples. Thereafter, cell lysates were collected from each well and transferred into separate 1.5 ml Eppendorf tubes. The samples were then centrifuged at 12,000*g*. For each experimental condition, the volume of supernatant to collect for drying with the SpeedVac Vacuum Concentrator (model: SPD1030) was determined based on the protein concentration of the parallel plate.

For pancreas tissue, samples were flash frozen in liquid nitrogen upon collection. Tissue samples of approximately equal weight (~0.02 g) were collected per sample per experimental group. The tissues were then put into 2 ml Eppendorf tubes with 1 ml of ice-cold 80% methanol (diluted in 20% H_2O). Metallic beads were added to each tube, and samples were shaken and homogenized on a Retsch TissueLyser II (129251128) in intervals of 30 s until fully homogenized. Samples were then centrifuged at 12,000*g,* and the supernatant was collected for further processing.

Metabolomics method and analysis: Targeted metabolomics was performed on an Agilent 1290 Infinity II Binary Bio LC coupled with an Agilent 6495d QqQ mass spectrometer. Two methods were utilized in this study on the same instrumentation. For the first method, an Agilent InfinityLab Poroshell 120 HILIC-Z, 2.1 x 150 mm, 2.7uM (p/n 683775-924) was used. Method parameters are as follows: Solvent A is water + 20mM ammonium acetate (pH 9.3) + 5uM medronic acid. Solvent B is acetonitrile. Wash solvent is 1:1:1 water, acetonitrile, and methanol. The solvent gradient is 10% A – 90% B until 1 minute, 22% A – 78% B until 8 minutes, 40% A – 60% B until 12 minutes, 90% A – 10% B until 15 minutes, hold until 18 minutes, 10% A – 90% B until 19 minutes, hold until 23 minutes. Flow rate was 0.4mL/minutes. Column temperature was set to 15 C. Source parameters were optimized for the Agilent dMRM (dynamic multiple reaction monitoring) library. The dMRM library was acquired from Agilent for their HILIC-Z platform and further optimized to screen for 435 targets in both positive and negative ion modes.

Method 2 utilized an Agilent ZORBAX RRHD Eclipse Plus C18, 100 x 2.1mm, 1.8um (p/n, 959758-902) column. Solvent A was water + 0.1% formic acid. Solvent B is

methanol + 0.1% formic acid. Wash solvent is 1:1 water and methanol. The solvent gradient is100% A until 3 minutes, 5% A – 95% B until 5 minutes, hold until 7 minutes, 100% A until 8 minutes, hold until 10 minutes. Flow rate is 0.2mL/minutes. Column temperature is set to 45 C. Source parameters reflect method 1. The dMRM acquisition list includes 12 targets optimized by analytical standards in both positive and negative ion modes.

Data from both methods was preprocessed using Agilent MassHunter Workstation Quantitative Analysis for QQQ Version 12.1.

Raw data was normalized by median-centering and then further fold-change analysis was performed relative to control groups to achieve a relative abundance. Student's T-Tests were performed with an alpha level of 0.1. Heatmaps were generated in Morpheus (Morpheus, https://software.broadinstitute.org/morpheus).

Mouse studies: Animal studies were performed at the University of Michigan under the supervision of Unit for Laboratory Animal Medicine and in accordance with the Institutional Animal Care and Use Committee (IACUC). All animals used in this study were housed in a pathogen-free environment, and all procedures involving these animals were performed in accordance with the requirements of the University of Michigan Institutional Animal Care & Use Committee (IACUC). Mice were housed at a maximum of five mice per cage in a pathogen-free animal facility with a 12 h:12 h light: dark cycle, with 30–70% humidity and a temperature of 20–23 °C.

Genetically engineered mouse models: *Ptf1a-Cre, Ptf1a-Cre;*LSL-*Kras*$^{G12D/+}$ and *Ptf1a-Cre;*LSL-*Kras*$^{G12D/+}$;*Trp53*$^{R172H/+}$ mice have been described previously. (12) Floxed

Got1$^{f/f}$ and *Got2*$^{f/f}$ mice were generated by Ozgene (*Got1* floxed around exon 3; *Got2* floxed around exon 2)[17,35]. PCR genotyping was done for the *Ptf1a-Cre, Kras*$^{G12D/+}$, *Trp53*$^{R172H/+}$, *Got1*$^{f/f,}$ and *Got2*$^{f/f}$ alleles from DNA isolated from mouse tails using standard methodology, using the primers listed below. Littermate controls were used in all experiments, and the sex ratios for each cohort were balanced.

For the double knockout Cre mice, mice were euthanized at 8 weeks to evaluate the pancreas and body weight. For the double knockout Cre mice used in the glucose tolerance test, mice were euthanized 1 week after test completion. Pancreata and plasma were collected for downstream analyses.

Mice in the KC experiment were euthanized at 6 or 12 months of age. Pancreata were collected for downstream analyses.

For the KPC study, mice were euthanized at humane endpoint according to veterinarian recommendations based on disease symptoms or at 20% body weight loss. Pancreata and plasma were collected for downstream analyses.

Cerulein treatment: Wildtype mice (2 male, 2 female) were injected with cerulein (Caerulein, Sulfated TS# J64320MCR) hourly for a total of 8 times on day one, followed the next day with 2 more injections and euthanasia an hour later. Cerulein was administered at 75ug/kg via intraperitoneal injection. At euthanasia, feces and pancreata were collected for downstream analysis, and blood was collected via cardiac puncture.

Orthotopic tumor implantation: Male 8- to 12-week-old C57BL/6J mice were obtained from The Jackson Laboratory (strain 000664) and maintained in the facilities of the Unit

for Laboratory Animal Medicine (ULAM) under specific pathogen-free conditions. Before tumor cell injection, wildtype or *Got1*-KO or *Got2*-KO mouse cell lines (derived from KPC 7940b) were collected from culture plates according to standard cell culture procedures. The cells were counted, washed once with PBS, and resuspended in a 1:1 solution of serum-free DMEM and Matrigel (Corning, 354234). For the orthotopic surgical procedure, mice were anaesthetized using inhalation isoflurane. The surgical site was sterilized by swabbing with iodine (Povidine-Iodine Prep Pad, PDI, B40600). This was followed by an incision on the left flank using sterilized instruments. Thereafter, the cell lines were injected into the pancreas, and the incision was sutured. Cell injection was as follows: 50,000 cells in 50 µl final volume for orthotopic implantation. Animals were monitored regularly in the post-operative period, and the orthotopic group was euthanized at post-implantation day 18. At endpoint, pancreata were weighed and preserved for further analyses.

Tissue processing: Mice were euthanized by CO2 asphyxiation or isoflurane overdose, followed by cervical dislocation. Tissue was quickly harvested and fixed at room temperature with zinc formalin fixative (Z-Fix; Anatech Ltd). Fixed tissues were transferred to 70% ethanol after 24 hours. Tissues were processed using a Leica ASP300S Tissue Processor (Leica Microsystems, Inc), paraffin embedded and cut into 5 µm sections. One section was stained for H&E for histological analysis.

Histology imaging and grading: Imaging was performed automatically using a whole-slide scanner (Vectra Polaris, Akoya Biosciences) or manually using an Olympus BX53F microscope. Whole-slide scanning was performed by the by the University of Michigan

Tissue & Molecular Pathology Shared Resource. For tissue grading, at least 3, 20x fields were reviewed by a pathologist and graded in a blinded manner.

Quantification of islet and acinar area: Hematoxylin and eosin-stained slides were digitally scanned and loaded into QuPath. Total tissue area was identified using a Pixel Classifier for detecting Average Channels with a sigma of 2 and threshold of 227. The spleen was manually removed from analyses. Islets and acinar area were manually annotated. Measurements were exported and analyzed to obtain percent acinar area and percent islet area.

Opal multiplex IHC staining: Blocks were cut into 5-micron slices and placed onto charged slides for processing. Slides were baked at 60℃ for 1 hour. Slides were subjected to deparaffinization and rehydration, then fixed with formalin. The multiplex staining was performed according to established protocols. (24) Using the OPAL 7 manual kit, the slides underwent six rounds of staining. Slides were prepared for each staining round using AR9 or AR6 Akoya Biosciences antigen retrieval buffer, followed by a primary antibody (F480 from Cell Signaling, cat #70076S;CD3 from Abcam, cat #Ab11089;CD8 from Cell Signaling, cat #98941;PDL1 from eBioscience, cat #14-5982-81;CK19 from DSHB, cat #Ab 2133570;FoxP3 from Cell Signaling, cat #12653). This was followed by secondary antibody stain (ImmPRESS HRP Goat Anti-Mouse IgG Polymer Detection Kit and ImmPRESS HRP Horse Anti-Rabbit IgG Polymer Detection Kit). Slides were counterstained using 4’,6-diamidino-2-phenylindole (DAPI), mounted, cover-slipped, and left to dry overnight. Using the PhenoImager HT (Akoya Biosciences), slides were imaged at 20x in all channels: DAPI, Opal 480, Opal 520,

Opal 570, Opal 620, Opal 690, and Opal 780. Composite images were created by automatically merging images from each channel and then taken for further analysis.

OPAL analysis: Images were analyzed using inForm Cell Analysis software (Perkin Elmer). All 90 images were batch analyzed using a subset of 13 randomly chosen tissue core images. A library was made using single-antigen staining for each fluorophore and used for unmixing and validation of the multiplex fluorescent composite staining, ensuring no spectral overlap between fluorophores. Using the inForm training software, DAPI counterstain was used to determine the size and shape of each nucleus, with a splitting sensitivity of 0.5. After cell segmentation, the following cells were phenotyped using the trainable software after select cells were manually assigned based on single staining criteria: T cells (CD3+), cytotoxic T cells (CD8+), macrophages (F480+), Tregs (FoxP3+), epithelial cells (CK19+). Fluorescent intensity scores of PD-L1, CD8, and FoxP3 were determined, which allowed for complex cell phenotyping using R. (24) After the fluorescent intensity score was determined for PD-L1, CD8, and FoxP3, using R programs in combination with the original cell phenotypes produced by inForm (T cell, APC, EC, and other), complex phenotypes were formulated. Final multiplex fluorescent composite images were reviewed with a trained pathologist to confirm the accuracy of staining and phenotyping.

Glucose tolerance test: After 5 hours fast, animals were given 50% glucose via oral gavage at 1~2.0g/kg. Blood samples are collected before and after gavage at time 0, 15, 30, 60, and 120 minutes via tail vein bleeding. Blood levels of glucose were measured using a glucometer (Acucheck, Roche), and plasma levels of insulin are determined using the Millipore rat/mouse insulin ELISA kit. Animals were restrained

repeatedly for less than a minute each time while blood samples were collected. HOMA-IR was calculated by multiplying fasting glucose by fasting insulin and dividing by 22.5. Glucose insulin index was calculated by multiplying the area under the curve of glucose and the area under the curve of insulin and 10^{-6}.

Amylase: Plasma obtained via tail vein bleed or cardiac puncture was used to quantify amylase in plasma using the Pointe Scientific Amylase Reagent (Fisher 23-666-111). Following the manufacturer's instructions, 10 µL of plasma was added to 400uL of reagent, followed by reading on a plate reader at 409nm with 3 readings taken over 2 minutes. To calculate the concentration of amylase in a sample in U/L, the average absorbance per minute was multiplied by the assay volume, then by 1000. This product was divided by the millimolar absorptivity of 2-chloro-p-nitrophenol times the sample volume times the light path.

(**Table 2-2**)

Statistics and reproducibility:

Figure 2-1: Mouse pancreatic functions are maintained without Got1 or Got2. C, Statistical significance was measured using two-tailed t-tests. For pancreatic weight, $p<0.0001$. For body weight, $p=0.0105$. For pancreatic weight/body weight, $p<0.0001$. E, Statistical significance was measured using a two-tailed t-test. $p<0.0001$. F, Statistical significance was measured using a two-tailed t-test. $p=0.7059$. G, Statistical significance was measured using a two-tailed unpaired t-test. $p=0.1455$. H, Statistical significance was measured using a two-tailed unpaired t-test. $p=0.0428$. I, The area under the curve (AUC) was calculated for each individual mouse. Statistical significance was measured

using a two-tailed unpaired t-test comparing the AUC of each group. p=0.6451. J, The area under the curve (AUC) was calculated for each individual mouse. Statistical significance was measured using a two-tailed unpaired t-test comparing the AUC of each group. p=0.1536. K, HOMA-IR was calculated by multiplying fasting glucose by fasting insulin and dividing by 22.5. Statistical significance was measured using a two-tailed unpaired t-test. p=0.1335. L, The glucose insulin index was calculated by multiplying the area under the curve of glucose and the area under the curve of insulin and 10^{-6}. Statistical significance was measured using a two-tailed unpaired t-test. p=0.4504. M, Statistical significance was measured using two-tailed unpaired t-tests. No serum control (2 wells of reagent only); Cerulein-treated wildtype mice (2 wells per mouse, n=4 mice); *Got1*$^{f/f}$*;Got2*$^{f/f}$ Cre negative mice (2 wells per mouse, n=5 mice); *Ptf1a-Cre*;*Got1*$^{f/f}$*;Got2*$^{f/f}$ mice (2 wells per mouse, n=2 mice). Comparing cerulein-treated to DKO, p <0.000001****. Comparing cerulein-treated to Cre- mice, p<0.000001****. Comparing DKO to Cre- mice, p=0.000030****. N-Q, Statistical significance was measured using two-tailed unpaired t-tests. N, Aspartate, p=0.0464* .O, glutamate, p=0.6654. P, α-ketoglutarate, p=0.4040. Q, lactate/pyruvate, p=0.2906.

Figure 2-2: Knockout of pancreatic Got1 or Got2 does not impact precancerous lesion formation. B, Statistical significance was measured with a two tailed unpaired t-test. Pancreas weight, p=0.8877. Body weight, p=0.8860. Pancreas/body weight, p=0.7337. C, Statistical significance was measured with a one-way ANOVA with Dunnet's multiple comparisons. pancreas weight, KC to KC;*Got2*$^{f/+}$, p=0.3368. KC to KC;*Got2*$^{f/f}$, p=0.3735. Body weight, KC to KC;*Got2*$^{f/+}$, p=0.0603. KC to KC;*Got2*$^{f/f}$, p=0.0370*. Pancreas/body weight, KC to KC;*Got2*$^{f/+}$, p=0.7527. KC to KC;*Got2*$^{f/f}$, p=0.9520. D,

Statistical significance was measured with a one-way ANOVA with Dunnet's multiple comparisons. pancreas weight, KC to KC;*Got1*$^{f/+}$, p=0.9569. KC to KC;*Got1*$^{f/f}$, p=0.3786. Body weight, KC to KC;*Got1*$^{f/+}$, p=0.3034. KC to KC;*Got1*$^{f/f}$, p=0.6767. Pancreas/body weight, KC to KC;*Got1*$^{f/+}$, p=0.9738. KC to KC;*Got1*$^{f/f}$, p=0.5312. E, Statistical significance was measured with a one-way ANOVA with Dunnet's multiple comparisons. pancreas weight, KC to KC;*Got2*$^{f/+}$, p=0.9412. KC to KC;*Got2*$^{f/f}$, p=0.8980. Body weight, KC to KC;*Got2*$^{f/+}$, p=0.9432. KC to KC;*Got2*$^{f/f}$, p=0. 9342. Pancreas/body weight, KC to KC;*Got2*$^{f/+}$, p=0.9178. KC to KC;*Got2*$^{f/f}$, p=0.9280. F, A KC;*Got2*$^{f/f}$ 12-month mouse was removed from the grading analysis after using Grubb's outlier test with an alpha of 0.2. Statistical significance was measured using one-way ANOVAs. Acinar, p=0.3400. ADM, p=0.2583. PanIN 1A, p=0.2740. PanIN 2, p=0.5996. PanIN 3, p=0.7651. PDAC, p=0.1406.

Figure 2-3: Loss of Got1 or Got2 does not improve survival in genetically engineered models of pancreatic cancer. B, Statistical significance of survival time was measured using a one-way ANOVA, p= 0.4689. Average survival time: KPC (n=6) 134.3 days, KPC;*Got1*$^{f/+}$ het (n=11) 128.2 days, KPC;*Got1*$^{f/f}$ null (n=5) 145.8 days. C, Statistical significance of survival time was measured using a one-way ANOVA, p= 0.7353. Average survival time: KPC (n=6) 134.3 days, KPC;*Got2*$^{f/+}$ het (n=12) 133.5 days, KPC;*Got2*$^{f/f}$ 143.7 days.

Figure 2-4: Got1 or Got2 loss does not alter the composition of immune and epithelial compartments in the tumor microenvironment. B, Analysis performed on KPC, KPC;*Got1*$^{f/+}$, and KPC;*Got1*$^{f/f}$ pancreata (n=5 mice per group). Statistical significance

was measured with one-way ANOVAs with Dunnet's multiple comparisons. CD3+/CD8-/FoxP3-; KPC to KPC;*Got1*$^{f/+}$, p=0.4200. KPC to KPC;*Got1*$^{f/f}$, p=0.8784. C, CD3+/CD8-/FoxP3+; KPC to KPC;*Got1*$^{f/+}$, p=0.9916. KPC to KPC;*Got1*$^{f/f}$, p=0.201*. D, CD3+/CD8+/FoxP3-; KPC to KPC;*Got1*$^{f/+}$, p=0.7204. KPC to KPC;*Got1*$^{f/f}$, p=0.4894. E, Total T Cells, KPC to KPC;*Got1*$^{f/+}$, p=0.5094. KPC to KPC;*Got1*$^{f/f}$, p=0.9351. F, F480+/PDL1-; KPC to KPC;*Got1*$^{f/+}$, p=0.7382. KPC to KPC;*Got1*$^{f/f}$, p=0.6963. G, F480+/PDL1+; KPC to KPC;*Got1*$^{f/+}$, p=0.3500. KPC to KPC;*Got1*$^{f/f}$, p=0.5652. H, F480+; KPC to KPC;*Got1*$^{f/+}$, p=0.7376. KPC to KPC;*Got1*$^{f/f}$, p=0.6958.I, CK19+/PDL1-; KPC to KPC;*Got1*$^{f/+}$, p=0.9953. KPC to KPC;*Got1*$^{f/f}$, p=0.5750. J, CK19+/PDL1+; KPC to KPC;*Got1*$^{f/+}$, p=0.8662. KPC to KPC;*Got1*$^{f/f}$, p=0.9946.K, CK19+; KPC to KPC;*Got1*$^{f/+}$, p=0.9893. KPC to KPC;*Got1*$^{f/f}$, p=0.5742. L, Analysis performed on KPC, KPC;*Got2*$^{f/+}$, and KPC;*Got2*$^{f/f}$ pancreata (n=5 mice per group). Statistical significance was measured with one-way ANOVAs with Dunnet's multiple comparisons. CD3+/CD8-/FoxP3-; KPC to KPC;*Got2*$^{f/+}$, p=0.9672 . KC to KPC;*Got2*$^{f/f}$, p=0.5817. M, CD3+/CD8-/FoxP3+; KPC to KPC;*Got2*$^{f/+}$, p=0.0084** . KC to KPC;*Got2*$^{f/f}$, p= 0.8722. N, CD3+/CD8+/FoxP3-; KPC to KPC;*Got2*$^{f/+}$, p=0.2592 . KC to KPC;*Got2*$^{f/f}$, p=0.8374. O, Total T Cells; KPC to KPC;*Got2*$^{f/+}$, p=0.8970 . KC to KPC;*Got2*$^{f/f}$, p=0.6198.P, F480+/PDL1-; KPC to KPC;*Got2*$^{f/+}$, p=0.5403 . KC to KPC;*Got2*$^{f/f}$, p=0.7421.Q, F480+/PDL1+; KPC to KPC;*Got2*$^{f/+}$, p=0.9665 . KC to KPC;*Got2*$^{f/f}$, p=0.1716. R, F480+; KPC to KPC;*Got2*$^{f/+}$, p=0.5404 . KC to KPC;*Got2*$^{f/f}$, p=0.7414. S, CK19+/PDL1-; KPC to KPC;*Got2*$^{f/+}$, p=0.2352. KC to KPC;*Got2*$^{f/f}$, p=0.3086. T, CK19+/PDL1+; KPC to KPC;*Got2*$^{f/+}$, p=0.9479. KC to KPC;*Got2*$^{f/f}$, p=0.7145. U, CK19+; KPC to KPC;*Got2*$^{f/+}$, p=0.2715. KC to KPC;*Got2*$^{f/f}$, p=0.3132

Figure 2-5: PDAC cells adapt their metabolism to counter GOT loss. B, Statistical significance was measured with a one-way ANOVA with Dunnett's multiple comparisons. sgNT to Got1 sg1, p=0.9967. sgNT to Got2 sg1, p=0.5040. sgNT to Got2 sg2, p=0.5915. C, Statistical significance was measured with a one-way ANOVA with Dunnett's multiple comparisons. sgNT to Got1 sg1, p=0.9951. sgNT to Got2 sg1, p=0.4177. F-M, Statistical significance was measured with a one-way ANOVA with Dunnet's multiple comparisons. F, Aspartate; MT3: NT to Got1 sg1, 0.0030**. NT to Got2 sg1, 0.0847. G, 7940B: NT to Got1 sg1, p=0.0564. NT to Got2 sg1, p=0.0681. NT to Got2 sg2, p=0.1598. H, Glutamate; MT3: NT to Got1, 0.5402, NT to Got2 sg1, 0.0081**. I, 7940B: NT to Got1 sg1, 0.1594. NT to Got2 sg1, 0.5562. NT to Got2 sg2, 0.3036. J, αKG; MT3: NT to Got1 sg1, p= 0.4166. NT to Got2 sg1, p=0.2319. K, 7940B: NT to Got1 sg1, p=0.3497. NT to Got2 sg1, p=0.3497. NT to Got2 sg2, p=0.1365. L, Lactate/pyruvate; MT3: NT to Got1 sg1, p= 0.<0.0001****. NT to Got2 sg1, p=0.0382*. M, 7940B: NT to Got1 sg1, p=0.0113*. NT to Got2 sg1, p=0.0380*. NT to Got2 sg2, p=0.0309*. N, Statistical significance was measured with two tailed unpaired t-tests (n=5 mice per group). Pancreas weight, p= 0.8230. body weight, p= 0.4937. Pancreas/body weight, p= 0.6871. O, Statistical significance was measured with one-way ANOVAs (n=5 mice per group) with Dunnett's multiple comparisons. Pancreas weight, sgNT to Got2 sg1, p=0.9904. sgNT to Got2 sg2, p=0.9954. Body weight, sgNT to Got2 sg1, p=0.4571. sgNT to Got2 sg2, p=0.6886. Pancreas/Body weight, sgNT to Got2 sg1, p=0.8335. sgNT to Got2 sg2, p=0.9609.

Supplementary Figure 2-1 B, Heatmap was generated identifying metabolites with a p-value<0.1 compared to the control sample (Cre negative mice). Samples included pancreata of 8-week old *Got1$^{f/f}$;Got2$^{f/f}$* (n=4) or *Ptf1a-Cre*;*Got1$^{f/f}$;Got2$^{f/f}$* (n=3) mice

Supplementary Figure 2-2 A, Statistical significance was measured with a one-way ANOVA with Dunnet's multiple comparisons. Pancreas weight, KPC to KPC;*Got1$^{f/f}$,* p=0.6485. KPC to KPC;*Got1$^{f/f}$*, p=0.3787. Body weight, KPC to KPC;*Got1$^{f/f}$,* p=0.9860. KPC to KPC;*Got1$^{f/f}$*, p=0.3603. Pancreas/Body weight, KPC to KPC;*Got1$^{f/f}$,* p=0/7897. KPC to KPC;*Got1$^{f/f}$*, p=0.6374. B, Statistical significance was measured with a one-way ANOVA with Dunnet's multiple comparisons. Pancreas weight, KPC to KPC;*Got2$^{f/+}$,* p=0.7890. KPC to KPC;*Got2$^{f/f}$*, p=0.9039. Body weight, KPC to KPC;*Got2$^{f/+}$,* p=0.9974. KPC to KPC;*Got2$^{f/f}$*, p=0.3601. Pancreas/Body weight, KPC to KPC;*Got2$^{f/+}$,* p=0.7340. KPC to KPC;*Got2$^{f/f}$*, p=0.9923.

Supplementary Figure 2-3 Heatmap was generated identifying metabolites with a p-value<0.1 compared to the control sample (sgNT cell lines). n=3 biologically independent samples per group.

Supplementary Figure 2-4 Heatmap was generated identifying metabolites with a p-value<0.1 compared to the control sample (sgNT cell lines). n=3 biologically independent samples per group.

Supplementary Figure 2-5 Heatmaps were generated identifying metabolites with a p-value<0.1 compared to the control sample (sgNT cell lines). n=3 biologically independent samples per group, n=2 for Got2 sg2.

Supplementary Figure 2-6 Heatmaps were generated identifying metabolites with a p-value<0.1 compared to the control sample (sgNT cell lines). n=3 biologically independent samples per group, n=2 for Got2 sg2.

2.4 Results

2.4.1 Mouse pancreatic functions are maintained without Got1 or Got2.

To determine the dependence of normal pancreas development on the GOTs, we crossed *Got1*$^{f/f}$ and *Got2*$^{f/f}$ mice with the pancreas-specific *Ptf1a-Cre* to generate a conditional knockout of *Got1* and *Got2* (**Figure 2-1B**). We previously published that the single knockout of *Got2* in the pancreas had no observable impact on pancreatic morphology (17), and similarly we did not observe differences between the knockouts and controls. Accordingly, wild type and single knockouts are used as controls for the double knockout studies (**Figure 2-1C**). While mice with conditional knockout of both *Got1* and *Got2* are viable, their body weight trailed that of their age-matched controls (by ~5g on average) but otherwise appeared healthy. Further, analysis of pancreata from double knockout mice taken down at 8 weeks of age revealed significantly smaller pancreata compared to single and wildtype animals (**Figure 2-1C**).

Histological analysis of double knockout pancreata revealed a significant morphological defect when both *Got1* and *Got2* were lost, compared to the loss of either enzyme alone (**Figure 2-1D**). (17) Notable were the loss of acinar tissue area and its repopulation with fat. Using hematoxylin and eosin stains for 8-week-old *Ptf1a-Cre*;*Got1*$^{f/f}$ (n=3) and *Ptf1a-Cre*;*Got1*$^{f/f}$*;Got2*$^{f/f}$ mice (n=6), we quantified the acinar and islet area of pancreatic samples. We found that the area of acinar cells was significantly

reduced in double knockout mice (**Figure 2-1D-E**) without an impact on the area of islets (**Figure 2-1F**). This phenotype is also seen when comparing *Ptf1a-Cre*;*Got1*$^{f/f}$;*Got2*$^{f/f}$ and *Got1*$^{f/f}$;*Got2*$^{f/f}$ (Cre negative) pancreata (**Supplementary Figure 2-1A**). Next, we performed targeted mass spectrometry-based metabolomics on these pancreata. Consistent with the tissue level disturbances, the metabolome was widely changed (**Supplementary Figure 2-1C**), which may simply be a result of changes to cellular composition of the tissue. In addition, we observed metabolic shifts coherent with GOT knockout, including a decrease in aspartate and indications of NADH reductive stress (**Figure 2-1N-Q, Supplementary Figure 2-1D**). Together, these data illustrate that the loss of *Got1* and *Got2* have a significant impact on pancreatic development, and we questioned whether these mice also had defects in pancreatic exocrine and endocrine function.

Using a separate cohort of double knockout or wildtype female mice, we found that after a 5-hour fast, fasted blood glucose was not significantly altered in double knockout or wildtype animals (n=4 for Cre- control; n=3 for double knockout) (**Figure 2-1G**). However, fasting insulin was slightly elevated in double knockout mice (**Figure 2-1H**). After fasting, mice were subjected to a glucose tolerance test. Here, mice were provided with 1.5g/kg of glucose via oral gavage, followed by tail vein blood extraction at 0, 15, 30, 60, and 120 minutes. Here, we find that double knockout animals do not have improved or worsened glucose tolerance or insulin sensitivity compared to control mice (**Figure 2-1I, J**). Further, *Got1* and *Got2* loss show no significant impact on Glucose Insulin Index or the Homeostasis Model Assessment of Insulin Resistance (HOMA-IR) Index (**Figure 2-1K, L**). These findings indicate that the available endocrine

cells in double knockout pancreata are sufficient to retain normal pancreatic endocrine function.

When acinar cells are damaged, amylase is released into the bloodstream. (22, 23) Therefore, to evaluate exocrine function, we measured circulating amylase in the blood in a cohort of double knockout mice and Cre-negative controls. We also included cerulein-treated wildtype mice, which develop pancreatic injury and lesion formation, as a positive control. As expected, cerulein-treated mice (n=4) have high amylase in plasma, ~4-fold above untreated mice of both genotypes (**Figure 2-1M**). Double knockout mice (n=2) have significantly lower plasma amylase levels than controls (n=5), potentially reflective of the lower acinar content (**Figure 2-1M**). As a further measure, feces from the double knockout animals are grossly indistinguishable from controls, further supporting that digestion is overtly normal. Together, these data demonstrate the loss of *Got1* and *Got2* from the pancreas causes a severe disturbance in pancreatic morphology, yet these mice are viable and retain normal pancreatic exocrine and endocrine function at the ages examined.

2.4.2 Knockout of pancreatic Got1 or Got2 does not impact precancerous lesion formation.

Due to the prominent tissue-level defects of *Got1* and *Got2* dual knockout, we elected to use a single knockout of *Got1* or *Got2* for subsequent genetic models of pancreatic cancer. To evaluate whether GOT1 or GOT2 affects the development of precancerous lesions, a first step toward PDAC, we crossed the *Got* floxed alleles with the “KC” mouse model. This model expresses a mutant Kras allele (LSL-$Kras^{G12D/+}$) driven by the pancreas-specific *Ptf1a-Cre* to drive the development of pancreatic lesions

and early neoplasia that precedes PDAC (**Figure 2-2A**). KC (n=4), KC;*Got1*$^{f/f}$ (n=3), KC;*Got2*$^{f/+}$ (n=10), and KC;*Got2*$^{f/f}$ (n=5) mice were aged to 6 months, and KC (n=4), KC;*Got1* $^{f/+}$ KC (n=3);*Got1*$^{f/f}$ (n=8), KC;*Got2*$^{f/+}$ (n=3), and KC;*Got2*$^{f/f}$ (n=4) mice were aged to 12 months, which are well established timepoints to assess the presence of pancreatic transformation. At these endpoints, animals were sacrificed, and pancreata were harvested and processed for histological examination. At both the 6-month and 12-month timepoints, there was no significant difference in animal body weight or pancreas weight for either genotype of KC;*Got* mice (**Figure 2-2B-E**). Histology from these mice revealed similar levels of metaplasia, lesions, and fibrosis across each group (**Figure 2-2G**). By 12 months of age, some lesions in KC mice can advance to PDAC. A cohort of the 12-month pancreata was further analyzed histologically to grade lesions and calculate the percent tumor area in mice where lesions progressed to PDAC (KC n=3, KC;*Got1*$^{f/f}$ n=5, KC;*Got2*$^{f/f}$ n=5). In this cohort, no wildtype KC mice developed tumors by 12 months, and 2 of 5 *Got1* knockout and 1 of 5 *Got2* knockout pancreata evaluated had small areas of PDAC. However, grading these 12-month-old KC mice revealed was no significant difference among the groups for any of the lesion grades evaluated (**Figure 2-2F**). Additionally, we did not observe any obvious tissue-level morphological differences among genotypes (**Figure 2-2G-H, Supplementary Figure 2-2C**). Together, these data suggest that loss of *Got1* or *Got2* is not protective against pancreatic precancerous lesion formation.

2.4.3 Loss of Got1 or Got2 does not improve survival in genetically engineered models of pancreatic cancer.

Next, we assessed the role of the GOT enzymes in PDAC using the most well established genetically engineered mouse model of PDAC progression. In the KPC model, mice are engineered to express a mutant Kras G12D allele and a mutant TP53 allele (*Tp53* $^{R17H2/+}$) driven by the pancreas-specific *Ptf1a-Cre* (**Figure 2-3A**). This drives pancreatic cancer formation that advances to PDAC. To this, we crossed our *Got1* or *Got2* floxed mice. Cohorts of at least 5 mice from each genotype were followed until they died naturally or required sacrifice due to being moribund: KPC (n=6), KPC;*Got1*$^{f/+}$ het (n=11), KPC;*Got1*$^{f/f}$ null (n=5), KPC;*Got2*$^{f/+}$ het (n=12), or KPC;*Got2*$^{f/f}$ null (n=11). Among this large cohort of animals, we did not observe significant survival differences among any of the genotypes (**Figure 2-3B-C**). The mean mortality for each genotype was within a range of 17 days: KPC 134.3 days, KPC;*Got1*$^{f/+}$ 128.2 days, KPC;*Got1*$^{f/f}$ 145.8 days, KPC;*Got2*$^{f/+}$ 133.5 days, KPC;*Got2*$^{f/f}$ 143.7 days. These mice were euthanized at various timepoints based upon onset of moribundity; however, within these timepoints, we did not observe any major aberrations in tumor or body weight among our genotypes (**Supplementary Figure 2-2A-B**). Additionally, we did not observe differences in tumor morphology among genotypes (**Figure 2-3D**). Together, these data indicate that loss of *Got1* or *Got2* does not improve survival in this genetically engineered mouse model of PDAC.

2.4.4 Got1 or Got2 loss in the endogenous KPC tumor model does not alter the composition of immune and epithelial compartments in the tumor microenvironment.

A recent study illustrated that *Got2* knockout in syngeneic, orthotopic PDAC models reduces tumor size and that this is dependent on the activity of T cells. (21) Although we did not observe an effect on tumor size from either *Got1* or *Got2* loss in our

KPC models, we next sought to interrogate whether T cell quantity or subtype was affected by the knockout of *Got1* or *Got2*. Here, we conducted multiplex immunofluorescence (IF) staining on KPC, KPC;*Got1*$^{f/+}$, KPC;*Got1*$^{f/f}$, KPC;*Got2*$^{f/+}$, and KPC;*Got2*$^{f/f}$ tumors (n=5 per group). Our multiplex IF panel focused on the quantification of T cells, macrophages, and epithelial cells in these KPC tumors. This included staining for DAPI (nuclei), F480 (macrophages), CD3 (T cells), CD8 (cytotoxic T cells), PDL1 (immune evasiveness), CK19 (epithelial cells), and FoxP3 (Tregs) (**Figure 2-4A, Supplementary Figure 2-2C**). These data were then quantified using the inForm software. (24-27) This enabled us to calculate cellular phenotypes and quantities. In the KPC model without disruption of *Got1* or *Got2*, most of the evaluated cell types were epithelial cells and macrophages, with few T cells; data that align with the previous analyses of KPC tumors (**Figure 2-4B-U**). (28, 29) Most of the macrophages and epithelial cells were PDL1-, which corresponds with PDAC tumors being largely unresponsive to single-agent treatment with PDL1 immunotherapies in the clinic (**Figure 2-4F, I, P, S**). (30) Compared to macrophages, T cells were in very low abundance (~2% of all cells), again in line with human PDAC and previous analyses of KPC tumors (**Figure 2-4E, O**). (31) Compared to the *Got1* and *Got2* knockout tumors, there were no meaningful differences in epithelial or immune cell populations across tumors. This includes no statistical difference amongst the quantity of different T cell populations, including CD3+/CD8-/FoxP3- helper T cells, and CD3+/CD8+/FoxP3- effector CD8+ T cells (**Figure 2-4B-E, L-O**). We did, however, detect a minor increase in CD3+/CD8-/Fox3P+ Tregs in KPC;*Got1*$^{f.f}$ and KPC;*Got2*$^{f/+}$ mice, however, these Tregs make up <0.4% of cells (**Figure 2-4C, M**). We also did not observe a difference in F480+/PDL1+

or F480+/PDL1- macrophages or CK19+/PDL1+ or CK19+/PDL1- epithelial cells (**Figure 2-4F-K, P-U**). Together, these data demonstrate that *Got1* or *Got2* loss has minimal impact on the immune and epithelial cellular compartments of the TME.

2.4.5 PDAC cells adapt their metabolism to counter GOT loss.

The tissue complexity and limited number of cancer cells in the autochthonous PDAC tumors (~30%, **Figure 2-4U**) presents a challenge to studying metabolic reprogramming. Thus, we utilized syngeneic KPC cell line-based models to study the cell-autonomous impacts of GOT1 and GOT2. We used CRISPR/Cas9 to knock out *Got1* and *Got2* in the MT3 and 7940B KPC cell lines (**Figure 2-5A**). Next, in standard cell culture media, we evaluated whether the loss of either enzyme alone affects proliferation of pooled populations, relative to cells harboring a non-targeting sgRNA (sgNT). *Got* knockout did not have a negative effect on proliferation, with a trend toward faster proliferation in the Got1 sg1 condition in both cell lines (**Figure 2-5B,C**).

Next, we assessed metabolic programs in these cells by measuring oxygen consumption rates and changes to the metabolome by mass spectrometry-based metabolomics. While loss of *Got1* or *Got2* did not negatively oxygen consumption rate (**Figure 2-5D,E**), we observed widespread changes to both the intracellular and extracellular metabolomes (**Supplementary Figure 2-3-6**). Notably, aspartate levels tracked with the canonical directionality of the GOTs, with aspartate levels increasing in GOT1 knockouts and aspartate levels decreasing in the GOT2 knockouts (**Figure 2-5F,G**). Changes to levels of the other GOT substrates were not consistent (**Figure 2-5H-K**), in line with our previous observations (15, 17, 19), and the buffering of glutamate and α-ketoglutarate levels by many other enzymes. We also observed indicators of

NADH reductive stress, including a significant increase in the lactate to pyruvate ratio (**Figure 2-5L,M**).

We then wanted to determine if these metabolic changes would impact tumor growth using an orthotopic, immunocompetent model of PDAC. This also allowed us to compare if GOT knockout impacted the take or growth of established tumors, relative to our observations on tumor development and progression using the autochthonous models. To this end, we implanted our Got knockout 7940B KPC cells into the pancreas of B6 mice. Analysis of tumor weight at endpoint revealed that neither *Got1* nor *Got2* loss had a deleterious impact on tumor growth (**Figure 2-5N,O**). The results from this experiment provide data from a third distinct, immune competent model of PDAC, which all collectively illustrate that the GOTs are dispensable in pancreatic tumorigenesis, tumor growth, and tumor progression. They also serve to further underscore the adaptability of pancreatic tumor metabolism.

2.5 Discussion

The concentration of aspartate in the serum is lower than that of all other amino acids, typically low to sub-micromolar. Rather, as a non-essential amino acid, aspartate is created in cells by the GOTs as needed. This suggests that excretory, protein-producing cells should require GOT activity. Single loss of either *Got1* or *Got2* in the pancreas, using the pancreas-specific Ptf1a-Cre, has no apparent impact on pancreatic formation or function. Canonically, mitochondrial GOT2 makes aspartate, which is released into the cytosol by the mitochondrial aspartate-glutamate transporter ARALAR. In the cytosol, GOT1 can act on aspartate and α-ketoglutarate to make glutamate and oxaloacetate. In the absence of GOT2, we speculate that GOT1 runs the canonically

reverse reaction to produce aspartate. Indeed, when we fully block aspartate production with dual, pancreas-specific loss of *Got1* and *Got2*, the number of digestive enzyme-producing acinar cells in the pancreas is severely restricted, leading to a much smaller pancreas. Despite this, mice with Got-less acinar cells are viable and do not exhibit overt challenges to digestion, with the potential exception of being slightly smaller in weight. This suggests that a mere fraction of normal pancreas is sufficient to retain normal pancreas function, but more work is necessary to delineate the specific needs of a functioning pancreas.

We speculate that the deleterious impact of Got loss on the exocrine pancreas results from a differentiation defect limiting acinar cell maturation or via cell death or mature acinar cells limited in aspartate. In contrast to acinar cells, total islet area was unaffected by loss of the *Got*s, and the loss of these enzymes did not significantly impact glucose or insulin sensitivity. However, Ptf1a-Cre is less penetrant in the endocrine lineage, and some *Got* expression remains. As such, our observations instead reveal that the major structural impacts to the exocrine pancreas do not appear to impact endocrine function.

Beyond its role in protein biosynthesis, aspartate is also an essential building block for nucleotides and other amino acids, highlighting the potential importance of the GOTs for the biosynthetic needs of proliferating cells. (16, 18) Further, the action of the GOTs within the MAS are also important mediators of redox balance through their downstream impacts on NADH/NAD^+ ratios. (15) Together, the physiological roles of the GOTs and the MAS suggest a potential importance of these pathways in cancer cells, where redox imbalances and biosynthetic needs are paramount. (7, 15, 32) Despite

these important functions, we find that the pancreas-specific loss of *Got1* or *Got2* does not protect against precancerous lesions or reduce PDAC tumor size using orthotopic and genetic models of pancreatic cancer *in vivo.*

Our data herein add to a growing body of work on the role of GOTs in PDAC and include some conflicting observations. Over a decade ago, we demonstrated that PDAC cells rely on the metabolism of glutamine-derived carbon through the activity of GOT1 in a pathway regulated by mutant KRAS. (15) Using human cell culture models *in vitro* and immunocompromised xenograft mouse models, we showed that genetic GOT1 inhibition slows PDAC growth and leads to oxidative stress, which sensitizes cells to ferroptosis. (19)

We also explored the role of GOT2 in pancreatic cancer. Using human cell line models *in vitro*, we found that genetic inhibition of GOT2 reduces PDAC cell proliferation. (17) In contrast, after implanting human PDAC cell lines subcutaneously or orthotopically into nude mice, we found that genetic inhibition of *GOT2* does not impair tumor growth. In the genetically engineered KC model, $Got2^{f/f}$ knockout had no impact on disease progression. Subsequent studies *in vitro* using human PDAC cell lines revealed that GOT2 knockdown led to NADH reductive stress, which inhibited proliferation. Reversal of the NADH burden restored proliferation. Indeed, we demonstrated conditioned media from cancer associated fibroblasts could rescue GOT2 proliferative defects in vitro, and this activity was attributed to pyruvate, potentially explaining why *Got2* loss does not affect tumor growth. (17) A related study also found that GOT2 knockout had no impact on PDAC tumor growth using human cell lines in immune compromised animals. (20) Further, they demonstrated that aspartate

auxotrophic tumors (double GOT1-GOT2 knockout), while slower growing, maintained aspartate levels through macropinocytosis, providing important new mechanistic insights into how tumors cope with GOT loss.

In contrast to the GOT2 results using human cell lines in immune compromised mice described above, it was reported that *Got2* knockout using murine KPC cells and syngeneic, orthotopic transplantation resulted in markedly reduced tumor growth. (15, 19) Tumor growth inhibition was ascribed to tumor-infiltrating T cells and a decrease in immunosuppressive macrophages in this immune competent model.

Building on our previous work studying GOTs in human cell lines and immune compromised transplant models, here we utilized mouse models pancreatic cancer development and progression *in vivo*, along with orthotopic animal models and cell line models. We find that murine tumor development, progression, and established tumor models appear largely, if not completely, unaffected by *Got1* or *Got2* loss. These results are harmonious with previous work on GOT2 in human models (17, 20) yet contrast those from another mouse study. (21) These new results also stand in contrast to our previous work on GOT1 in human models. (15, 19) It is likely that we can fully reconcile these discrepancies by simply considering the features of the model systems employed. Such results also serve to highlight concerns with reproducibility amongst scientific studies, which may not in fact be issues with reproducibility but rather a consequence of the myriad variables associated with studying cancer in animals.

Finally, the observation that PDAC tumors can develop, grow, and progress without Got1 or Got2 highlights the adaptability of cancer metabolism. Indeed, a wealth of studies detail the metabolic flexibility of PDAC, including their ability to engage

various recycling and scavenging pathways, as well as intratumoral metabolic crosstalk pathways, to facilitate growth and survival. For example, our metabolomics data and that of others indicates isoform compensation for aspartate biosynthesis. Additionally, aspartate auxotrophic tumors overcome dual GOT loss by utilizing macropinocytosis to scavenge for environmental aspartate. (20) Single Got knockout will also disable the malate-aspartate shuttle and thus lead to NADH/NAD+ redox imbalance. Our previous work on fibroblast-derived pyruvate release may provide a mechanism to overcome NADH stress. (17) Future work will be necessary to study these metabolic compensatory mechanisms.

2.6 References

1. Wood, L. D., Canto, M. I., Jaffee, E. M., & Simeone, D. M. (2022). Pancreatic cancer: pathogenesis, screening, diagnosis, and treatment. *Gastroenterology*, *163*(2), 386-402.

2. Siegel, R. L., Miller, K. D., Wagle, N. S., & Jemal, A. (2023). Cancer statistics, 2023. *CA: a cancer journal for clinicians*, *73*(1).

3. National Cancer Institute. (2025). Surveillance, epidemiology, and end results (SEER) program. *Cancer Statistics, SEER Data & Software, Registry Operations*.

4. Koong, A. C., Mehta, V. K., Le, Q. T., Fisher, G. A., Terris, D. J., Brown, J. M., ... & Vierra, M. (2000). Pancreatic tumors show high levels of hypoxia. *International Journal of Radiation Oncology* Biology* Physics*, *48*(4), 919-922.

5. Kamphorst, J. J., Nofal, M., Commisso, C., Hackett, S. R., Lu, W., Grabocka, E., ... & Rabinowitz, J. D. (2015). Human pancreatic cancer tumors are nutrient poor and tumor cells actively scavenge extracellular protein. *Cancer research*, *75*(3), 544-553.

6. Encarnacion-Rosado, J., & Kimmelman, A. C. (2021). Harnessing metabolic dependencies in pancreatic cancers. *Nature Reviews Gastroenterology & Hepatology*, *18*(7), 482-492.

7. Halbrook, C. J., Lyssiotis, C. A., di Magliano, M. P., & Maitra, A. (2023). Pancreatic cancer: advances and challenges. *Cell*, *186*(8), 1729-1754.

8. Nwosu, Z. C., Ward, M. H., Sajjakulnukit, P., Poudel, P., Ragulan, C., Kasperek, S., ... & Lyssiotis, C. A. (2023). Uridine-derived ribose fuels glucose-restricted pancreatic cancer. *Nature*, *618*(7963), 151-158.

9. Cheng, C., Hu, J., Mannan, R., He, T., Bhattacharyya, R., Magnuson, B., ... & Chinnaiyan, A. M. (2025). Targeting PIKfyve-driven lipid metabolism in pancreatic cancer. *Nature*, 1-9.

10. Santana-Codina, N., Roeth, A. A., Zhang, Y., Yang, A., Mashadova, O., Asara, J. M., ... & Kimmelman, A. C. (2018). Oncogenic KRAS supports pancreatic cancer through regulation of nucleotide synthesis. *Nature communications*, *9*(1), 4945.

11. Ying, H., Kimmelman, A. C., Lyssiotis, C. A., Hua, S., Chu, G. C., Fletcher-Sananikone, E., ... & DePinho, R. A. (2012). Oncogenic Kras maintains pancreatic tumors through regulation of anabolic glucose metabolism. *Cell*, *149*(3), 656-670.

12. Hingorani, S. R., Wang, L., Multani, A. S., Combs, C., Deramaudt, T. B., Hruban, R. H., ... & Tuveson, D. A. (2005). Trp53R172H and KrasG12D cooperate to promote chromosomal instability and widely metastatic pancreatic ductal adenocarcinoma in mice. *Cancer cell*, *7*(5), 469-483.

13. Collins, M. A., Bednar, F., Zhang, Y., Brisset, J. C., Galbán, S., Galbán, C. J., ... & Di Magliano, M. P. (2012). Oncogenic Kras is required for both the initiation and maintenance of pancreatic cancer in mice. *The Journal of clinical investigation*, *122*(2), 639-653.

14. Drizyte-Miller, K., Talabi, T., Somasundaram, A., Cox, A. D., & Der, C. J. (2025). KRAS: the Achilles' heel of pancreas cancer biology. *The Journal of Clinical Investigation*, *135*(16).

15. Son, J., Lyssiotis, C. A., Ying, H., Wang, X., Hua, S., Ligorio, M., ... & Kimmelman, A. C. (2013). Glutamine supports pancreatic cancer growth through a KRAS-regulated metabolic pathway. *Nature*, *496*(7443), 101-105.

16. Borst, P. (2020). The malate–aspartate shuttle (Borst cycle): How it started and developed into a major metabolic pathway. *IUBMB life*, *72*(11), 2241-2259.

17. Kerk, S. A., Lin, L., Myers, A. L., Sutton, D. J., Andren, A., Sajjakulnukit, P., ... & Lyssiotis, C. A. (2022). Metabolic requirement for GOT2 in pancreatic cancer depends on environmental context. *Elife*, *11*, e73245.

18. Birsoy, K., Wang, T., Chen, W. W., Freinkman, E., Abu-Remaileh, M., & Sabatini, D. M. (2015). An essential role of the mitochondrial electron transport chain in cell proliferation is to enable aspartate synthesis. *Cell*, *162*(3), 540-551.

19. Kremer, D. M., Nelson, B. S., Lin, L., Yarosz, E. L., Halbrook, C. J., Kerk, S. A., ... & Lyssiotis, C. A. (2021). GOT1 inhibition promotes pancreatic cancer cell death by ferroptosis. *Nature communications*, *12*(1), 4860.

20. Garcia-Bermudez, J., Badgley, M. A., Prasad, S., Baudrier, L., Liu, Y., La, K., ... & Birsoy, K. (2022). Adaptive stimulation of macropinocytosis overcomes aspartate limitation in cancer cells under hypoxia. *Nature Metabolism*, *4*(6), 724-738.

21. Abrego, J., Sanford-Crane, H., Oon, C., Xiao, X., Betts, C. B., Sun, D., ... & Sherman, M. H. (2022). A cancer cell–intrinsic GOT2–PPARδ axis suppresses antitumor immunity. *Cancer discovery*, *12*(10), 2414-2433.

22. Janowitz, H. D., & Dreiling, D. A. (1959). The plasma amylase: source, regulation and diagnostic significance. *The American journal of medicine*, *27*(6), 924-935.

23. Banks, P. A. (1997). Practice guidelines in acute pancreatitis. *American Journal of Gastroenterology (Springer Nature)*, *92*(3).

24. Lazarus, J., Maj, T., Smith, J. J., Lanfranca, M. P., Rao, A., D'Angelica, M. I., ... & Frankel, T. L. (2018). Spatial and phenotypic immune profiling of metastatic colon cancer. *JCI insight*, *3*(22), e121932.

25. Griffith, B. D., Lazarus, J., McGue, J., Krishnan, S., D'Angelica, M. I., Shia, J., ... & Frankel, T. L. (2023). Unique characteristics of the tumor immune microenvironment in young patients with metastatic colorectal cancer. *Frontiers in Immunology*, *14*, 1289402.

26. Griffith, B. D., Turcotte, S., Lazarus, J., Lima, F., Bell, S., Delrosario, L., ... & Frankel, T. L. (2022). MHC class II expression influences the composition and distribution of immune cells in the metastatic colorectal cancer microenvironment. *Cancers*, *14*(17), 4092.

27. McGue, J. J., Edwards, J. J., Griffith, B. D., & Frankel, T. L. (2023). Multiplex fluorescent immunohistochemistry for preservation of tumor microenvironment architecture and spatial relationship of cells in tumor tissues. In *Cancer Systems and Integrative Biology* (pp. 235-246). New York, NY: Springer US.

28. Di Caro, G., Cortese, N., Castino, G. F., Grizzi, F., Gavazzi, F., Ridolfi, C., ... & Marchesi, F. (2016). Dual prognostic significance of tumour-associated macrophages in human pancreatic adenocarcinoma treated or untreated with chemotherapy. *Gut*, *65*(10), 1710-1720.

29. Balachandran, V. P., Łuksza, M., Zhao, J. N., Makarov, V., Moral, J. A., Remark, R., ... & ARC-Net Centre for Applied Research on Cancer Scarpa Aldo 41 Lawlor Rita T. 41 Beghelli Stefania 41 Corbo Vincenzo 41 Scardoni Maria 41 Bassi Claudio 41. (2017). Identification of unique neoantigen qualities in long-term survivors of pancreatic cancer. *Nature*, *551*(7681), 512-516.

30. Brahmer, J. R., Tykodi, S. S., Chow, L. Q., Hwu, W. J., Topalian, S. L., Hwu, P., ... & Wigginton, J. M. (2012). Safety and activity of anti–PD-L1 antibody in patients with advanced cancer. *New England journal of medicine*, *366*(26), 2455-2465.

31. Brouwer, T. P., de Vries, N. L., Abdelaal, T., Krog, R. T., Li, Z., Ruano, D., ... & de Miranda, N. F. (2022). Local and systemic immune profiles of human pancreatic ductal adenocarcinoma revealed by single-cell mass cytometry. *Journal for Immunotherapy of Cancer*, *10*(7), e004638.

32. Panieri, E., & Santoro, M. M. (2016). ROS homeostasis and metabolism: a dangerous liason in cancer cells. *Cell death & disease*, *7*(6), e2253-e2253.

33. Sanjana, N. E., Shalem, O., & Zhang, F. (2014). Improved vectors and genome-wide libraries for CRISPR screening. *Nature methods*, *11*(8), 783-784.

34. Shalem, O., Sanjana, N. E., Hartenian, E., Shi, X., Scott, D. A., Mikkelsen, T. S., ... & Zhang, F. (2014). Genome-scale CRISPR-Cas9 knockout screening in human cells. *Science*, *343*(6166), 84-87.

35. Pourmandi, N., Myers, G., Jha, A., Temprine, K., Sankar, A., Das, N. K., ... & Lyssiotis, C. A. (2025). Aspartate transaminases are required for blood development. *bioRxiv*, 2025-09.

2.7 Figures and Tables

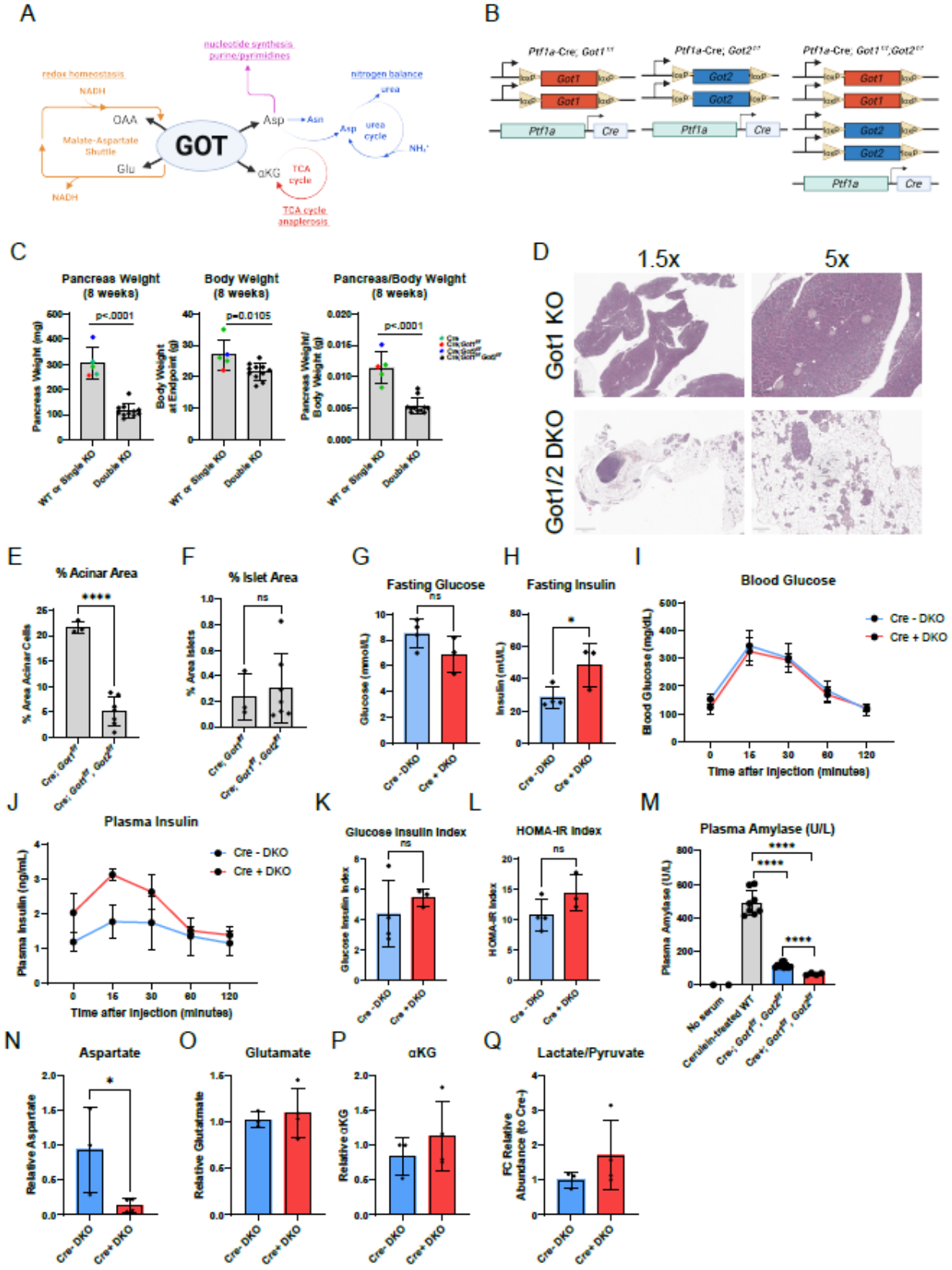


Figure 2-1 Mouse pancreatic functions are maintained without Got1 or Got2.

A, Scheme of the glutamate-oxaloacetate transaminases (GOTs) and their roles in cellular metabolism. OAA=oxaloacetate, Asp=aspartate, Glu=glutamine, αKG=α-ketoglutarate, Asn=asparagine. **B,** Scheme of alleles used for *Got* knockout pancreata. *Got1* and/or *Got2* deletion driven by epithelial pancreas-specific Cre recombinase (p48-Cre) on an immunocompetent (C57B/6) background. **C,** Pancreas and body weight of *Ptf1a-Cre*;*Got1*$^{f/f}$*;Got2*$^{f/f}$ double knockout (n=11) mice compared to controls. Controls include 8-week old single KO (n=5) or wild type (WT) mice, as indicated by colored circles. **D,** Representative hematoxylin and eosin (H&E) staining of pancreata from 8-week old Got1 KO and Got1/Got2 knockout mice. Scale bar is 800μm for 1.5x and 200μm for 5x. **E,** Percent acinar and **F,** islet area calculated from H&E images of 8-week old *Ptf1a-Cre*;*Got1*$^{f/f}$ (n=3) or *Ptf1a-Cre*;*Got1*$^{f/f}$*;Got2*$^{f/f}$ mice (n=7) mice. **G,** Fasting glucose and **H,** insulin after 5 hour fast in *Got1*$^{f/f}$*;Got2*$^{f/f}$ (n=4) or *Ptf1a-Cre*;*Got1*$^{f/f}$*;Got2*$^{f/f}$ (n=3) female mice. **I,** Blood glucose and **J,** plasma insulin measurements after 1.5g/kg glucose bolus with plasma analysis at 0, 15, 30, 60, and 120 minutes for *Got1*$^{f/f}$*;Got2*$^{f/f}$ (n=4) or *Ptf1a-Cre*;*Got1*$^{f/f}$*;Got2*$^{f/f}$ (n=3) female mice. **K,** Glucose-insulin index and **L,** HOMA-IR index of *Got1*$^{f/f}$*;Got2*$^{f/f}$ (n=4) or *Ptf1a-Cre*;*Got1*$^{f/f}$*;Got2*$^{f/f}$ (n=3) female mice. **M,** Plasma amylase for no serum controls, cerulein-treated wildtype mice (positive controls, n=4), Cre negative *Got1*$^{f/f}$*;Got2*$^{f/f}$ mice (n=5) or *Ptf1a-Cre*;*Got1*$^{f/f}$*;Got2*$^{f/f}$ double knockout mice (n=2). **N-Q,** Relative metabolite abundance, reported as fold change (FC) relative to control, as determined by LC-MS/MS in pancreata of 8-week old *Got1*$^{f/f}$*;Got2*$^{f/f}$ (n=3) or *Ptf1a-Cre*;*Got1*$^{f/f}$*;Got2*$^{f/f}$ (n=4) mice. **N,** aspartate, **O,** glutamate, **P**, α-ketoglutarate (αKG), and **Q**, lactate/pyruvate..

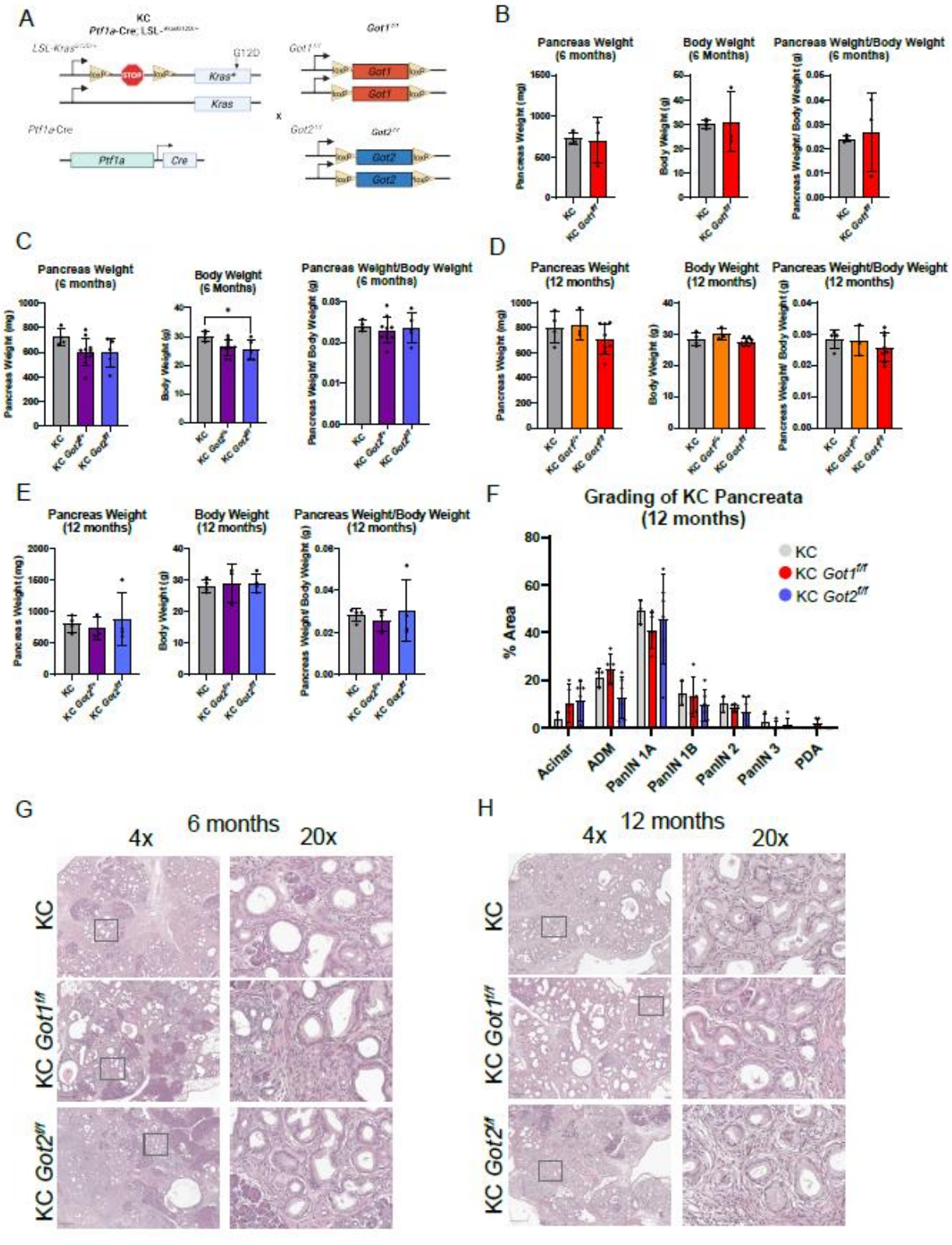

A
KC
Ptf1a-Cre; LSL-
LSL-Kras
G12D
STOP
loxP
Kras+
Kras
Ptf1a-Cre
Ptf1a
Cre
x
Got1
Got2
B
Pancreas Weight (6 months)
Body Weight (6 Months)
Pancreas Weight/Body Weight (6 months)
Pancreas Weight (mg)
Body Weight (g)
KC
KC Got1f/f
C
Pancreas Weight (6 months)
Body Weight (6 Months)
Pancreas Weight/Body Weight (6 months)
KC Got2f/f
D
Pancreas Weight (12 months)
Body Weight (12 months)
Pancreas Weight/Body Weight (12 months)
E
Pancreas Weight (12 months)
Body Weight (12 months)
Pancreas Weight/Body Weight (12 months)
F
Grading of KC Pancreata (12 months)
% Area
KC
KC Got1f/f
KC Got2f/f
Acinar
ADM
PanIN 1A
PanIN 1B
PanIN 2
PanIN 3
PDA
G
6 months
4x
20x
KC
KC Got1f/f
KC Got2f/f
H
12 months
4x
20x
KC
KC Got1f/f
KC Got2f/f

Figure 2-2 Knockout of pancreatic Got1 or Got2 does not impact precancerous lesion formation.

A, Scheme of alleles used to study Got in pancreatic precancerous lesions. Got1 or Got2 deletion with expression of mutant Kras (LSL-*Kras*^{G12D}) driven by epithelial pancreas-specific Cre recombinase (*p48*-Cre) on an immunocompetent (C57B/6) background (KC-Got1 and KC-Got2). **B,** Pancreas and body weight of KC (n=4) and KC;*Got1*$^{f/f}$ (n=3) mice aged to 6 months. **C,** Pancreas and body weight of KC (n=4), KC;*Got2*$^{f/+}$ (n=10), and KC;*Got2*$^{f/f}$ (n=5) mice aged to 6 months. **D,** Pancreas and body weight of KC (n=4), KC;*Got1* $^{f/+}$ KC (n=3);*Got1*$^{f/f}$ (n=8) mice aged to 12 months. **E,** Pancreas and body weight of KC (n=4), KC;*Got2*$^{f/+}$ (n=3), and KC;*Got2*$^{f/f}$ (n=4) mice aged to 12 months. **F,** Histological grading of pancreata of KC (n=3), KC;*Got1*$^{f/f}$ (n=5), and KC;*Got2*$^{f/f}$ (n=5) mice aged to 12 months. **G,** Representative hematoxylin and eosin (H&E) staining of pancreata from 6- and **H,** 12-month aged KC mice. Scale bar is 250μm for 4x and 50μm for 20x images.

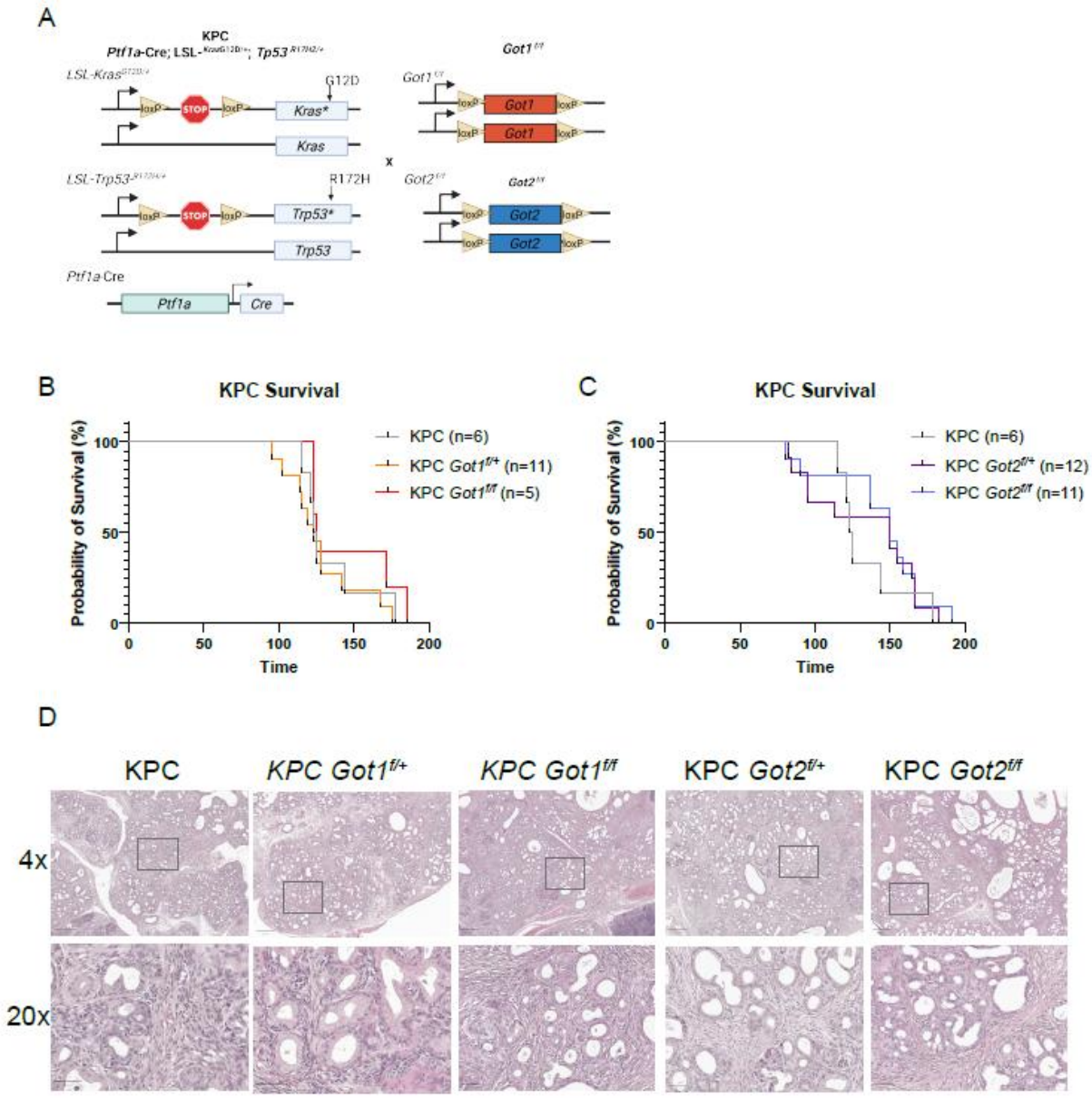


Figure 2-3 Loss of Got1 or Got2 does not improve survival in genetically engineered models of pancreatic cancer.

A, Scheme of alleles used to study Got in pancreatic cancer. Got1 or Got2 deletion with expression of mutant Kras (LSL-*Kras*^{G12D}) and mutant p53 (LSL-*Tp53* $^{R17H2/+}$) driven by epithelial pancreas-specific Cre recombinase (*p48*-Cre) on an immunocompetent (C57B/6) background (KPC-Got1 and KPC-Got2). **B,** Kaplan-Meier survival curves for overall survival of KPC (n=6), KPC;*Got1*$^{f/+}$ (n=11), and KPC;*Got1*$^{f/f}$ (n=5) mice. **C,** Kaplan-Meier survival curves for overall survival of KPC (n=6), KPC;*Got2*$^{f/+}$ (n=12), and KPC;*Got2*$^{f/f}$ (n=11) mice. **D,** Representative hematoxylin and eosin (H&E) staining of pancreata from KPC mice. Scale bar is 250μm for 4x and 50μm for 20x images.

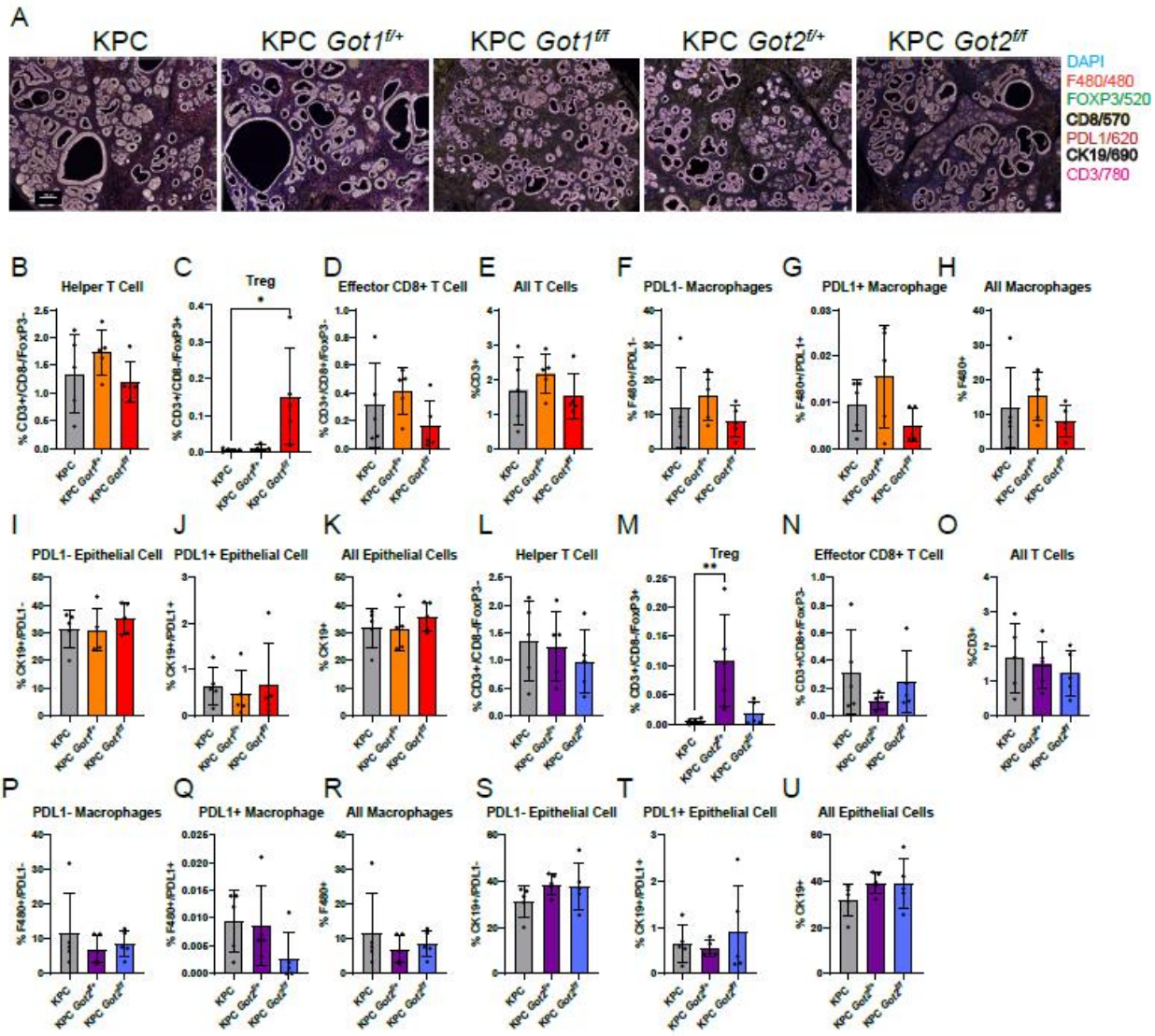


Figure 2-4 Got1 or Got2 loss does not alter the composition of immune and epithelial compartments in the tumor microenvironment.

A, Representative multiplex IF images of KPC, KPC;*Got1*$^{f/+}$, KPC;*Got1*$^{f/f}$, KPC;*Got2*$^{f/+}$, and KPC;*Got2*$^{f/f}$ mice. Scale bar is 100μm. **B, C, D, E,** T cell populations identified by multiplex IF of KPC, KPC;*Got1*$^{f/+}$, and KPC;*Got1*$^{f/f}$ mice (n=5 per group). **F, G, H,** Macrophage populations identified by multiplex IF of KPC, KPC;*Got1*$^{f/+}$, and KPC;*Got1*$^{f/f}$ mice (n=5 per group). **I, J, K,** Epithelial cell populations identified by multiplex IF of KPC, KPC;*Got1*$^{f/+}$, and KPC;*Got1*$^{f/f}$ mice (n=5 per group). **L, M, N, O,** T cell populations identified by multiplex IF of KPC, KPC;*Got2*$^{f/+}$, and KPC;*Got2*$^{f/f}$ mice (n=5 per group). **P, Q, R,** Macrophage populations identified by multiplex IF of KPC, KPC;*Got2*$^{f/+}$, and KPC;*Got2*$^{f/f}$ mice (n=5 per group). **S, T, U,** Epithelial cell populations identified by multiplex IF of KPC, KPC;*Got2*$^{f/+}$, and KPC;*Got2*$^{f/f}$ mice (n=5 per group).

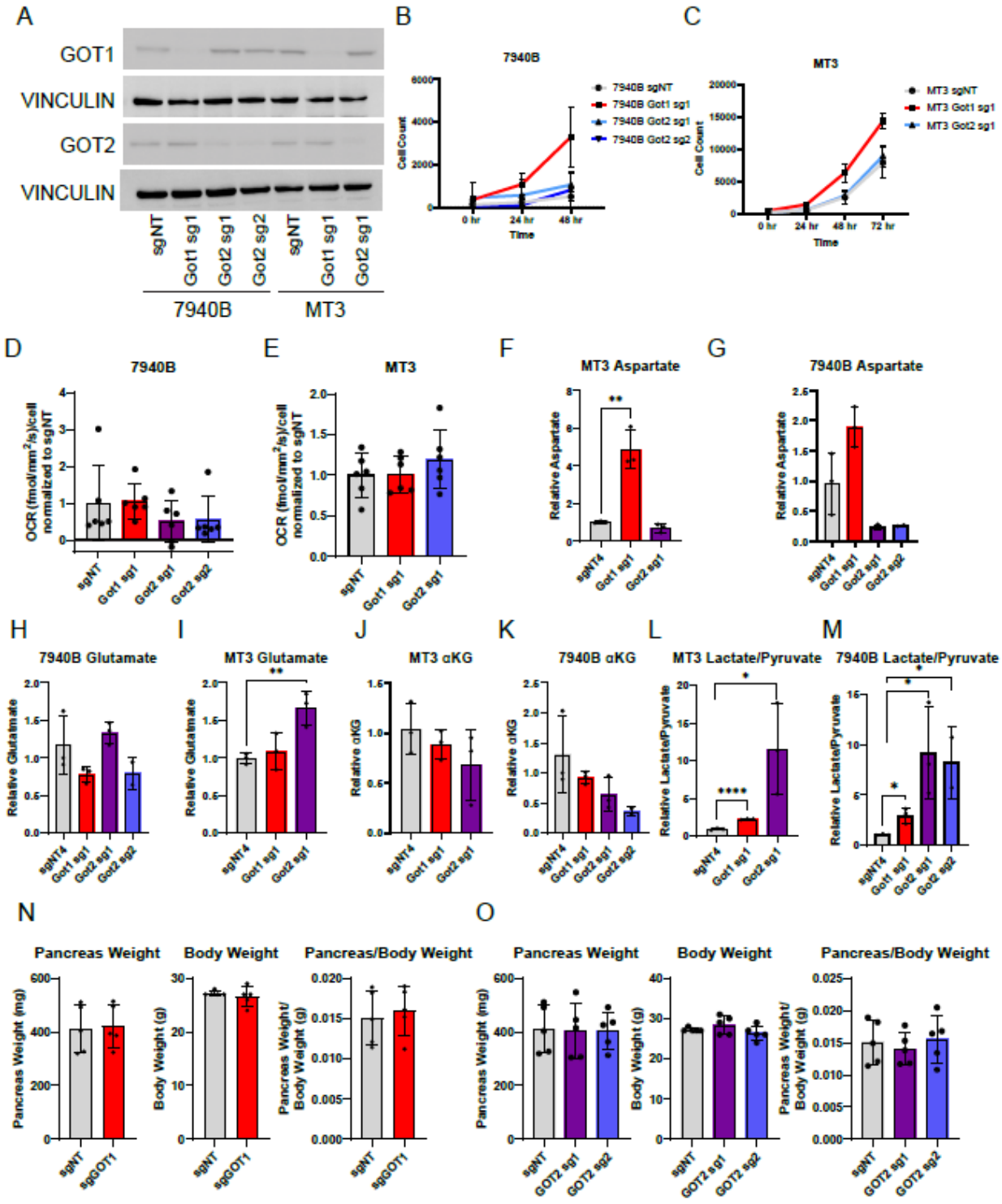

A
GOT1
VINCULIN
GOT2
VINCULIN
sgNT
Got1 sg1
Got2 sg1
Got2 sg2
sgNT
Got1 sg1
Got2 sg1
7940B
MT3
B
7940B
Cell Count
Time
0 hr
24 hr
48 hr
7940B sgNT
7940B Got1 sg1
7940B Got2 sg1
7940B Got2 sg2
C
MT3
Cell Count
Time
0 hr
24 hr
48 hr
72 hr
MT3 sgNT
MT3 Got1 sg1
MT3 Got2 sg1
D
7940B
OCR (fmol/mm²/s)/cell normalized to sgNT
sgNT
Got1 sg1
Got2 sg1
Got2 sg2
E
MT3
OCR (fmol/mm²/s)/cell normalized to sgNT
sgNT
Got1 sg1
Got2 sg1
F
MT3 Aspartate
Relative Aspartate
**
sgNT4
Got1 sg1
Got2 sg1
G
7940B Aspartate
Relative Aspartate
sgNT4
Got1 sg1
Got2 sg1
Got2 sg2
H
7940B Glutamate
Relative Glutamate
sgNT4
Got1 sg1
Got2 sg1
Got2 sg2
I
MT3 Glutamate
Relative Glutamate
**
sgNT4
Got1 sg1
Got2 sg1
J
MT3 αKG
Relative αKG
sgNT4
Got1 sg1
Got2 sg1
K
7940B αKG
Relative αKG
sgNT4
Got1 sg1
Got2 sg1
Got2 sg2
L
MT3 Lactate/Pyruvate
Relative Lactate/Pyruvate
*
****
sgNT4
Got1 sg1
Got2 sg1
M
7940B Lactate/Pyruvate
Relative Lactate/Pyruvate
*
*
*
sgNT4
Got1 sg1
Got2 sg1
Got2 sg2
N
Pancreas Weight
Pancreas Weight (mg)
sgNT
sgGOT1
Body Weight
Body Weight (g)
sgNT
sgGOT1
Pancreas/Body Weight
Pancreas Weight/ Body Weight (g)
sgNT
sgGOT1
O
Pancreas Weight
Pancreas Weight (mg)
sgNT
GOT2 sg1
GOT2 sg2
Body Weight
Body Weight (g)
sgNT
GOT2 sg1
GOT2 sg2
Pancreas/Body Weight
Pancreas Weight/ Body Weight (g)
sgNT
GOT2 sg1
GOT2 sg2

Figure 2-5 PDAC cells adapt their metabolism to counter GOT loss.

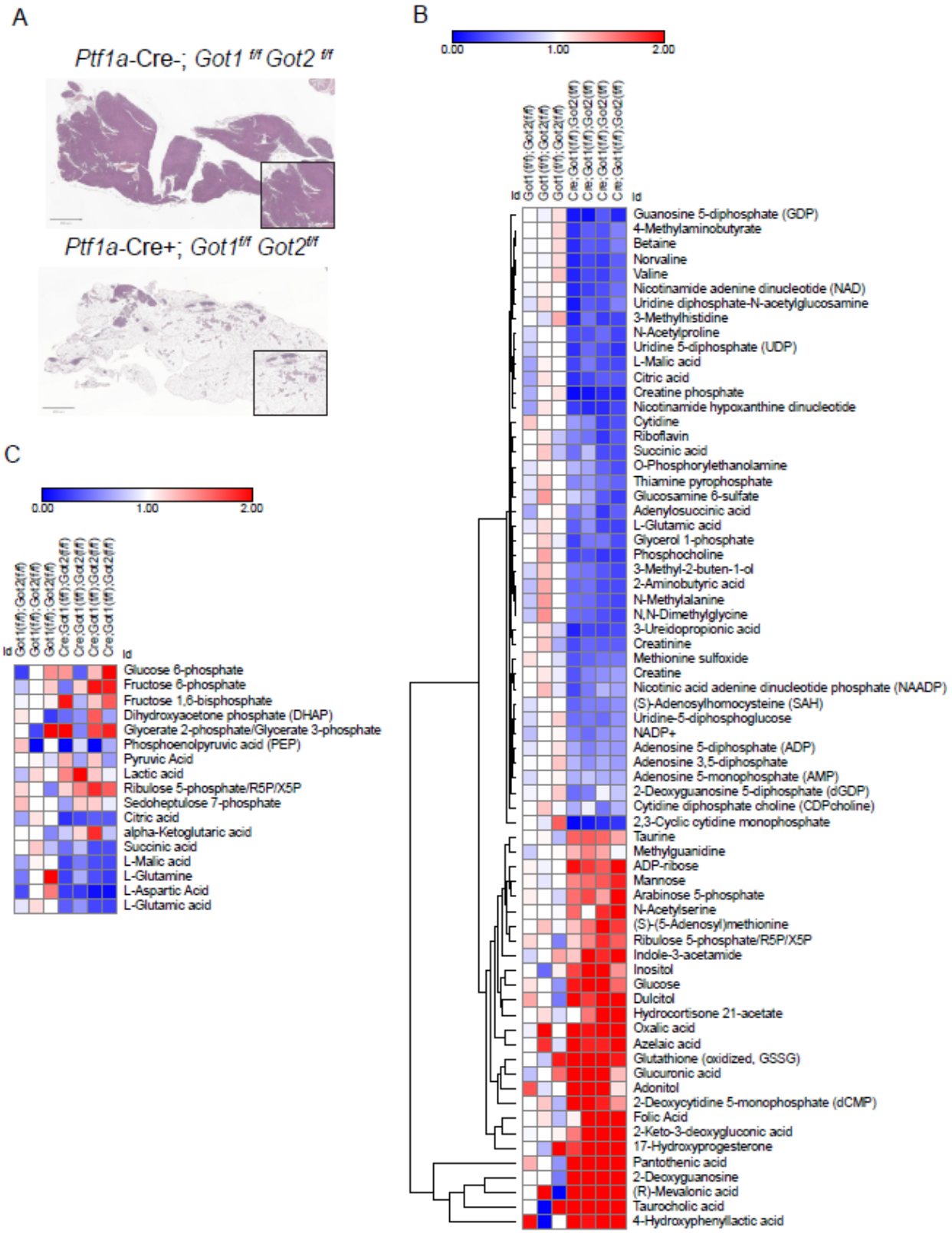
A, Western blot analysis of murine KPC pancreatic cancer cell lines (7940B and MT3) stably expressing a non-targeting sgRNA (sgNT) or with Got1 or Got2 KO. Two independent sgRNAs against GOT2 are designated sg1 and sg2. **B,** Cell count of 7940B and MT3 cell lines with Got1 or Got2 KO over 48-72 hours. Each clone plated with 5-10 replicates. **C,D,** Oxygen consumption rate (fmol/mm^2/s) of 7940B and MT3 cell lines with Got1 or Got2 KO normalized to cell number. Each clone plated with 6 replicates. **F-M**, Relative intracellular metabolite abundance, reported as fold change (FC), as determined by LC-MS/MS in MT3 and 7940B murine KPC cells. **F,G** aspartate, **H,I,** glutamate, **J,K**, α-KG (α-ketoglutarate), **L,M**, lactate/pyruvate. **N,O,** Pancreas and body weight of mice at endpoint after orthotopic implantation of pancreatic cancer cells (n=5 per group).

sgNT	ACTATTTAATATTGGTAAGT
Got1sg1 5’—3’	GATAGGCTGAGTCAAAGAAG
Got2sg1 5’—3’	TGGACCCGCGTCCCGAGCAG
Got2sg2 5’—3’	TGGAGGTCCCATTTCAACAT

Table 2-1 sgRNA Sequences.

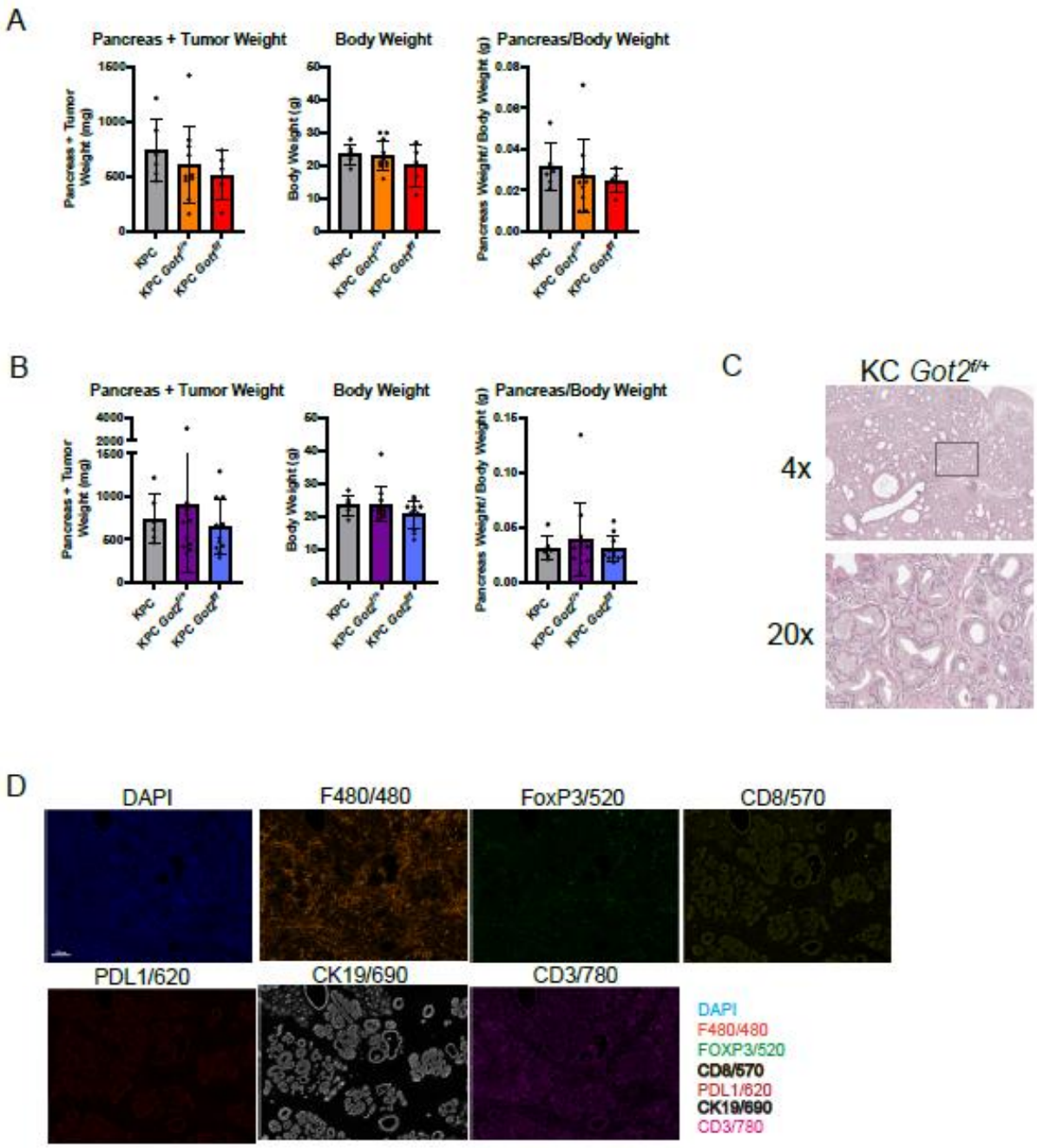
Gene	Primer Sequence
Got1 WT - F	CGTGGAAGATGTAACCTATCCCTG
Got1 WT - R	GGCTTGCCATTGAGTTATACTAGG
Got1 floxed - F	ACTGGTGACTGAGCAGGGACTTC
Got1 floxed - R	CTTAAGTGTATGAGTTCCTCAAACCATTGC
Got2 WT -F	CAGCTAGGATGTGGAACCTGAG
Got2 WT - R	AATGGAACTAAGAGTAGCTGCACC
Got2 floxed - F	GCAGATTAAAACCACAAGGCCTGTA
Got2 floxed - R	ATGTTAAAATTGTCATCCCCTGTGC
Ptf1a-Cre – F	TCGCGATTATCTTCTATATCTTCAG
Ptf1a-Cre - R	GCTCGACCAGTTTAGTTACCC
LSL-P53R172H p53 WT	TTACACATCCAGCCTCTGTGG
LSL-P53R172H p53 5’	AGCTAGCCACCATGGCTTGAGTAAGTCT
LSL-P53R172H p53 3’	CTTGGAGACATAGCCACACTG
LSL KRASG12D - F1	CACCAGCTTCGGCTTCCTATT
LSL KRASG12D - F2	AGCTAATGGCTCTCAAAGGAATGTA
LSL KRASG12D - R	CCATGGCTTGAGTAAGTCTGC

Table 2-2 PCR Primers for Genotyping


A
Ptf1a-Cre-; Got1 f/f Got2 f/f
Ptf1a-Cre+; Got1f/f Got2f/f
B
0.00
1.00
2.00
Id
Got1(f/f);Got2(f/f)
Got1(f/f);Got2(f/f)
Got1(f/f);Got2(f/f)
Cre;Got1(f/f);Got2(f/f)
Cre;Got1(f/f);Got2(f/f)
Cre;Got1(f/f);Got2(f/f)
Cre;Got1(f/f);Got2(f/f)
Guanosine 5-diphosphate (GDP)
4-Methylaminobutyrate
Betaine
Norvaline
Valine
Nicotinamide adenine dinucleotide (NAD)
Uridine diphosphate-N-acetylglucosamine
3-Methylhistidine
N-Acetylproline
Uridine 5-diphosphate (UDP)
L-Malic acid
Citric acid
Creatine phosphate
Nicotinamide hypoxanthine dinucleotide
Cytidine
Riboflavin
Succinic acid
O-Phosphorylethanolamine
Thiamine pyrophosphate
Glucosamine 6-sulfate
Adenylosuccinic acid
L-Glutamic acid
Glycerol 1-phosphate
Phosphocholine
3-Methyl-2-buten-1-ol
2-Aminobutyric acid
N-Methylalanine
N,N-Dimethylglycine
3-Ureidopropionic acid
Creatinine
Methionine sulfoxide
Creatine
Nicotinic acid adenine dinucleotide phosphate (NAADP)
(S)-Adenosylhomocysteine (SAH)
Uridine-5-diphosphoglucose
NADP+
Adenosine 5-diphosphate (ADP)
Adenosine 3,5-diphosphate
Adenosine 5-monophosphate (AMP)
2-Deoxyguanosine 5-diphosphate (dGDP)
Cytidine diphosphate choline (CDPcholine)
2,3-Cyclic cytidine monophosphate
Taurine
Methylguanidine
ADP-ribose
Mannose
Arabinose 5-phosphate
N-Acetylserine
(S)-(5-Adenosyl)methionine
Ribulose 5-phosphate/R5P/X5P
Indole-3-acetamide
Inositol
Glucose
Dulcitol
Hydrocortisone 21-acetate
Oxalic acid
Azelaic acid
Glutathione (oxidized, GSSG)
Glucuronic acid
Adonitol
2-Deoxycytidine 5-monophosphate (dCMP)
Folic Acid
2-Keto-3-deoxygluconic acid
17-Hydroxyprogesterone
Pantothenic acid
2-Deoxyguanosine
(R)-Mevalonic acid
Taurocholic acid
4-Hydroxyphenyllactic acid
C
0.00
1.00
2.00
Id
Got1(f/f);Got2(f/f)
Got1(f/f);Got2(f/f)
Got1(f/f);Got2(f/f)
Cre;Got1(f/f);Got2(f/f)
Cre;Got1(f/f);Got2(f/f)
Cre;Got1(f/f);Got2(f/f)
Cre;Got1(f/f);Got2(f/f)
Glucose 6-phosphate
Fructose 6-phosphate
Fructose 1,6-bisphosphate
Dihydroxyacetone phosphate (DHAP)
Glycerate 2-phosphate/Glycerate 3-phosphate
Phosphoenolpyruvic acid (PEP)
Pyruvic Acid
Lactic acid
Ribulose 5-phosphate/R5P/X5P
Sedoheptulose 7-phosphate
Citric acid
alpha-Ketoglutaric acid
Succinic acid
L-Malic acid
L-Glutamine
L-Aspartic Acid
L-Glutamic acid

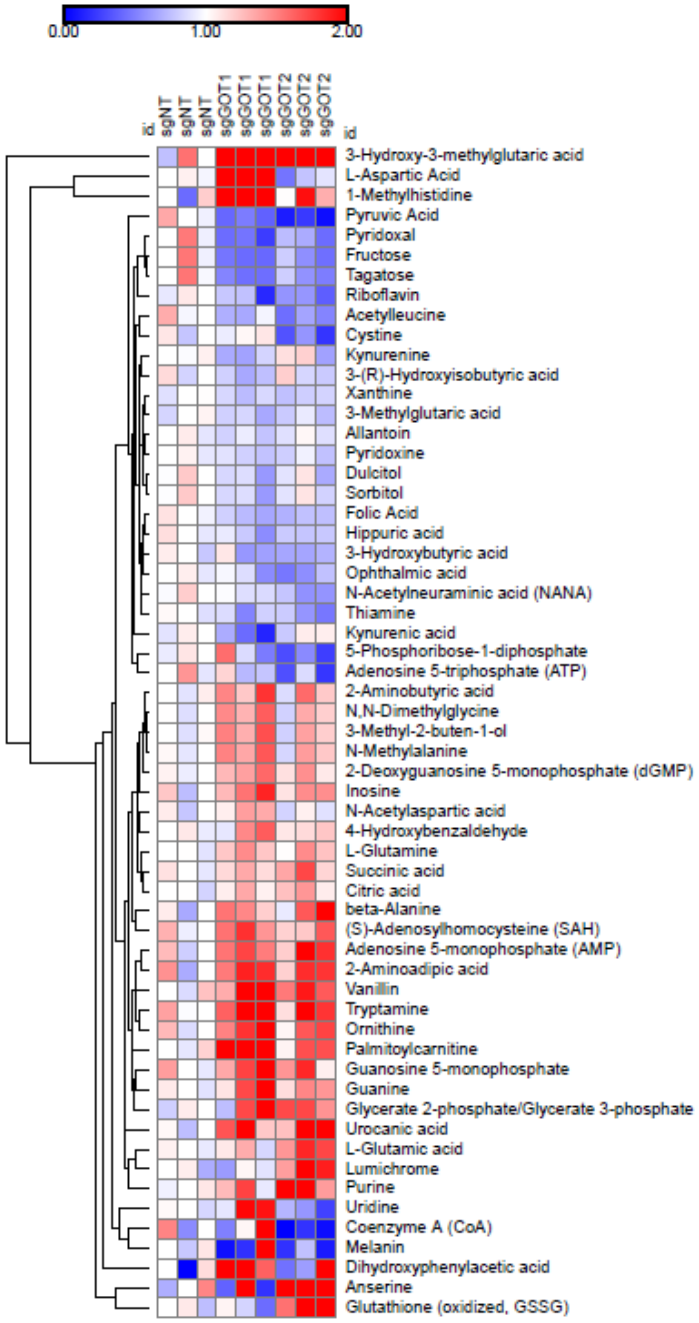
Supplementary Figure 2-1

A, Representative hematoxylin and eosin (H&E) staining of *Got1*$^{f/f}$*;Got2*$^{f/f}$ (Cre negative) and *Ptf1a-Cre*;*Got1*$^{f/f}$*;Got2*$^{f/f}$ pancreata. Scale bar is 800μm. **B,** Unsupervised hierarchical clustering of differentially abundant metabolites ($p<0.1$, compared to Cre negative mice) in pancreata of 8-week old *Got1*$^{f/f}$*;Got2*$^{f/f}$ (n=3) or *Ptf1a-Cre*;*Got1*$^{f/f}$*;Got2*$^{f/f}$ (n=4) mice, as measured by LC-MS/MS. **C,** Curated list of glycolytic, pentose phosphate, and TCA cycle intermediate metabolites from the dataset generated in **B**.



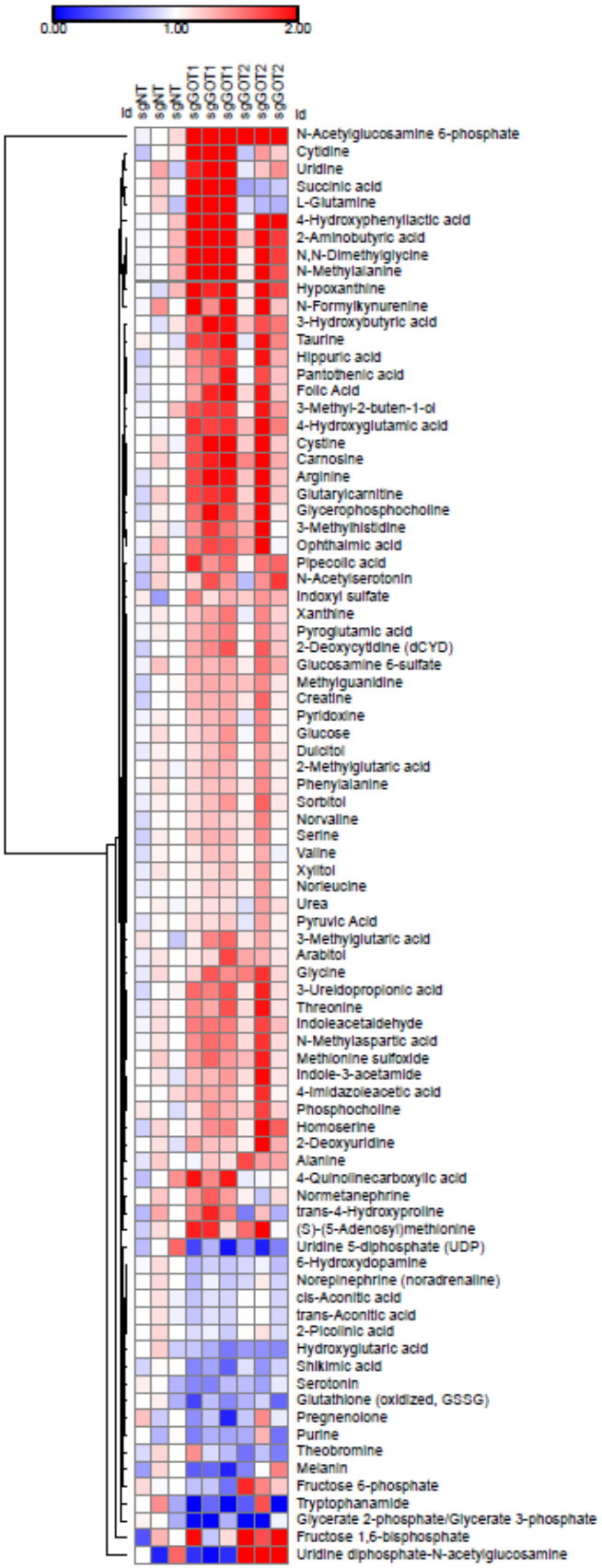
Supplementary Figure 2-2

A, Tumor and body weight of KPC (n=6), KPC;*Got1*$^{f/+}$ (n=11), and KPC;*Got1*$^{f/f}$ (n=5) mice. **B,** Tumor and body weight of KPC (n=6), KPC;*Got2*$^{f/+}$ (n=12), and KPC;*Got2*$^{f/f}$ (n=11) mice. **C,** Representative hematoxylin and eosin (H&E) staining of 12-month-aged KC; *Got2*$^{f/+}$ pancreata. Scale bar is 100μm. **D,** Individual immunofluorescence panels for multiplex IF. Scale bar is 250μm for 4x and 50μm for 20x images.



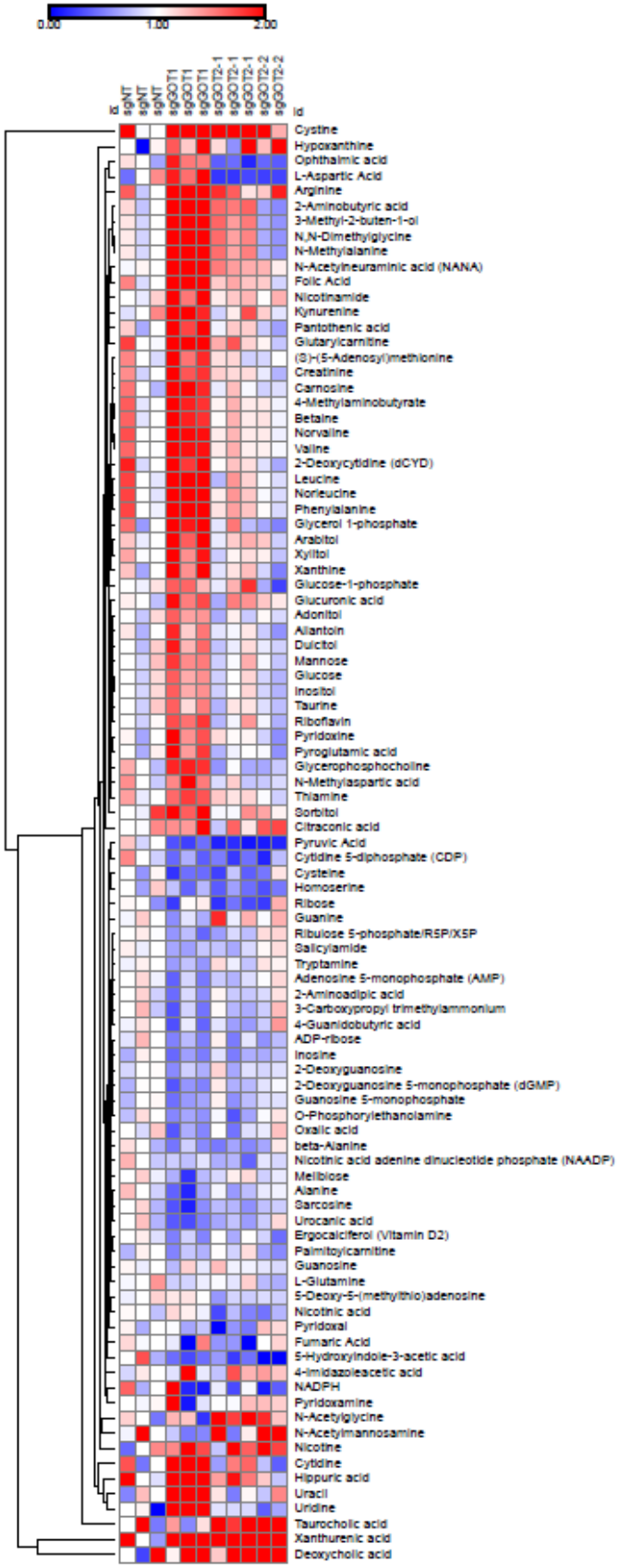
Supplementary Figure 2-3

Unsupervised hierarchical clustering of differentially abundant intracellular metabolites ($p<0.1$, compared to sgNT) from MT3 cells with *Got1* or *Got2* knockout as measured by LC-MS/MS. n=3 biologically independent samples per group.


0.00
1.00
2.00
Id
sgNT
sgNT
sgNT
sgGOT1
sgGOT1
sgGOT1
sgGOT2
sgGOT2
sgGOT2
Id
N-Acetylglucosamine 6-phosphate
Cytidine
Uridine
Succinic acid
L-Glutamine
4-Hydroxyphenyllactic acid
2-Aminobutyric acid
N,N-Dimethylglycine
N-Methylalanine
Hypoxanthine
N-Formylkynurenine
3-Hydroxybutyric acid
Taurine
Hippuric acid
Pantothenic acid
Folic Acid
3-Methyl-2-buten-1-ol
4-Hydroxyglutamic acid
Cystine
Carnosine
Arginine
Glutarylcarnitine
Glycerophosphocholine
3-Methylhistidine
Ophthalmic acid
Pipecolic acid
N-Acetylserotonin
Indoxyl sulfate
Xanthine
Pyroglutamic acid
2-Deoxycytidine (dCYD)
Glucosamine 6-sulfate
Methylguanidine
Creatine
Pyridoxine
Glucose
Dulcitol
2-Methylglutaric acid
Phenylalanine
Sorbitol
Norvaline
Serine
Valine
Xylitol
Norleucine
Urea
Pyruvic Acid
3-Methylglutaric acid
Arabitol
Glycine
3-Ureidopropionic acid
Threonine
Indoleacetaldehyde
N-Methylaspartic acid
Methionine sulfoxide
Indole-3-acetamide
4-Imidazoleacetic acid
Phosphocholine
Homoserine
2-Deoxyuridine
Alanine
4-Quinolinecarboxylic acid
Normetanephrine
trans-4-Hydroxyproline
(S)-(5-Adenosyl)methionine
Uridine 5-diphosphate (UDP)
6-Hydroxydopamine
Norepinephrine (noradrenaline)
cis-Aconitic acid
trans-Aconitic acid
2-Picolinic acid
Hydroxyglutaric acid
Shikimic acid
Serotonin
Glutathione (oxidized, GSSG)
Pregnenolone
Purine
Theobromine
Melanin
Fructose 6-phosphate
Tryptophanamide
Glycerate 2-phosphate/Glycerate 3-phosphate
Fructose 1,6-bisphosphate
Uridine diphosphate-N-acetylglucosamine

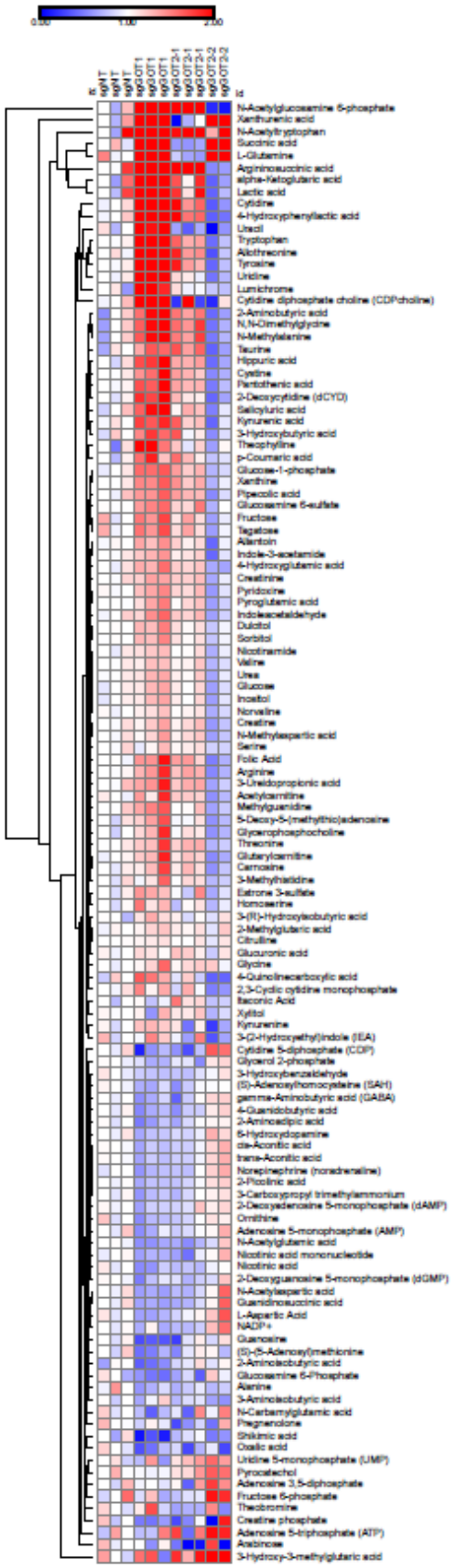
Supplementary Figure 2-4

Unsupervised hierarchical clustering of differentially abundant extracellular metabolites ($p<0.1$, compared to sgNT) from MT3 cells with *Got1* or *Got2* knockout as measured by LC-MS/MS. n=3 biologically independent samples per group.


0.00
1.00
2.00
Id
sgNT
sgNT
sgNT
sgGOT1
sgGOT1
sgGOT2-1
sgGOT2-1
sgGOT2-1
sgGOT2-2
sgGOT2-2
Cystine
Hypoxanthine
Ophthalmic acid
L-Aspartic Acid
Arginine
2-Aminobutyric acid
3-Methyl-2-buten-1-ol
N,N-Dimethylglycine
N-Methylalanine
N-Acetylneuraminic acid (NANA)
Folic Acid
Nicotinamide
Kynurenine
Pantothenic acid
Glutarylcarnitine
(S)-(5-Adenosyl)methionine
Creatinine
Carnosine
4-Methylaminobutyrate
Betaine
Norvaline
Valine
2-Deoxycytidine (dCYD)
Leucine
Norleucine
Phenylalanine
Glycerol 1-phosphate
Arabitol
Xylitol
Xanthine
Glucose-1-phosphate
Glucuronic acid
Adonitol
Allantoin
Dulcitol
Mannose
Glucose
Inositol
Taurine
Riboflavin
Pyridoxine
Pyroglutamic acid
Glycerophosphocholine
N-Methylaspartic acid
Thiamine
Sorbitol
Citraconic acid
Pyruvic Acid
Cytidine 5-diphosphate (CDP)
Cysteine
Homoserine
Ribose
Guanine
Ribulose 5-phosphate/RSP/X5P
Salicylamide
Tryptamine
Adenosine 5-monophosphate (AMP)
2-Aminoadipic acid
3-Carboxypropyl trimethylammonium
4-Guanidobutyric acid
ADP-ribose
Inosine
2-Deoxyguanosine
2-Deoxyguanosine 5-monophosphate (dGMP)
Guanosine 5-monophosphate
O-Phosphorylethanolamine
Oxalic acid
beta-Alanine
Nicotinic acid adenine dinucleotide phosphate (NAADP)
Melibiose
Alanine
Sarcosine
Urocanic acid
Ergocalciferol (Vitamin D2)
Palmitoylcarnitine
Guanosine
L-Glutamine
5-Deoxy-5-(methylthio)adenosine
Nicotinic acid
Pyridoxal
Fumaric Acid
5-Hydroxyindole-3-acetic acid
4-Imidazoleacetic acid
NADPH
Pyridoxamine
N-Acetylglycine
N-Acetylmannosamine
Nicotine
Cytidine
Hippuric acid
Uracil
Uridine
Taurocholic acid
Xanthurenic acid
Deoxycholic acid

Supplementary Figure 2-5

Unsupervised hierarchical clustering of differentially abundant intracellular metabolites ($p<0.1$, compared to sgNT) from 7940B cells with *Got1* or *Got2* knockout as measured by LC-MS/MS. n=3 biologically independent samples per group; n=2 for Got2 sg2.


0.50
1.00
2.00
n
sgn1-T
sgn1-T
sgn1-T
sg2-OT-1
sg2-OT-1
sg2-OT-1
sg2-OT2-1
sg2-OT2-1
sg2-OT2-1
sg2-OT2-2
sg2-OT2-2
sg2-OT2-2
Id
N-Acetylglucosamine 6-phosphate
Xanthurenic acid
N-Acetyltryptophan
Succinic acid
L-Glutamine
Argininosuccinic acid
alpha-Ketoglutaric acid
Lactic acid
Cytidine
4-Hydroxyphenyllactic acid
Uracil
Tryptophan
Allothreonine
Tyrosine
Uridine
Lumichrome
Cytidine diphosphate choline (CDPcholine)
2-Aminobutyric acid
N,N-Dimethylglycine
N-Methylalanine
Taurine
Hippuric acid
Cystine
Pantothenic acid
2-Deoxycytidine (dCYD)
Salicyluric acid
Kynurenic acid
3-Hydroxybutyric acid
Theophylline
p-Coumaric acid
Glucose-1-phosphate
Xanthine
Pipecolic acid
Glucosamine 6-sulfate
Fructose
Tagatose
Allantoin
Indole-3-acetamide
4-Hydroxyglutamic acid
Creatinine
Pyridoxine
Pyroglutamic acid
Indoleacetaldehyde
Dulcitol
Sorbitol
Nicotinamide
Valine
Urea
Glucose
Inositol
Norvaline
Creatine
N-Methylaspartic acid
Serine
Folic Acid
Arginine
3-Ureidopropionic acid
Acetylcarnitine
Methylguanidine
5-Deoxy-5-(methylthio)adenosine
Glycerophosphocholine
Threonine
Glutarylcarnitine
Carnosine
3-Methylhistidine
Estrone 3-sulfate
Homoserine
3-(R)-Hydroxybutyric acid
2-Methylglutaric acid
Citrulline
Glucuronic acid
Glycine
4-Quinolinecarboxylic acid
2,3-Cyclic cytidine monophosphate
Itaconic Acid
Xylitol
Kynurenine
3-(2-Hydroxyethyl)indole (IEA)
Cytidine 5-diphosphate (CDP)
Glycerol 2-phosphate
3-Hydroxybenzaldehyde
(S)-Adenosylhomocysteine (SAH)
gamma-Aminobutyric acid (GABA)
4-Guanidobutyric acid
2-Aminoadipic acid
6-Hydroxydopamine
cis-Aconitic acid
trans-Aconitic acid
Norepinephrine (noradrenaline)
2-Picolinic acid
3-Carboxypropyl trimethylammonium
2-Deoxyadenosine 5-monophosphate (dAMP)
Ornithine
Adenosine 5-monophosphate (AMP)
N-Acetylglutamic acid
Nicotinic acid mononucleotide
Nicotinic acid
2-Deoxyguanosine 5-monophosphate (dGMP)
N-Acetylaspartic acid
Guanidinosuccinic acid
L-Aspartic Acid
NADP+
Guanosine
(S)-(5-Adenosyl)methionine
2-Aminobutyric acid
Glucosamine 6-Phosphate
Alanine
3-Aminoisobutyric acid
N-Carbamylglutamic acid
Pregnenolone
Shikimic acid
Oxalic acid
Uridine 5-monophosphate (UMP)
Pyrocatechol
Adenosine 3,5-diphosphate
Fructose 6-phosphate
Theobromine
Creatine phosphate
Adenosine 5-triphosphate (ATP)
Arabinose
3-Hydroxy-3-methylglutaric acid

Supplementary Figure 2-6

Unsupervised hierarchical clustering of differentially abundant extracellular metabolites ($p<0.1$, compared to sgNT) from 7940B cells with *Got1* or *Got2* knockout as measured by LC-MS/MS. n=3 biologically independent samples per group; n=2 for Got2 sg2.

Chapter 3: Selective and Targeted Molecular MRI of Pancreatic Cancer Using a Polyethylene Glycol Nanopolymer

3.1 Abstract

Development of novel, targeted molecular imaging agents for oncology is critical to overcoming the limitations of current clinical standards, which often lack molecular specificity and raise long-term safety concerns. This paper introduces a new paradigm for cancer imaging that circumvents these challenges. To develop and validate a selective, gadolinium-free, quantitative magnetic resonance (MR) molecular imaging agent using a polyethylene glycol (PEG) nanopolymer. The agent's selective delivery to pancreatic cancer was mediated in a mouse model by the co-administered, tumor-penetrating peptide iRGD. The MR sensitivity and quantitative linearity of the PEG agent were established using controlled phantoms. Subsequently, *in vivo* validation was performed in an orthotopic pancreatic cancer (KPC) mouse model. Imaging was conducted using a diffusion-weighted (DW), T2-weighted (T2w), single-shot fast spin echo (FSE) sequence specifically optimized to leverage the unique MR properties of PEG for selective detection while suppressing endogenous signals. The PEG MRI signal is linear concentration with highly effective suppression of background signals from water and fat. In the preclinical model, *in vivo* imaging revealed specific, high-contrast accumulation of PEG within pancreatic tumors following iRGD-mediated delivery. This resulted in "PET-like" molecular images that unambiguously delineated the tumor mass from surrounding healthy tissue. Targeted PEG MR imaging represents

a new method for high-contrast, specific cancer detection. This innovative approach successfully combines the molecular specificity characteristic of positron emission tomography (PET) with the superior spatial resolution and safety profile of magnetic resonance imaging (MRI), offering a promising new tool for precision oncology.

3.2 Introduction

Pancreatic ducal adenocarcinoma (PDAC) is among the most lethal malignancies, marked by a persistently low 5-year survival rate, currently at approximately 8%. (1,2) These statistics stem largely from the fact that symptoms are often vague and non-specific (e.g. abdominal pain, weight loss, and general fatigue), which leads to delayed diagnosis. (3) Additionally, the lack of reliable and routine screening methods means that the disease is frequently discovered only after it has advanced to a late stage, when treatment options are limited. This combination of silent progression and diagnostic challenges contributes to PDAC's status as one of the deadliest forms of cancer worldwide.

In patients at high risk for PDAC, namely those with a significant familial history of pancreatic cancer or those with known pathogenic gene mutations (eg. *BRCA*, *PALB2*, *CDKN2A*, or *STK11*), screening is more routine. (4,5) In these individuals, endoscopic ultrasound and magnetic resonance cholangiopancreatography (MRCP) may be utilized to provide annual or semiannual surveillance, often starting as early as age 30. This routine surveillance often leads to a higher proportion of early-stage pancreatic cancer diagnosis, which in turn allows for earlier intervention with surgical resection, alongside adjuvant or neoadjuvant chemotherapy, and a 5-year survival rate surpassing 40% (2). While routine screening has merit in high-risk individuals, this is not

recommended for the general population. Intensified surveillance is not without its risks, as false positives can result in unnecessary medical procedures. (4,5)

Consequently, only 10-20% of patients with a new pancreatic cancer diagnosis are surgical candidates due to both the aforementioned challenges with early detection and the propensity of PDAC for early metastatic disease. (6) As such, novel diagnostic tools that provide detection of early-stage pancreatic cancer would represent an opportunity to increase the surgical candidate pool and potentially extend the lives of patients who would not otherwise be eligible for these interventions.

Magnetic resonance imaging (MRI) is a cornerstone of modern medical diagnostics, prized for its exceptional ability to visualize soft tissue anatomy, making it invaluable for the detection and characterization of solid tumors. (7) However, the utility of conventional MRI is often constrained by the non-specific enhancement of current contrast agents. Almost all MR contrast studies rely on gadolinium (Gd)-based contrast agents (GBCAs), which enhance the signal from water protons non-specifically via water proton relaxation enhancement. (8) In addition, there is growing concerns over long-term safety due to finding of Gd deposition in the brain and other tissues. (9-11) Furthermore, GBCAs lack true molecular specificity, providing contrast based on physiological proxies like blood flow rather than direct molecular targeting. (8) Based on this, a safer contrast agent would be a welcome alternative, particularly in a vulnerable population such as those being screened for PDAC.

Polyethylene glycol (PEG) has widespread and versatile use in the pharmaceutical industry, due to its biocompatibility, water solubility, and low toxicity. (12) Within the context of MRI, PEG has been used to prolong the circulation time of contrast

agents, but it has not traditionally been thought of as a contrast agent itself. (13-14) One study successfully imaged 13C-labeled PEG by employing multiple quantum filtering. This clever, though cumbersome, method provides selective images of PEG but requires synthesis of 13C PEG. (15)

PEG has unique MR properties that allow selective imaging without resorting to 13C labeling. First, the chemical shift of PEG is ~1 ppm upfield from water, allowing imaging by frequency selection. Second, the T2 of PEG protons is approximately 500 ms, much longer than most water protons in tissue. And finally, the diffusion constant of 10 or 20k PEG is two orders of magnitude smaller than water. Given the different frequency, long T2 and small diffusion constant, T2-weighted and diffusion weighted sequences can be employed to selectively image PEG (**Figure 1**). However, since PEG is not readily taken up by cancer cells, and would otherwise be excreted, the remaining hurdle would be to augment its tumor penetration and retention to be a useful MRI candidate. (16)

To this end, our laboratories have developed a magnetic resonance imaging (MRI) protocol that utilizes structured polyethylene glycol (PEG) combined with an internalizing arginine-glycine-aspartate (iRGD) peptide to enhance tumor imaging in a non-invasive manner. iRGD represents a viable solution due to its ability to enhance the delivery of drugs or nanoparticles into solid tumors. (17-18) As its name suggests, iRGD contains an RGD motif (Arg-Gly-Asp) that binds specifically to αvβ3 and αvβ5 integrins, which are overexpressed on tumor epithelial cells. (17-20) Once bound to the integrins, iRGD undergoes proteolytic cleavage, exposing the C-end Rule (CendR) motif, which then binds to neuropilin-1 (NRP-1), a receptor highly expressed on tumor cells. Binding

to NRP-1 triggers transcytosis of co-administered agents across the tumor endothelial cells and into the tumor microenvironment (**Figure 3-2**). (17-18) If administered at the same time as iRGD, this process would likely allow PEG to be taken up into the target tumor cells and allow for enhanced imaging.

The goal of this study was to evaluate the ability of PEG to be imaged via MRI and to determine whether the combination of PEG and iRGD administration would allow for reliable tumor imaging in a murine model of pancreatic cancer.

3.3 Methods

3.3.1 Study approvals and mouse model

All animal procedures were performed at the University of Michigan (protocol number PRO00011640) in compliance with the Institutional Animal Care and Use Committee guidelines. Eight-to-ten-week-old C57BL/6 mice (Jackson Laboratory) were used for all mouse experiments. The mice were housed in the vivaria at the Lurie Biomedical Engineering Building and the North Campus Research Complex and were monitored daily.

3.3.2 In vitro PEG imaging in phantoms

To estimate the sensitivity of PEG imaging and establish a linear relationship between concentration and signal, a phantom was constructed using PEG concentrations of 0, 0.05, 0.1, 0.5, 1.0, 3.0 and 5.0 mg/ml in 5 mm NMR glass tubes. The tubes were sealed, arranged in a hexagonal closest packing, placed in a 50 ml plastic centrifuge tube, and surrounded with 1.5% agarose to minimize susceptibility to artifacts. The phantom was imaged with a diffusion-weighted, fast-spin echo sequence with b value = 5000 s/mm^2 and TE = 240 ms.

3.3.3 Subcutaneous flank injection

Mice were anesthetized via isoflurane inhalation and received bilateral 200μL flank injections of a 1:1 mixture of Matrigel (Corning) and 8-PEG reconstituted in phosphate-buffered saline (PBS). The left flank received a PEG concentration of 2mg/mL and the right flank received a PEG concentration of 10mg/mL. The mice then immediately underwent MRI.

3.3.4 Orthotopic pancreas KPC cell injection

Immediately prior to the animal procedure, $5x10^4$ KPC cells per recipient mouse were prepared in a 1:1 mixture of Matrigel and DMEM. Mice were anesthetized via isoflurane inhalation and the left flank was prepared utilizing aseptic technique. A 5mm skin incision was made just posterior to the ribcage and an additional incision was made through the muscle layer overlying the spleen. The spleen was elevated through the muscle layer, exposing the attached pancreas. A 50μL injection of the prepared tumor cell suspension was injected directly into the pancreas using an insulin syringe. The organs were reapproximated within the cavity and the site was closed in layers. Tumors were allowed to grow for 18 days prior to our MRI procedure.

3.3.5 Tail vein injections of PEG and iRGD

Prior to undergoing MRI, mice in the orthotopic pancreatic tumor group were anesthetized and placed on a warming pad. PEG (MW = 40K, 400mg/kg) and iRGD (8mg/kg) are reconstituted in 200uL of PBS and co-administered via a lateral tail vein injection approximately 15 minutes prior to imaging.

3.3.6 MRI Protocol

Following the PEG-iRGD injection, the animals were placed in a 40mm Millipede MRI probe. Thermoregulation was provided by fiberoptic temperature measurement controlling warm air. Isoflurane (1.5%–2.0%) in 1 L/min oxygen (SurgiVet V704001, Smiths Medical, Waukesha, WI, USA) was used to induce and maintain general anesthesia and a respiratory rate of approximately 80 breaths/min. Mouse temperature during MRI acquisition was maintained at 36°C–37°C using an MR-compatible fiberoptic temperature module and an MR-compatible heater system for small animals (1025T monitoring and gating system, SA Instruments, Stony Brook, NY, USA). Selective imaging of the PEG component was performed with a DW, T2W, single-shot FSE sequence with a 35 mm FOV, 5mm ST, b=5200 s/mm2, TR/TE=2000/276 ms and 100 averages for a total imaging time of 3.3 minutes. The slow diffusion (D = 4.9 10-5 mm2/s) and long TE (550 ms) allows suppression of water and selective imaging of PEG. Long PEG T2 allows a single echo train with 64 echoes and narrow BW of 10 kHz to be used to further increase SNR.

3.4 Results

3.4.1 In vitro PEG imaging

PEG can be selectively imaged. The PEG signal was found to be linear with concentration and could be detected to 0.1 mg/ml in voxel sizes with in-plane resolution of 0.5 mm and voxel size of 1.5 ul. **(Figure 3-3)** Single-shot FSE was used with 100 averages to achieve sufficient SNR using parameters outlined above.

3.4.2 Subcutaneous in vivo PEG imaging

While selective PEG imaging was relatively straightforward in the phantom, the environment *in vivo* creates additional challenges. Specifically, methyl protons in adipose tissue also have long T2 times and slow diffusion. Effective fat suppression is needed for selective PEG imaging. This is easily accomplished as PEG protons resonate 1 ppm upfield from water, making it possible to eliminate adipose tissue signals with appropriate RF fat suppression. Other fat protons, such as repeating methylene groups, have sufficiently long T2 times that they do not appear in the image. **(Figure 3-4)**

3.4.3 Orthotopic tumor PEG imaging

Following tail vein injection, we find optimal uptake of PEG in the tumor cells at about 1 hour post-injection. PDAC cells impede water diffusion, and imaging of with high b-value and short TE (50ms) reveals restricted water. At TE > 250 ms, we observe no residual water signal. **(Figure 3-5)**. Selective imaging of PEG in a tumor requires the PEG component to be selectively delivered to the site of interest. This is achieved by co-administering the PEG with the proprietary tumor activating peptide (iRGD). Administration of either component individually is insufficient to provide effective MR imaging of the PDAC tumor. (**Figure 3-6A, B**) In contrast, PEG-iRGD combination administration provides sufficient PEG uptake by PDAC cells to visualize the tumor. **(Figure 3-6C)**

3.5 Discussion

These results demonstrate a promising strategy to utilize a PEG-iRGD compound to enhance targeted tumor imaging with MRI. Ostensibly, PEG on its own

should be nearly invisible to conventional MRI. The polymer is water-soluble, inert, and maintains no magnetic properties that would generate T1 or T2 relaxation effects. (20) Based on this assumption, other researchers have sought to utilize PEG's unique characteristics as a surface coating for contrast agent nanoparticles. (14-16) The polymer's hydrophilicity and stealth properties reduce rapid clearance by the reticuloendothelial system and prevent protein absorption, thereby extending blood circulation time and improving bioavailability. (21) However, in this study, we demonstrated that PEG on its own, without the aid of additional contrast agents, is visible on MRI imaging with the use of a proper protocol. This was clearly visualized in the *in vitro* arm of our experiment, as well as in both the subcutaneous and orthotopic compartments of our *in vivo* arm, supporting the feasibility of this approach in practical scenarios.

The accumulation of PEG within the pancreatic tumor compartment was due to the addition of iRGD to our pre-scan administration routine. iRGD achieves tumor specificity through a multistep mechanism that depends on both tumor-restricted integrins and neuropilin-1/2, plus tumor-associated protease activity, so penetration is largely confined to malignant tissues and their vasculature. (22) iRGD first binds αvβ3/αvβ5 integrins that are upregulated on many tumor cells and angiogenic tumor endothelium but low in most quiescent normal vessels, providing an initial tumor-vascular homing step. Proteolytic cleavage in the tumor microenvironment then exposes a CendR motif that binds neuropilin-1/2, which are also overexpressed in numerous cancers and correlate with tumor progression, further biasing uptake to malignant tissue. (23-24) Importantly, tumor penetration requires all three cooperating

conditions (αv integrin expression, appropriate proteases, and NRP-1/2 expression) so full activation of the transport pathway rarely occurs in normal tissues where one or more of these are missing or low. The modular design of iRGD—with a vascular homing motif, a protease site, and CendR motif—enhances specificity compared with simple RGD ligands that bind only integrins and mainly accumulate around tumor vessels. (25-26)

The technical aspects of the MRI protocol are as important as the PEG-iRGD compound itself. Water suppression is critical in MRI for several fundamental reasons related to signal dynamics, tissue contrast, and diagnostic visualization. Water suppression techniques like fat saturation enhance the ability to visualize specific tissue pathology. By selectively dampening either water or fat signals depending on the clinical goal, the dynamic range of the receiver can be fully utilized. This allows increased receiver gain while keeping the strong water signal from saturating the system, thereby maximizing the visibility of weaker tissue signals. In pancreatic imaging, suppressing the water signal emphasizes contrast in soft tissue masses and improves visualization of focal lesions within organs. (27-28)

Effective water suppression is also essential for reducing imaging artifacts. Chemical shift artifacts arise from the resonance frequency difference between water and fat (approximately 3.5 ppm), and uncontrolled water signal can create spatial misregistration artifacts, particularly while using the higher 7T MRI unit. (29) Water suppression techniques exploit this chemical shift difference to selectively target and eliminate the water signal, resulting in cleaner images with fewer ghost artifacts. This is particularly important in pancreatic imaging, where the organ's anatomic location in the

abdomen makes it susceptible to motion artifacts that can compound water-related signal problems. (30) Fortunately, once a protocol has been developed, it can be adopted and utilized broadly by technicians at many health centers and research institutions.

Additional work is still needed to validate these results in a larger animal cohort, however these early results are very promising and represent a shift in the way that PEG may be used in the context of MRI. Currently, PEG is used in conjunction with a contrast imaging agent, such as Gd, to take advantage of PEG's biocompatibility and to target desirable features lacking in Gd independently. This PEGylated Gd exhibits increased hydrophilicity, reduced nonspecific protein binding, and prolonged residence in circulation. (31) The branch structure of PEG on PEG-Gd constructs affects molecular tumbling and thus relaxivity, with branched, multi-arm PEG-Gd agents showing higher relaxivity and greater contrast luminance than linear PEG-Gd and some commercial agents. These effects are attributed to reduced terminal mobility and slower rotational dynamics, which increase the efficiency of water-proton relaxation around the Gd centers. (31-33) As previously mentioned, however, Gd carries with it a dubious safety safety profile, with concerns about long-term tissue retention, including in the kidneys and brain. (8-11) Eliminating Gd from the contrast administration cocktail provides a safer alternative for patients who already carry with them a compromised health status. PEG, by comparison, has a well-established safety profile with limited risks.

Based upon this early research, we believe that this PEG-iRGD nanopolymer warrants further exploration as a method to enhance MR imaging of PDAC. This

strategy offers a safe and simple approach to improve diagnosis and surveillance of this terrible disease and hopefully lead to improved patient care and survival.

3.6 References

1. American Cancer Society. Cancer Facts & Figures 2025. Atlanta: American Cancer Society; 2025.

2. National Cancer Institute. (2025). Surveillance, epidemiology, and end results (SEER) program. *Cancer Statistics, SEER Data & Software, Registry Operations*.

3. American Cancer Society. Signs and Symptoms of Pancreatic Cancer [Internet]. www.cancer.org. 2024. Available from: https://www.cancer.org/cancer/types/pancreatic-cancer/detection-diagnosis-staging/signs-and-symptoms.html

4. Canto, M. I., Harinck, F., Hruban, R. H., Offerhaus, G. J., Poley, J. W., Kamel, I., ... & Bruno, M. (2013). International Cancer of the Pancreas Screening (CAPS) Consortium summit on the management of patients with increased risk for familial pancreatic cancer. *Gut*, *62*(3), 339-347.

5. Goggins, M., Overbeek, K. A., Brand, R., Syngal, S., Del Chiaro, M., Bartsch, D. K., ... & Bruno, M. (2020). Management of patients with increased risk for familial pancreatic cancer: updated recommendations from the International Cancer of the Pancreas Screening (CAPS) Consortium. *Gut*, *69*(1), 7-17.

6. Sarfaty, E., Khajoueinejad, N., Zewde, M. G., Yu, A. T., & Cohen, N. A. (2023). Surgical management of pancreatic ductal adenocarcinoma: a narrative review. *Translational Gastroenterology and Hepatology*, *8*, 39.

7. van Beek, E. J., Kuhl, C., Anzai, Y., Desmond, P., Ehman, R. L., Gong, Q., ... & Wang, M. (2019). Value of MRI in medicine: More than just another test?. *Journal of Magnetic Resonance Imaging*, *49*(7), e14-e25.

8. Iyad, N., Ahmad, M. S., Alkhatib, S. G., & Hjouj, M. (2023). Gadolinium contrast agents-challenges and opportunities of a multidisciplinary approach: Literature review. *European journal of radiology open*, *11*, 100503.

9. Starekova, J., Pirasteh, A., & Reeder, S. B. (2024). Update on gadolinium-based contrast agent safety, from the AJR special series on contrast media. *American Journal of Roentgenology*, *223*(3), e2330036.

10. Mendichovszky, I. A., Marks, S. D., Simcock, C. M., & Olsen, Ø. E. (2008). Gadolinium and nephrogenic systemic fibrosis: time to tighten practice. *Pediatric radiology*, *38*(5), 489-496.

11. Cunningham, A., Kirk, M., Hong, E., Yang, J., Howard, T., Brearley, A., ... & Wagner, B. (2024). The safety of magnetic resonance imaging contrast agents. *Frontiers in Toxicology*, *6*, 1376587.

12. D'souza, A. A., & Shegokar, R. (2016). Polyethylene glycol (PEG): a versatile polymer for pharmaceutical applications. *Expert opinion on drug delivery*, *13*(9), 1257-1275.

13. Yang, L., Fu, S., Cai, Z., Liu, L., Xia, C., Gong, Q., ... & Ai, H. (2021). Integration of PEG-conjugated gadolinium complex and superparamagnetic iron oxide nanoparticles as T 1–T 2 dual-mode magnetic resonance imaging probes. *Regenerative Biomaterials*, *8*(6), rbab064.

14. Cruje, C., Dunmore-Buyze, P. J., Grolman, E., Holdsworth, D. W., Gillies, E. R., & Drangova, M. (2021). PEG-modified gadolinium nanoparticles as contrast agents for in vivo micro-CT. *Scientific reports*, *11*(1), 16603.

15. Alvares, R. D., Lau, J. Y., Macdonald, P. M., Cunningham, C. H., & Prosser, R. S. (2017). Direct quantitative 13C-filtered 1H magnetic resonance imaging of PEGylated biomacromolecules in vivo. *Magnetic Resonance in Medicine*, *77*(4), 1553-1561.

16. Sadzuka, Y., Kishi, K., Hirota, S., & Sonobe, T. (2003). Effect of polyethyleneglycol (PEG) chain on cell uptake of PEG-modified liposomes. *Journal of liposome research*, *13*(2), 157-172.

17. Zuo, H. (2019). iRGD: a promising peptide for cancer imaging and a potential therapeutic agent for various cancers. *Journal of Oncology*, *2019*(1), 9367845.

18. Yin, H., Yang, J., Zhang, Q., Wang, H., Xu, J., & Zheng, J. (2017). iRGD as a tumor-penetrating peptide for cancer therapy. *Molecular medicine reports*, *15*(5), 2925-2930.

19. Desgrosellier, J. S., & Cheresh, D. A. (2010). Integrins in cancer: biological implications and therapeutic opportunities. *Nature Reviews Cancer*, *10*(1), 9-22.

20. Hutton, W. C., Bretthorst, G. L., Garbow, J. R., & Ackerman, J. J. (2009). High dynamic-range magnetic resonance spectroscopy (MRS) time-domain signal analysis. *Magnetic Resonance in Medicine: An Official Journal of the International Society for Magnetic Resonance in Medicine*, *62*(4), 1026-1035.

21. Kobayashi, H., Kawamoto, S., Saga, T., Sato, N., Hiraga, A., Ishimori, T., ... & Brechbiel, M. W. (2001). Positive effects of polyethylene glycol conjugation to generation-4 polyamidoamine dendrimers as macromolecular MR contrast agents. *Magnetic Resonance in Medicine: An Official Journal of the International Society for Magnetic Resonance in Medicine*, *46*(4), 781-788.

22. Kang, S., Lee, S., & Park, S. (2020). iRGD peptide as a tumor-penetrating enhancer for tumor-targeted drug delivery. *Polymers*, *12*(9), 1906.

23. Nikitovic, D., Kukovyakina, E., Berdiaki, A., Tzanakakis, A., Luss, A., Vlaskina, E., ... & Kuskov, A. (2024). Enhancing tumor targeted therapy: the role of iRGD peptide in advanced drug delivery systems. *Cancers*, *16*(22), 3768.

24. Meng, F., Liu, J., Wei, J., Yang, J., Zhou, C., Yan, J., & Liu, B. (2022). Tumor-penetrating peptide internalizing RGD enhances radiotherapy efficacy through reducing tumor hypoxia. *Cancer Science*, *113*(4), 1417-1427.

25. Zuo, H. (2019). iRGD: a promising peptide for cancer imaging and a potential therapeutic agent for various cancers. *Journal of Oncology*, *2019*(1), 9367845.

26. Qian, J., Zhou, S., Lin, P., Lei, J., Zheng, S., Xu, W., ... & Yang, J. (2023). Recent advances in the tumor-penetrating peptide internalizing RGD for cancer treatment and diagnosis. *Drug Development Research*, *84*(4), 654-670.

27. Del Grande, F., Santini, F., Herzka, D. A., Aro, M. R., Dean, C. W., Gold, G. E., & Carrino, J. A. (2014). Fat-suppression techniques for 3-T MR imaging of the musculoskeletal system. *Radiographics*, *34*(1), 217-233.

28. Hauger, O., Dumont, E., Chateil, J. F., Moinard, M., & Diard, F. (2002). Water excitation as an alternative to fat saturation in MR imaging: preliminary results in musculoskeletal imaging. *Radiology*, *224*(3), 657-663.

29. Huang, S. Y., Seethamraju, R. T., Patel, P., Hahn, P. F., Kirsch, J. E., & Guimaraes, A. R. (2015). Body MR imaging: artifacts, k-space, and solutions. *Radiographics*, *35*(5), 1439-1460.

30. Harrington, K. A., Shukla-Dave, A., Paudyal, R., & Do, R. K. (2021). MRI of the Pancreas. *Journal of Magnetic Resonance Imaging*, *53*(2), 347-359.

31. Yallapu, M. M., Foy, S. P., Jain, T. K., & Labhasetwar, V. (2010). PEG-functionalized magnetic nanoparticles for drug delivery and magnetic resonance imaging applications. *Pharmaceutical research*, *27*(11), 2283-2295.

32. Doble, D. M., Botta, M., Wang, J., Aime, S., Barge, A., & Raymond, K. N. (2001). Optimization of the relaxivity of MRI contrast agents: effect of poly (ethylene glycol) chains on the water-exchange rates of GdIII complexes. *Journal of the American Chemical Society*, *123*(43), 10758-10759.

33. Hsu, Y. I., Mahara, A., & Yamaoka, T. (2018). Influence of molecular mobility on contrast efficiency of branched polyethylene glycol contrast agent. *Contrast Media & Molecular Imaging*, *2018*(1), 1259325.

3.7 Figures

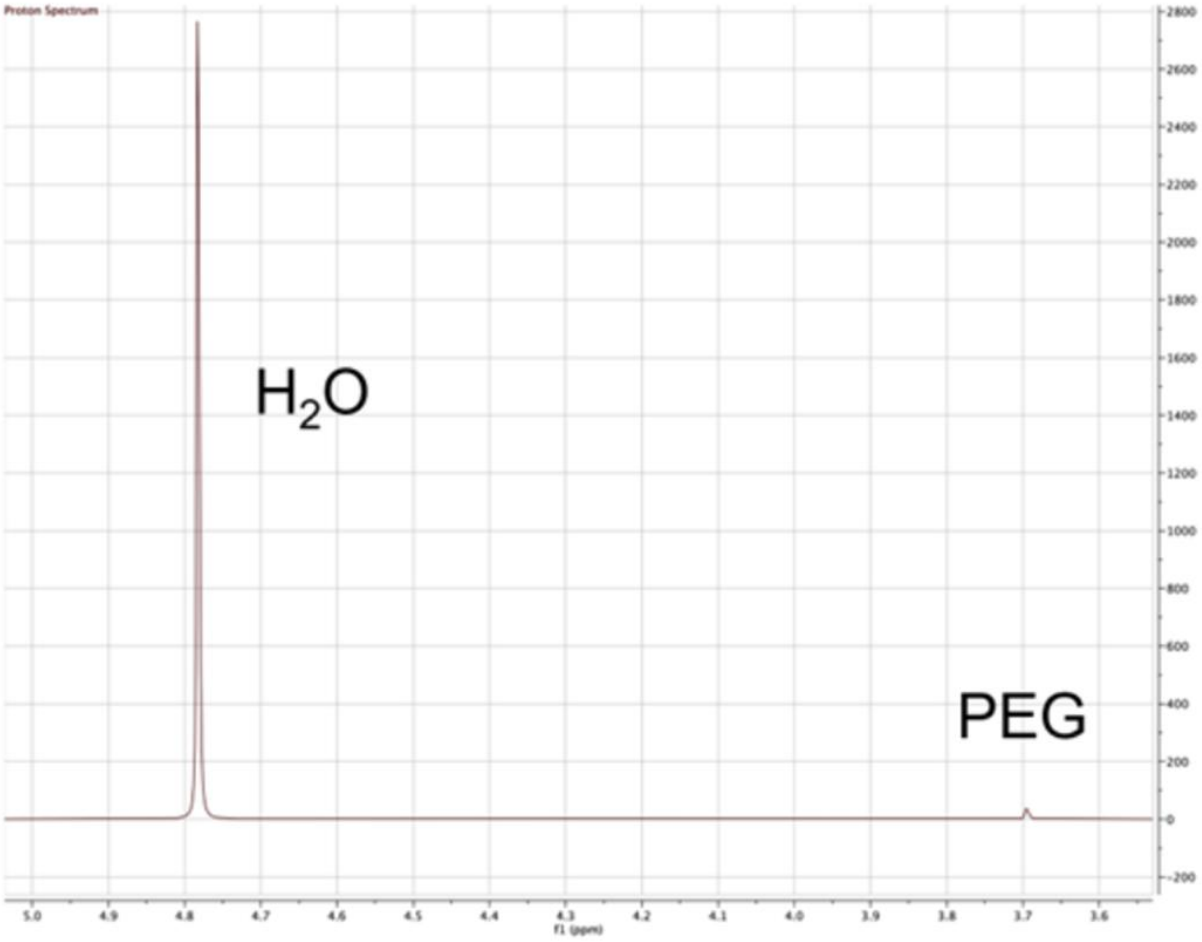


Figure 3-1 Nuclear magnetic resonance (NMR) spectrum depicting separation between water and polyethylene glycol (PEG) signatures.

The unique, non-overlapping NMR peaks of water (~4.8ppm) and PEG (~3.7ppm) enhance the potential for PEG to be a high quality magnetic resonance imaging candidate. [8PEG] = 125 uM; [^{1}H] = 454 mM.

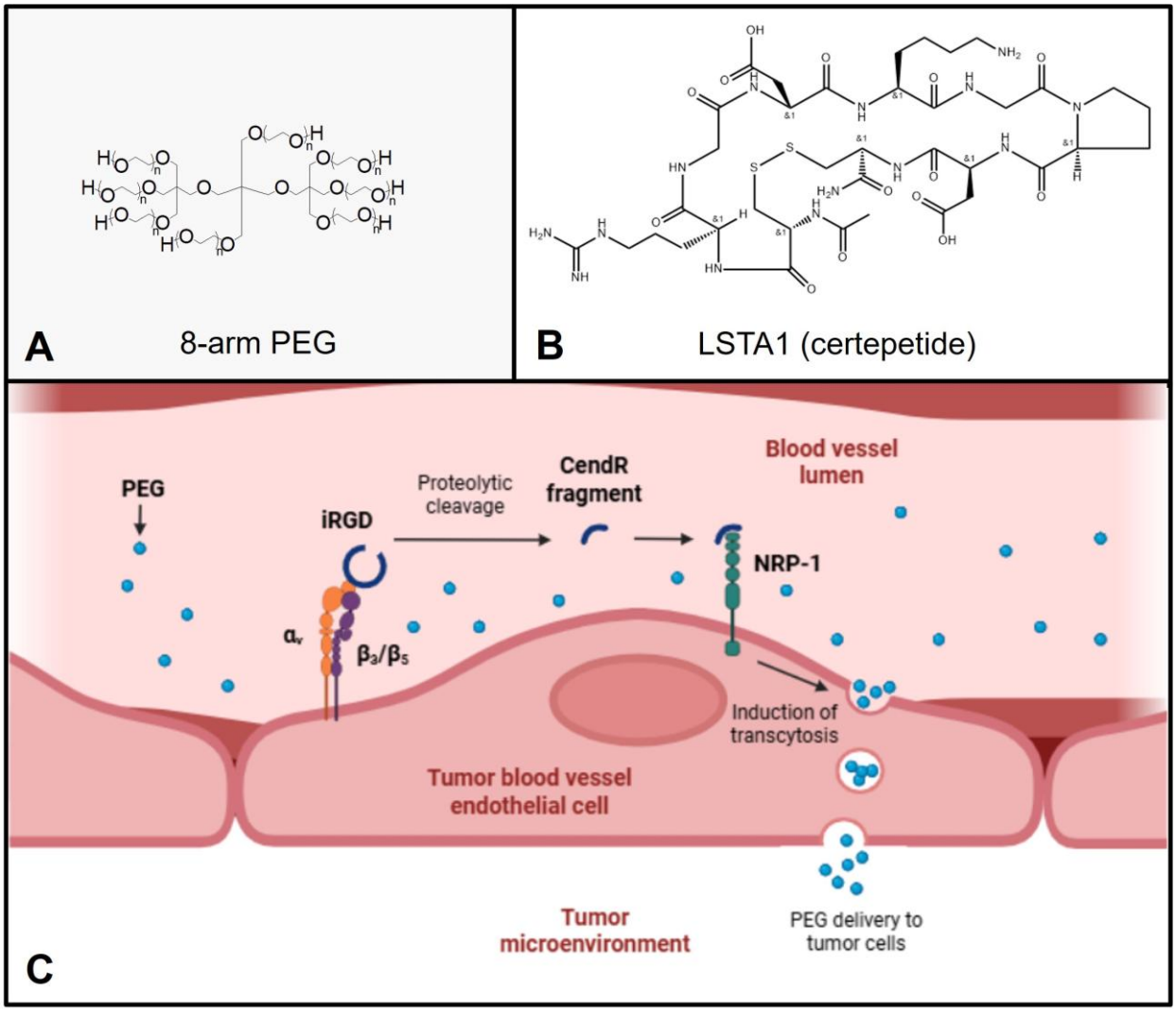


Figure 3-2 Schematic of the iRGD-PEG imaging strategy.

A) Eight-arm PEG (molecular weight = 20k) is used as a molecular imaging agent with desirable NMR/MRI properties. B) Structure of LSTA1 (certepetide), which is the specific iRGD peptide used in this project. C) iRGD is co-administered with PEG via tail vein injection, causing the CendR fragment of the iRGD to bind to neuropilin-1 (NRP-1) receptors in pancreatic cancer cells, allowing PEG into the tumor cells via transcytosis.

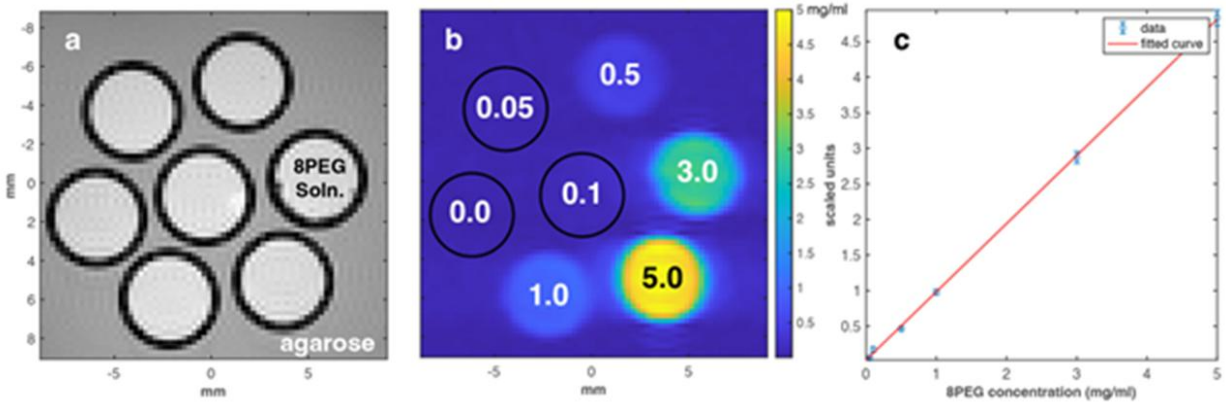


Figure 3-3 Sensitivity of magnetic resonance imaging (MRI) to diffusion-weighted (DW), T2-weighted (T2W) selective polyethylene glycol (PEG) imaging.

A) A phantom consisting of 5mm nuclear magnetic resonance tubes filled with PEG solutions between 0 and 5mg/ml, embedded in agarose. B) Selective PEG imaging DW, T2W single shot fast-spin echo (FSE). C) Linear dependence of MR PEG signal with concentration. Diffusion weighting with b=5000 s/mm^2 and time to echo (TE) = 256 ms eliminates all water signal and provides a linear concentration dependence for the PEG signal.

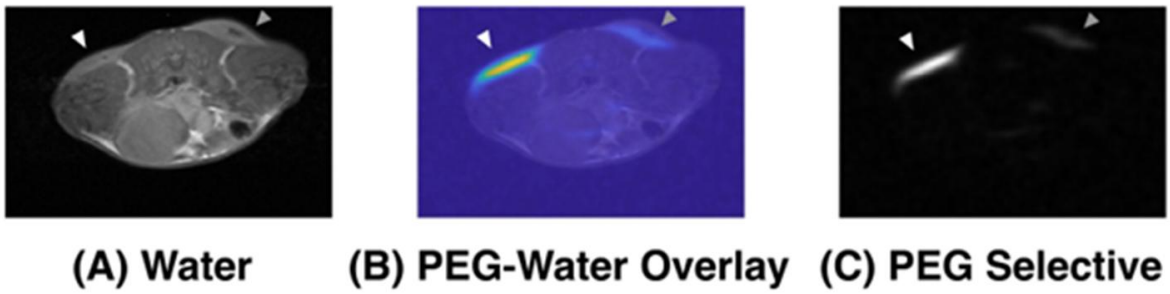


Figure 3-4 *In vivo* imaging of PEG in mouse with PEG-Matrigel flank injection.

Co-administration of Matrigel with PEG at 10mg/ml (white arrows) and 2mg/ml (gray arrows). Images depict A) standard proton fast-spin echo image, B) overlay of water and PEG image, and C) selective imaging of PEG using b=5200 s/mm^2 and TE=256 ms. These images demonstrate that diffusion-weighted, T2-weighted, fast-spin echo MRI is able to selectively image PEG *in vivo*.

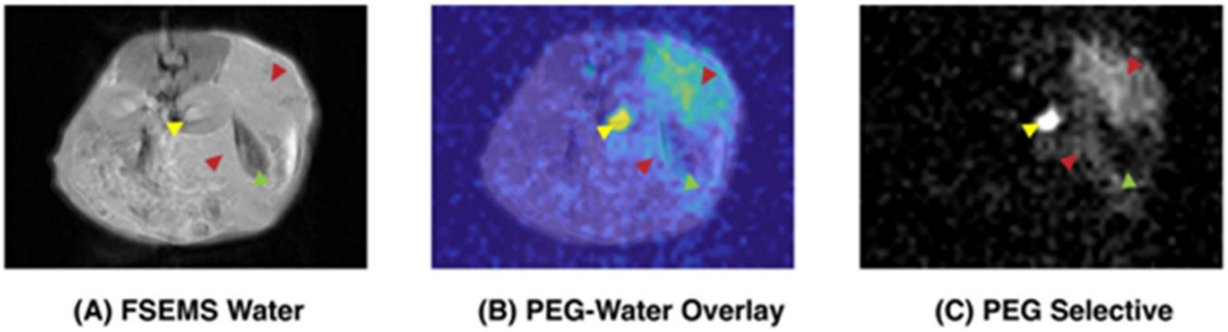


Figure 3-5 Selective imaging of PEG in murine PDAC tumors.

Mice were orthotopically implanted with pancreatic cancer cells and allowed to grow for two weeks. Arrows identify the kidney (yellow), spleen (green), and pancreatic tumor (red arrows). A) Fast-spin echo water image. B) Overlay of colorized PEG image onto the water image. C) Selective PEG image. Note the localization of white/grey in the selective image (C) represents PEG accumulation in the tumor site with excess being excreted. PEG imaging time was 15 minutes.

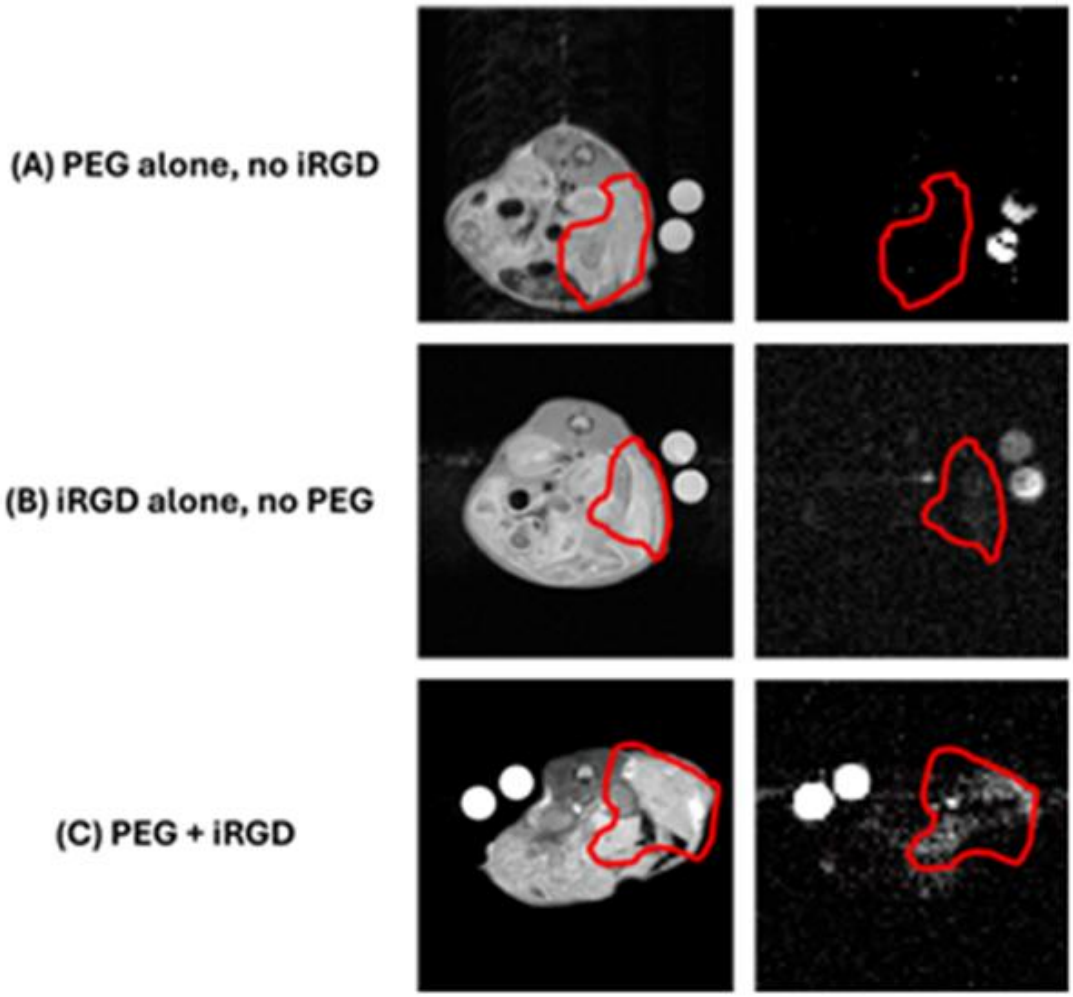


Figure 3-6 *In vivo* imaging of singular PEG, singular iRGD, and joint PEG-iRGD administration.

MRI images of mice with pancreatic tumors (outlined in red) next to two external PEG phantoms for reference. A) Image of PEG-only administration, which lacks uptake and retention by the tumor cells. B) Image of iRGD-only administration, which lacks PEG visualization. C) Image of PEG and iRGD co-administration, which demonstrates visual uptake and retention of PEG by the tumor cells. Taken together, these images demonstrate the insufficiency of PEG or iRGD alone in visualizing the pancreatic tumor.

Chapter 4: Future Directions and Conclusions

4.1 Background

The work described in Chapters 2 and 3 represent two distinct, yet complementary approaches to addressing the high mortality associated with PDAC. The analysis of GOT1/GOT2 as a druggable target to counteract the metabolic rewiring that is a hallmark of PDAC represents an attempt to understand the underlying biology of the disease and provide alternative treatment options. In contrast, an enhanced MRI protocol could improve diagnostic strategies and change the way that PDAC is tracked in patients. Both projects have work left to do, and in this chapter, I will detail future experiments for each that will strengthen the knowledge surrounding our understanding of PDAC surveillance and treatment. Finally, I will conclude with the key takeaways that I have gained from this dissertation work and how it applies to the broader field of pancreatic cancer research.

4.2 Future Directions: Assessing the Essentiality of GOTs in the Pancreas

In order to fully understand the role that GOT1 and GOT2 play in the pancreas, both in the context of PDAC and in normal development, a few key studies remain. As alluded to in the conclusion of Chapter 2, the compensatory circuits that allow GOT1/2 to be dispensable remain undefined. Stable isotope tracing could be used to identify alternative aspartate sources and anaplerotic routes in GOT1/2-deficient mice. Glucose,

glutamine, and serine could all undergo labeling and could elucidate which pathways are responsible. Alternate aminotransferases may also be playing a role in aiding the PDAC cells in nutrient scavenging. Expression of glutamate-pyruvate transaminase (GPT), phophoserine aminotransferase 1 (PSAT1), and branched-chain amino acid 1/2 (BCAT1/2) could all be measured to in our GOT1/2 depleted model to see what role they may be playing. (1-3) Upon successful discovery of these compensatory pathways, inhibition strategies could be developed to determine if a combinatorial approach is more successful to stifle PDAC progression than by simply inhibiting GOT function.

In contrast to the extensive research that has been done exploring GOT inhibition in PDAC, the role of both GOTs in normal pancreas development is in its relative infancy. The early experiments thus far have shown that a dual knockout results in a markedly reduced pancreas size with no overt signs of functional impairment. This could once again point to a robust compensatory framework, however, this model requires additional rigorous testing in order to come to that conclusion. The first step will be to take these animals out longer than 8 weeks to see what effect the diminished pancreas size has on healthspan and lifespan. These animals may be more susceptible to specific stressors and have a higher likelihood of developing pancreatitis or fibrosis after injury. It will be helpful to identify if they experience subtle or overt deficiencies as they age. Furthermore, while circulating amylase and insulin levels were evaluated, other pancreatic products like lipase and proteases were not measured. Instead, stool samples were deemed to be normal in appearance, which may not be a definitive proxy for digestive function.

4.3 Future Directions: MR Imaging with PEG-iRGD

There is a great deal of work remaining before our MRI protocol utilizing this novel PEG-iRGD compound can have significant clinical impact. The experiments detailed within this thesis represent early, yet promising results that require additional validation and rigorous assessment. Following the initial successes described in our pilot study, the immediate first step will be to expand the number of animals in each group in order to demonstrate statistically significant differences among our groups. This will provide support that the initial results that we have seen are valid and that PEG-iRGD combination enables high quality MRI surveillance of PDAC. Additional rodent studies can be performed to optimize the protocol, including dose-response and administration timing experiments to determine how much of each component is required to achieve the best uptake by the tumor and how far in advance of imaging the PEG-iRGD should be administered to the subject.

Once the protocol optimization has been completed, it will be important to provide a direct comparison between the new MRI protocol the other imaging modalities, namely PET and CT, in order to evaluate the resolution differences that may exist among these options. Additionally, a head-to-head evaluation of the PEG-iRGD imaging protocol to gadolinium-based contrast agent (GBCA) administration is essential to determine if target tissue sharpness and clarity are differential between the two options. If this study demonstrates that our MRI protocol outperforms or is comparable to the other two systems in regard to image quality and resolution, then it would provide an impetus to move the technology to the next step of preclinical evaluation. Clear

statistical superiority is not necessarily required for PEG-iRGD to warrant further utilization, as the safety profile of PEG and MRI is favorable when compared to GBCA and PET/CT, respectively.

Ultimately, since this imaging protocol is inherently patient-centered in nature, these studies need to be designed with an eye toward clinical implementation. As such, the long-term road to adoption has to be considered and what barriers currently exist. PEG itself has long been approved by the US Food and Drug Administration (FDA) for a number of clinical indications, both in its individual form and as a component in PEGylated products. The former is used for as a laxative for constipation, while the latter has a wide range of approved therapeutic uses, including chronic hepatitis, anemia, hemophilia, and enzyme deficiences. (4) Given its current status as an approved compound, the safety profile of PEG is well-established and therefore the regulatory hurdles to adoption as an MRI contrast agent could be substantially decreased. Its use in combination with iRGD has not been evaluated, however, representing a future issue that would need to be addressed.

Multiple preclinical studies have demonstrated iRGD's efficacy when conjugated to or co-administered with various therapeutic modalities: chemotherapy (doxorubicin, paclitaxel, gemcitabine, camptothecin), immunotherapy (anti-PD-1 antibodies), siRNA delivery, and NK cell engineering. (5-10) In murine cancer models spanning breast cancer, glioblastoma, pancreatic cancer, gastric cancer, and melanoma, iRGD-modified delivery systems consistently enhanced tumor accumulation, deep tissue penetration, and therapeutic efficacy compared with untargeted or unmodified agents. In pancreatic

cancer models specifically, iRGD-modified NK cells significantly reduced tumor growth and improved survival in subcutaneous and orthotopic xenografts. (10) Although iRGD has been extensively validated in preclinical models, it has not yet been approved by the FDA and is not used in routine clinical practice. Rather, iRGD remains in the preclinical and early translational research stage, with no completed human clinical trials directly testing iRGD as a therapeutic agent. (11)

Given the currently unapproved status of this PEG-iRGD combination drug administration, there is a long road ahead for this strategy prior to its use in humans for improving MRI. Although PEG is already FDA-approved and used widely, it would need to be reevaluated for safety and efficacy when administered with iRGD. This will require preclinical toxicology, pharmacokinetic, and pharmacodynamic assessments prior to an Investigational New Drug (IND) application with the FDA and subsequent clinical trials.

Although the focus of this study has been using PEG-iRGD to improve MRI for PDAC, this protocol could have utility for a variety of cancers throughout the body, specifically for solid tumors. iRGD is most compatible on solid tumors that express αvβ3/αvβ5 integrins (especially on tumor neovasculature and/or cancer cells) and neuropilin-1 (NRP-1), plus tumor-associated proteases to activate the CendR motif. Integrins located on tumor neovasculature and/or cancer cells themselves make for the best targets with associated NRP-1 on endothelium and tumor cells. (12) In addition to PDAC, there are several other candidate cancers that have strong preclinical validation using iRGD for tumor penetration. These include breast cancer, prostate cancer, glioblastoma, lung cancer, and gastric cancer. NRP-1 and αvβ3 are overexpressed in

breast cancer, especially in triple-negative and metastatic subtypes, and correlate with advanced disease and poor prognosis. (13) As such, our MRI protocol may be most effective to monitor disease progression and metastasis in these cases.

4.3 Conclusions

Receiving a PDAC diagnosis is a devastating scenario for patients and their families. This terrible disease carries with it a very poor prognosis and few successful treatment options for the vast majority. As such, it should be a priority for the biomedical community to focus financial and academic resources into improving the surveillance, diagnostic and evaluative imaging, and therapeutic options PDAC. Ultimately, each of these aspects of the care spectrum have room for improvement and refinement.

Our work delivers a compelling demonstration that aspartate transaminases GOT1 and GOT2 are dispensable for both pancreatic cancer progression and have more modest effects on normal pancreatic development than initially expected. Even complete loss of both enzymes fails to prevent or delay tumor formation or growth in multiple physiologically relevant cancer models. These findings fundamentally challenge the therapeutic potential of GOT inhibitors as monotherapy and underscore the critical importance of model selection when validating metabolic targets. The metabolic adaptability of PDAC, including its ability to recruit alternative pathways, harness microenvironment support, and maintain function despite loss of putatively essential enzymes, represents both a formidable therapeutic challenge and a revealing window into cancer biology. Future therapeutic strategies must account for this plasticity,

targeting not only cancer cell metabolism but also the supportive metabolic ecosystem that enables tumor survival when individual pathways are disrupted.

In addition to exploring new therapeutic opportunities, better imaging modalities are critical to making early diagnosis of PDAC a reality. Currently, routine surveillance is not recommended for the general population or those with average risk. This is due in large part to the low prevalence of the disease and the perceived risks of false positives, overtreatment, invasive diagnostic procedures, and the psychological burden on those being screened. Clearly, to combat these challenges, an accurate, non-invasive, widely available, and inexpensive diagnostic procedure would be welcomed. Although admittedly early in its development, the PEG-iRGD MRI protocol presents a new approach to overcoming some of these barriers and it may encourage other novel imaging techniques to be designed with some or all of the components utilized.

In summary, the metabolic heterogeneity of PDAC demands precise, context-specific therapeutic strategies. Single-pathway inhibition routinely fails due to compensatory metabolic flexibility; therefore, effective interventions require multi-pronged combinatorial approaches targeting metabolic vulnerabilities, signaling adaptations, and the immunosuppressive microenvironment simultaneously. Translating these mechanistic insights into clinical trials will be essential to improve outcomes for PDAC patients. Pairing therapeutic advancements with earlier and more effective diagnostic imaging and improved surveillance would offer a massive step forward for these patients and offer them the chance to beat this devastating disease.

4.4 References

1. Nong, X., Zhang, C., Wang, J., Ding, P., Ji, G., & Wu, T. (2022). The mechanism of branched-chain amino acid transferases in different diseases: Research progress and future prospects. *Frontiers in Oncology*, *12*, 988290.

2. Baytas, O., Davidson, S. M., DeBerardinis, R. J., & Morrow, E. M. (2022). Mitochondrial enzyme GPT2 regulates metabolic mechanisms required for neuron growth and motor function in vivo. *Human molecular genetics*, *31*(4), 587-603.

3. Ciuffoli, V., Feng, X., Jiang, K., Acevedo-Luna, N., Ko, K. D., Wang, A. H. J., ... & Sartorelli, V. (2024). Psat1-generated α-ketoglutarate and glutamine promote muscle stem cell activation and regeneration. *Genes & Development*, *38*(3-4), 151-167.

4. Gao, Y., Joshi, M., Zhao, Z., & Mitragotri, S. (2024). PEGylated therapeutics in the clinic. *Bioengineering & translational medicine*, *9*(1), e10600.

5. Zou, L., Chen, J., Bai, X., Wang, Y., Lu, C., Wang, Q., ... & Du, J. (2025). Tumor-penetrating peptide boosts bispecific T-cell engager antitumor efficacy for the pancreatic cancer. *Frontiers in Immunology*, *16*, 1693755.

6. Kang, S., Lee, S., & Park, S. (2020). iRGD peptide as a tumor-penetrating enhancer for tumor-targeted drug delivery. *Polymers*, *12*(9), 1906.

7. Singh, T., Kim, T. W., Murthy, A. S., Paul, M., Sepay, N., Kong, H. J., ... & Im, J. (2024). Tumor–homing peptide iRGD-conjugate enhances tumor accumulation of camptothecin for colon cancer therapy. *European Journal of Medicinal Chemistry*, *265*, 116050.

8. Nikitovic, D., Kukovyakina, E., Berdiaki, A., Tzanakakis, A., Luss, A., Vlaskina, E., ... & Kuskov, A. (2024). Enhancing tumor targeted therapy: the role of iRGD peptide in advanced drug delivery systems. *Cancers*, *16*(22), 3768.

9. Zuo, H. (2019). iRGD: a promising peptide for cancer imaging and a potential therapeutic agent for various cancers. *Journal of Oncology*, *2019*(1), 9367845.

10. Song, G., Qi, X., & Zhao, Y. (2025). iRGD Tumor Penetrating Peptide-Modified NK Cells Exhibit Enhanced Tumor Immune Infiltration Ability and Anti-Tumor Efficacy. *Protein & Peptide Letters*, *32*(3), 183-193.

11. Rocchi, A., Teesalu, T., & Celia, C. (2025). Advancing Cancer-Targeted Nanotherapies with Tumor Homing Peptides. *ACS Pharmacology & Translational Science*, *8*(7), 1919-1933.

12. Liu, X., Jiang, J., Ji, Y., Lu, J., Chan, R., & Meng, H. (2017). Targeted drug delivery using iRGD peptide for solid cancer treatment. *Molecular systems design & engineering*, *2*(4), 370-379.

13. Yao, L., Li, Y., Chen, H., Wen, X., Pang, Y., Chen, Z., ... & Guo, W. (2022). Dual targeting of integrin αvβ3 and neuropilin-1 receptors improves micropositron emission tomography imaging of breast cancer. *Molecular Pharmaceutics*, *19*(5), 1458-1467.